November 2021

Modeling, Identification, and Stability Analysis of Inverter-Based Resources Integrated Systems

Miao Zhang
University of South Florida

Modeling, Identification, and Stability Analysis of Inverter-Based Resources Integrated Systems

by

Miao Zhang

A dissertation submitted in partial fulfillment
of the requirements for the degree of
Doctor of Philosophy
Department of Electrical Engineering
College of Engineering
University of South Florida

Major Professor: Zhixin Miao, Ph.D.
Lingling Fan, Ph.D.
Chung Seop Jeong, Ph.D.
Achilleas Kourtellis, Ph.D.
Kaiqi Xiong, Ph.D.

Date of Approval:
November 2, 2021

Keywords: Dynamic modeling, Frequency domain analysis, System identification, Inverters, Weak grids

Dedication

My dissertation work is dedicated to my father, Yungang Zhang, and my mother, Junxia Liu. Without their endless love and encouragement I would never have been able to complete my Ph.D. studies. I love you both and I appreciate everything that you have done for me.

Acknowledgments

Without the full support from many professors and colleagues, my research studies would never occurred. I wish to express my sincere gratitude to the following people:

Dr. Zhixin Miao, my major professor, who gave me continuous support, guidance, suggestions, and encouragement all the way in my graduate studies. He is always patient on any questions I have asked.

Dr. Lingling Fan who always gave excellent guidance and support on my research in the past few years. She generously taught me the technique skills and knowledge on power systems. Furthermore, I learned the attitude and methodology on how to tackle engineering issues from her.

Dr. Achilleas Kourtellis, my supervisor during I was working as a graduate assistant in Center for Urban Transportation Research (CUTR). He offered a great opportunity for me to access the transportation area where I can utilize my electric skills to improve the safety of public transportation.

Dr. Chung Seop Jeong and Dr. Kaiqi Xiong, two significant committee members of my dissertation. I truly appreciate your comments and advises on my research works. That helps me a lot in polishing my presentation and thesis writing.

Finally, I would like to give my thanks to all my colleagues who were there when I need help: Dr. Yin Li, Dr. Yangkun Xu, Dr. Minyue Ma, Dr. Anas Almunif, Dr. Ibrahim Alsaleh, Dr. Abdullah Alassaf, Yi Zhou, Li Bao, Zhengyu Wang, Rabi Kar, Ratik Mittal, Huazhao Ding, etc.

Table of Contents

List of Tables

List of Figures

Abstract

More and more stability issues have been observed in real-world inverter-based resources (IBRs) power systems. Stability analysis is highly requested in the industrial area. To have an insight into the root causes of stability issues within IBR integrated systems, e.g, PV, wind, and battery storage systems, the dynamic characteristics should be fully understood.

The approaches are different when considering the presupposition of investigated IBR systems. A reduced-order analytical model of the IBR integrated system can be built if the IBR is treated as a white box. Since the parameters and control structures of converter control can be accessed. This analytical model can be used to reveal stability issues and propose improvement accordingly. However, completely replicating the real-world PV farms is not feasible. Some details should be ignored in a simplified model to conduct mathematical analysis. Meanwhile, the PV model must be accurate enough to capture major dynamic characteristics from the original PV system. Utilizing small-signal analysis of the linearized mathematical model, eigenvalue analysis can reveal the oscillation modes and identify the most impact states via participation factor analysis. Additionally, the stability impact of IBR controller parameters can be examined by open-loop analysis.

On the other hand, the internal details of original equipment manufacturers (OEMs) will not be provided for most scenarios due to confidential reasons. Under this condition, the IBRs are like black boxes. The dynamic characteristics can only be identified via measurement data. Consequentially, a s-domain admittance model can be found to lead the eigenvalue analysis. With measured admittance model, two things can be achieved. The first one is that extended mode shape analysis can be carried out to explain the dynamic phenomenons on various measurements, i.e., voltage magnitudes, current magnitudes, frequencies, real and reactive powers at different buses. In this way, the interactions among IBRs in a power system can be figured out. Another one is carrying

out dynamic simulation using the admittance model only. Numerical Laplace transform (NLT) is adopted to convert the frequency-domain data to fast time-domain simulation.

Chapter 1: Introduction

1.1 Background and Motivation

With increasing inverter-based resources (IBRs) are integrated into power grids, industry are confronting system stability challenges. One of them is instability due to IBRs integrated into systems with low short circuit strength, which is called weak grids [1]. In real world, there are some stability dynamic events observed in renewable energy IBR integrated systems. Low-frequency oscillations at 4 Hz were observed in type-4 wind farms in Texas [2]. A utility-scale PV plant experienced 7 Hz oscillations in power measurement during transmission line outage [3]. In the California Canyon 2 Fire disturbance, PV inverters tripped due to a subcycle (less than quarter cycle) measured voltage above the overvoltage protective setting [4].

Among the IBR integrated systems, type-4 wind farms dynamic phenomenon has been thoroughly analyzed by a simplified type-4 wind model, e.g., in [5–8]. Since grid-following VSC is employed for both type-4 wind farms and solar PVs to connect with power grids, it is reasonable to implement the similar modeling concept to PV farm system modeling. The grid-follow converters under weak grid condition stability mechanism can be summarized as follows. The converter is designed in dq-axis to regulate the inner current control loop. No matter it adopts active power control or dc-voltage control on outer d-axis, increasing the power generation leads to the increase of d-axis current order, where d-axis aligns with the point of common coupling (PCC) voltage. Larger current magnitude results decrease of voltage magnitude, which will limit the active power. Then an instability phenomenon will occur [5]. Therefore, proposing a powerful mathematical analytical model to reveal the stability root cause behind the brief mechanism concept is significant.

Since the increasing penetration of IBRs in modern power grids, the scope of this author would not just be limited to existing stability issues. As a researcher, more potential and scalable IBR

related stability problems should be predicted. Accordingly, solutions should be proposed to tackle those issues. E.g., a 3-Hz oscillation has been found in the IEEE 9-bus 100% IBR-penetrated power grid originally developed by National Renewable Energy Lab (NREL) [9]. This observation indicates the grid-forming converters is not immune to stability issues, although grid-forming converter can enhance synchronize stability in weak grid [10] and has advanced dynamic response over grid-following converters [11–13].

Also, the meshed network cannot be split into a two-component system or a single IBR integrated system. A planner would like to predict system stability for a combination of grid-forming and grid-following IBRs penetrated at different locations. Then the IBRs interactions can be determined. Integrating an admittance of an entire grid has been discussed in [14]. Nevertheless, it is important to conduct more studies to investigate the critical influencing factors for dominant oscillation modes.

In the author's previous works, e.g, [15, 16], IBR modeling are based on speculation of a white-box. However, the IBRs are black-boxes in the perspective of grid operators for the most time. For a specific wind farm or solar system, impedance/admittance model obtained from measurements are generally used [17]. Hence, identifying the dynamic characteristics of IBRs with measurement data only will be another essential mission.

1.2 Statement of Problems

Due to the increasing renewable energy sources in power market and resulted dynamic issues observed in real world, high IBR-penetrated network stability analysis is the focus topic in the following materials. To address this problem, there are two questions should be tackled.

- The first problem is to propose a reduced-order simplified system for industry to reveal the root cause of any stability oscillations in a Solar Photovoltaic (PV) system. Without sacrificing the accuracy, eliminate the less dynamic impact part in this analytical model. Comparing with existing modeling approaches, this model should be a state-of-art methodology to carry out not only linearized eigenvalue analysis but also time-domain simulation. This scenario is

based on assumption that the IBR is based on speculation of control structures and parameters.

- The second problem is to make a inquiry if it is possible to conduct stability analysis with measured admittance-based model. Since IBR's converter control information is technology proprietary, which is not fully accessible to industry operators. It will be efficient that an admittance model of IBR can be found only based on measurement data. Then integrate it to a scalable meshed network so that the whole system admittance model can be built. Eigenvalue analysis and extended mode analysis can reveal dynamic performance caused by the oscillation mode. Furthermore, a fast time-domain simulation results is expected to be produced with measured admittance model instead of complicated electromagnetic transient (EMT) testbed.

1.3 State-of-the-Art Survey

Some literature is visited by the author to have a widely understand of relevant state-of-the-art works. In this section, the investigation are conducted from three aspects. The first part is the introduction on grid-forming converter. Since grid-following converter has been well-known for stability issues under weak grids. Grid-forming converters are becoming popular in modern power grid in the past decade. The basic control structure and stability performance should be studies before investigating its dynamic performance. The second one is IBR system modeling approaches. With acknowledging the limitations of existing converter modeling approaches, an advanced and powerful mathematical analytical model can be proposed. The third part is IBR identification methods. There are some popular tools available for system identification. Depending those methods, the IBR admittance characterization will be revealed. That will help on the admittance-based modeling when treating IBRs as black-boxes.

1.3.1 Grid-Forming (GFM) Converter

The most PV and wind converters operated as grid-following (GFL) converters. They can measure and track grid side voltage angle by phase-lock loop (PLL). In contract, the grid-forming based converter can regulate the voltage magnitude and frequency at the point of common coupling (PCC) point or converter side. A grid-following converter behaviors as a current source in parallel with a impedance, while a grid-forming converter acts as a voltage source behind a series impedance [13, 18]. Therefore, the grid-forming converter can enhance synchronize stability in weak grid [10]. They are adopted in battery energy storage converters in a island or microgrid system. For the high-penetrated inverter-based resources (IBRs) system, the grid-forming converter has advanced dynamic response over grid-following converters [11–13]. However, the interactions between GFM converters have not been fully discussed. Chapter 4 will fill this gap.

1.3.1.1 Two GFM Voltage Controls

There are two commonly used voltage control strategy for grid-forming converters: multi-loop (or double-loop) voltage control and single-loop voltage control [19], which gives two basic grid-forming control structures with droop loops determined frequency $\omega*$ and voltage amplitude $v*$.

The major difference between those two voltage control strategies is that they regulate the voltage magnitude and frequency at different point. The single-loop controls the voltage and frequency at the converter internal voltage point, while multi-loop controls the voltage and angular frequency at the PCC bus. Thus, single-loop control advances multi-loop control on stability performance due to simpler structure and less coupling reactance of grid-forming converter [19]. On the other hand, the single-loop control lacks of current control capability, which can cause the converter tripping due to a fault [13].

Grid-forming control generally comes with additional droop loops as described in [19]. Beyond the basic voltage control loop, the active power-frequency (P-f) droop control and reactive power-voltage (Q-V) droop control are widely used in generating frequency reference $\omega*$ and voltage reference $v*$, respectively. The grid-forming control can be called grid-supporting control with adding the droop control loops. With only grid-forming control, converters cannot be connected

in parallel due to stiff regulation on voltage and frequency. However, grid-supporting controlled VSCs are suitable for parallel operation. A grid-forming VSC can be treated as a special case of a grid-supporting one with droop coefficients of zero [20].

1.3.1.2 Impact of Droop Gains

The stability dynamic impact of droop coefficients have been examined by existing literature. It has been investigated that with increasing P-f droop gain, a low-frequency mode will cause the instability [18, 19, 21–23]. And [21, 22] indicates that Q-V droop gain has a great affect on high-frequency modes. A larger Q-V droop gain will lead the system to unstable condition.

1.3.2 IBR Modeling

1.3.2.1 GFL Modeling

Impedance or admittance modeling in *dq*-domain is presented in [24–26]. They proposed an impedance/admittance model for three-phase grid integrated VSC. VSC feedback control and PLL dynamics are included. It reveals the instability causes and investigate how PLL, control structure parameters impact the impedance frequency responses in *dq*-domain. Bode plots are given to show the frequency responses under different assumptions. Nyquist criterion is adopted to identity the system stability [24, 26, 27]. The synchronization dynamics of current controller and voltage feedforward loop with a low-pass filter (LPF) are discussed in [26]. It shows either increasing or decreasing the cutoff frequency of LPF to make she system stable. This conclusion will also be validated in our examination in Chapter 2. Different from [24–26], [27] builds the VSC output impedance model in positive-sequence and negative-sequence. Current control loop and SRF-PLL are included. The stability criterion is to observe the inverter output impedance in positive and negative sequence with grid impedance. Compared to *s*-domain admittance-based eigenvalue analysis, Nyquist stability criterion may not be accurate as eigenvalue stability criterion. This shortcoming has been proved by [28].

Nonlinear state-space grid-connected PV system state space model, including VSC feedback controls, dc/dc boost converter controls, has been built by B. Pal's group in [29,30]. [29] incorporates

maximum power point tracking (MPPT) and irradiance-driven dynamics. In [30], a state-space model taking into account of all circuit dynamics is derived to examine system responses under irradiance fluctuation, grid faults and frequency distortion. Stability issues related to weak grid have not been investigated in [29, 30]. However, the industry desire a order-reduced simplified modeling. The type-4 wind farms simplified state-space model has been carried out to investigate wind system stability issues [5–8]. Those works are the foundation of PV farms simplified modeling. Furthermore, the modeling work in Chapter 2 makes an improvement on dc side representation. An improved dc voltage assumption will be examined in the proposed modeling, while only constant dc input power is assumed in [7, 8, 31].

1.3.2.2 GFM Modeling

Similar to grid-following converter modeling, there are two approaches to model the grid-forming converters: state-space model and impedance-based modeling. [18] proposed a $dq-$frame impedance model of a grid-forming VSC with droops connected to infinite bus. Each individual component is visualized as a impedance element of a circuit. Their physical interactions is revealed via Bode plots analysis. Frequency-domain spectrum measurement and time-domain dynamic response are adopted for the validation.

A simplified state-space model is the most common apporach to model the grid-forming system till now, which can be found in [12,21–23]. Among them, [21,22] proposed $dq-$ domain linear state-space models for a multiple grid-forming VSC systems. [22] is for a two grid-forming controlled VSC-HVDCs are parallel connected to a AC current source. And [21] is for a microgrid consists of three grid-forming converter. Use the eigenvalue analysis, the P-f droop gains and Q-V droop gains are investigated on the system stability impact from [21, 22]. A reduced 3rd-order state-space model is proposed to matching with EMT dynamic responses in [23]. The stability affected factors are investigated, such as grid impedance, operation level, and power filter time constant. For large scale system modeling, only the grid-forming and grid-following VSCs are modelled in $dq-$frame [12]. Then they are converted to $abc-$frame and interfaced with a large scale system via a network solver. Besides above mentioned linearized small-signal stability analysis modeling, [12]

proposed nonlinear state-space model on grid-forming large-signal analysis via Lyapunov stability criterion and the La Salle's Invariance Principle.

1.3.3 IBR Admittance Identification

The IBR admittance identification is significant for understand the dynamic characteristics. It can be used for not only validating the proposed analytical models on frequency-domain but also extracting the measurement-based admittance model under a black-box condition.

One of the most popular method in industry is frequency scanning [32, 33]. A small signal harmonic will be injected on the d-axis or q-axis voltage under a particular converter working condition. Then measure the current on dq-frame to conduct the admittance model via fast Fourier transform (FFT) analysis. Then convert the measured data to s-domain admittance transfer function using vector fitting [34]. Frequency scanning and vector fitting approaches will be implemented to identify the s-domain admittance-based IBR model in Chapter 4.

Data-driven black-box system identification has been tested in our studies, such as numerical algorithm for subspace state space system Identification (N4SID) [35], Multivariable Output-Error State Space (MOESP) [36], and Eigensystems Realization Algorithm (ERA) [37], are available. Among them, ERA has been adopted to identify reduce-order i/o linear models for system stabilizer design and FACTs controller design in [38]. And [39] has developed a toolbox relying on ERA algorithm to estimate time-domain measurement's transfer function for PV farm admittance estimation. ERA method will be adopted for s-domain admittance modeling for PV side in Chapter 2.

1.4 Research Contributions

Based on above discussion, there are four main research contributions achieved.

- A reduced-order simplified nonlinear dq-frame model is built. The PV system can be studied from small-signal analysis and large-signal simulation, which is not accessed in existing methods. It is examined that the dc-side dynamic can be represented by an equivalent RLC circuit. The proposed simplified model is capable to demonstrate low-frequency oscillations

in a PV grid integration system. The participation factor can pinpoint the most influencing state on the oscillation mode. Furthermore, the open-loop analysis can reveal the sensitivity of controller parameters on stability. All analysis conclusions are validated in EMT testbed simulations.

- Laplace domain admittance model can be identified from measurement data. Two approaches are employed: conventional sinusoidal harmonic injection (frequency scanning method), and step response-based numerical perturbation (ERA method). The measured admittance model can be integrated with a single bus system or a meshed network. Therefore, eigenvalue analysis can be carried out for stability analysis. And extended mode shape tool is developed to explain the dynamic responses at different locations. Compared to the existing admittance-bsed modal analysis using participation factor, voltage and current related observability or controllability, this research can be expended to any measurement.

- Furthermore, the measured admittance model can also be used to conduct fast time-domain simulation. It can convert a given frequency-domain measurement data to time-domain simulation data directly even without building an EMT testbed. A system of a type-4 wind farm with a parallel connected STATCOM is examined as an example. Their *dq*-domain admittance models are obtained via frequency scanning and vector fitting. It can be used to forecast interaction effects between IBR models efficiently.

1.5 Publications

First, the journal publications are listed.

1. M. Zhang, Z. Miao, L. Fan, and S. Shah, *Admittance-based Small-Signal Analysis for a 100% IBR-Penetrated Power Grid Via Frequency Scan*, IEEE PES Transactions on Power Delivery, Under Review.

2. M. Zhang, L. Fan, and Z. Miao, *Reduced-Order Analytical Model of Grid-Connected Solar Photovoltaic System for Low-Frequency Oscillation Analysis*, IEEE Transactions on Sustainable Energy, 2021.

3. L. Fan, Z. Miao, and M. Zhang, *Subcycle Overvoltage Dynamics in Solar PVs*, IEEE Transactions on Power Delivery, 2020.

4. Y. Xu, M. Zhang, L. Fan, and Z. Miao, *Small-Signal Stability Analysis of Type-4 Wind in Series Compensated Networks*, IEEE Transactions on Energy Conversion, 2019.

5. M. Zhang, R. S. Kar, Z. Miao, and L. Fan, *New auxiliary variable-based ADMM for nonconvex AC OPF*, Electric Power Systems Research, 2019

Second, the conference publications are listed.

1. M. Zhang, Z. Miao, and L. Fan, *Measured Admittance Model for Dynamic Simulation of Inverter-Based Resources Using Numerical Laplace Transform*, 2021 North American Power Symposium (NAPS).

2. M. Zhang, Z. Miao, and L. Fan, *Data Analytics of Real-World PV/Battery Systems*, 2019 IEEE Power & Energy Society General Meeting (PESGM).

3. M. Zhang, Z. Miao, and L. Fan, *Power Grid Partitioning: Static and Dynamic Approaches*, 2018 North American Power Symposium (NAPS).

4. M. Zhang, Z. Miao, and L. Fan, *Battery identification based on real-world data*, 2017 North American Power Symposium (NAPS).

5. R. S. Kar, M. Zhang, M. Zhang, and L. Fan, *ADMM for nonconvex AC optimal power flow*, 2017 North American Power Symposium (NAPS).

1.6 Outline of the Dissertation

This dissertation is organized as follows:

Chapter 2 shows the reduced-order simplified analytical modeling for a PV system in weak grid. The proposed model is detailed and compared with EMT tested on frequency responses and time-domain responses. The eigenvalue analysis and participation factor analysis are carried out

to reveal the root cause of a 7-Hz low-frequency oscillation. In addition, some sensitivity analysis is given.

Chapter 3 presents a toolbox for scalable IBR integrated network modeling from two approaches. The first one is extended from the simplified analytical modeling from Chapter 2. While the second approach is small-signal s-domain admittance modeling toolbox, which will be implemented for a 9-bus system in Chapter 4. The eigenvalue analysis indicates they can have same result on oscillation modes identification.

Chapter 4 provides a tutorial on how to conduct admittance-based small-signal analysis for a 100% IBR-penetrated power grid. The IBR admittance is identified via frequency scan method. Then the mode shape analysis can explain a 3-Hz poorly damped oscillation which caused by interaction between two GRM converters.

Chapter 5 introduces a fast conversion from given frequency-domain responses to time-domain simulation using numerical Laplace transform (NLT) method. An example of type-4 wind farm and paralleled STATCOM system under a weak grid is tested via fast time-domain simulations for stability demonstration.

Chapter 6 includes the research works and the plans for future work.

Chapter 2: Reduced-Order Analytical Modeling of PV Systems for Low-Frequency Oscillation Analysis

In a real-world solar photovoltaic (PV) farm, low-frequency oscillations have been reported [3]. This part aims to build a simplified analytical model for a PV system for large-signal simulation and small-signal analysis. Especially, the latter one utilizes eigenvalue analysis and participation factor analysis to reveal influencing factors of the oscillations. There are two simplified analytical models are proposed. The first one model assumes the input power from PV's dc side is known and constant. The second model assumes that PV's dc side is represented by a constant dc voltage behind an impedance. PV dc-side dynamics, e.g, dc/dc boost converter control and maximum power point tracking, are ignored. But the grid-side converter (GSC) controls and electromagnetic dynamics of the grid interconnection are still preserved. Two proposed simplified model are compared with an electromagnetic transient (EMT) testbed with full details on time-time domain simulations, admittance frequency-domain responses, and eigenvalue-based stability analysis. It is found that the second simplified model is found as capable of accurately predicting oscillation stability.

The major objective of this chapter [1] is two-fold.

- A 15th-order nonlinear *dq*-frame model is built with the capability of large-signal simulation and small-signal analysis for a grid-connected solar PV farm. Specifically, the dc-side dynamics are represented by an equivalent circuit and its parameters can be found through the measured dc admittance. Different to many other existing research papers in the literature adopted state-space models designed for grid-following converters, e.g., [28, 40], which are linear models suitable for small-signal analysis only. This model can accurately demonstrate

[1] The majority of this chapter was published in IEEE Transactions on Sustainable Energy [15], 2021. Permissions are included in Appendix A.

low-frequency oscillations in a PV grid integration system. Small-signal analysis based on the model pinpoints influencing factors of the oscillations.

- The proposed simplified models are compared with the EMT testbed with full details on not only time-domain simulation results, but also frequency-domain responses of solar PV admittances. In addition, stability analysis results are compared using system eigenvalues. For the analytical models in the synchronous frame, linear models can be found through numerical perturbation. With linear models, eigenvalues can be computed. For the EMT testbed where three-phase instantaneous voltages and currents are state variables, measurement data-based admittance characterization is adopted to obtain admittance. Not only the conventional sinusoidal harmonic injection or frequency scan is employed but also time-domain step response-based method is employed. With the PV system admittance available and the grid interconnection admittance derived, s-domain admittance-based eigenvalue analysis proposed in 1990s in [41] is utilized for stability analysis. This method is found to lead to accurate stability analysis compared to Bode plot stability criterion [42].

The remainder of the part is organized as follows. The first section introduces the 400-kW PV farm grid integration EMT testbed. Low-frequency oscillations are demonstrated. The admittance of the PV farm is also characterized. s-domain admittance-based eigenvalue analysis is then conducted to find stability limit. The second section describes the simplified models and presents the comparison results on dynamic simulation, admittance, and eigenvalue analysis. The third section presents the participation factor analysis of the selected simplified model. The fourth section conducted controller parameter sensitivity analysis and EMT validation. Finally it is concluded in the last section.

2.1 Detailed EMT Testbed

The testbed is developed based on the 400-kW grid-connected PV farm demo in MATLAB/SimPowerSystems [43]. A 400 kW 260 V PV system is integrated into a 120 kV grid through a step transformer, 25 kV line, and another step-up transformer.

The transmission topology and converter controls have been tuned for this research. The topology diagram is shown in Fig. 2.1. The GSC assumes PCC voltage oriented grid-following vector control and it regulates dc-link voltage and PCC voltage. The phase-locked loop (PLL) has three-phase PCC voltage as the input and outputs the PCC voltage angle. The PLL is also used to synchronize the converter to the grid. Details of the converter control can refer to Fig. 2.13. The PV farm consists of four PV arrays connected in parallel. Each array has a capability of 100 kW at 1000 W/m^2 sun irradiance.

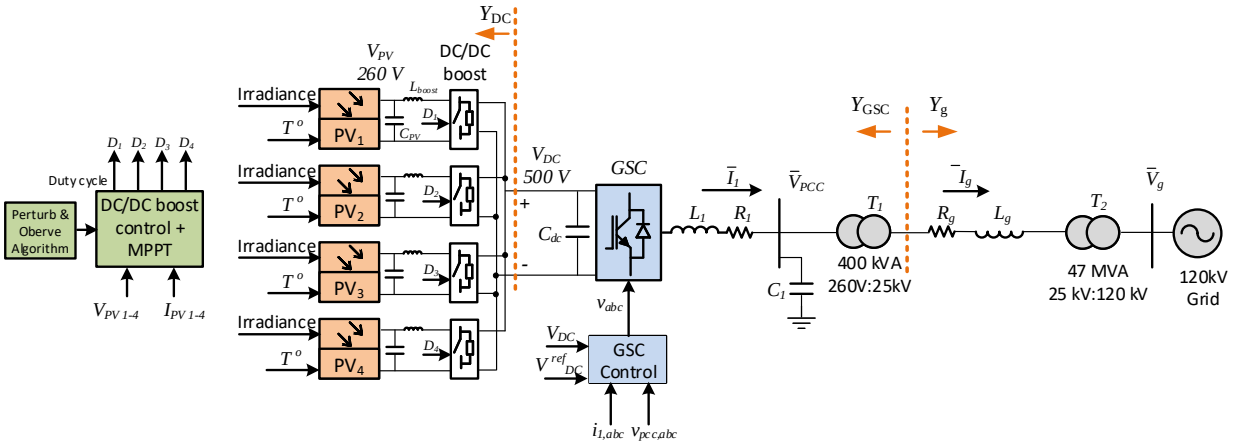

Figure 2.1: EMT testbed 400-kW grid-connected PV farm

The PV voltage (V_{PV}) is the PV array output voltage, or the input voltage to a dc/dc boost converter. The dc/dc boost converter control realizes MPPT, which adopts "perturb and observe" technique. The dc/dc booster's output voltage is at 500 V level. This 500 V dc voltage is converted to a three-phase 260 V ac voltage by a VSC. A shunt capacitor (C_1) is connected at the PCC bus to provide reactive power. Two transformers (T_1, T_2) step the 260 V ac voltage to 25 kV and 120 kV, respectively. The system parameters are given in Table 2.1.

The steady-state limits of the system, denoted by the aggregated transmission system (from the PCC bus to the 120 kV grid) reactance X_g, can be found by load flow. The transmission system resistance is assumed to be 10% of the reactance. Table 2.2 presents the two limits: 1.16 pu when the GSC is in PCC voltage control mode and 0.74 pu when the GSC is in reactive power control mode. In both cases, the real power delivery from the GSC to the PCC bus is kept at 0.935 pu.

Table 2.1: PV system parameters

Description	**Parameters**	**Value**
Power base	S_{base}	400 kW
Power level	P_{PCC}	0.935 pu
System frequency	f_{base}	60 Hz
Converter filter	R_1	0.15/50 pu
	X_1	0.15 pu
Shunt capacitor	C_1	0.25 pu
DC-link capacitor	C_{dc}	0.054 F
Transmission system	R_g	$0.1X_g$
Inner loop	K_{pi}, K_{ii}	0.3, 5
DC-link control loop	K_{pp}, K_{ip}	1, 100
V_{ac} control loop	K_{pv}, K_{iv}	1, 100
Q control loop	K_{pq}, K_{iq}	1, 100
PLL	$K_{p,\text{PLL}}$, $K_{i,\text{PLL}}$	60, 1400
Feedforward filter	T_{VF}	0.001

Table 2.2: Steady-state limits

Control mode	$P_{\text{PCC}} = 0.935$ pu
PCC voltage control: $V_{\text{PCC}} = 1.0$ pu	$X_g = 1.16$ pu
Reactive power control: $Q_{\text{PCC}} = 0$ pu	$X_g = 0.74$ pu

Low-frequency oscillations at $7 \sim 8$ Hz can be observed when the transmission line impedance X_g is 1.0 pu. The GSC assumes dc-link voltage control mode in the d-axis and PCC voltage control mode in the q-axis. Fig. 2.2 (a) and (b) present the system dynamic responses when the PCC voltage control's order (V^*_{PCC}) steps from 1.0 pu to 0.99 pu at $t = 4$ s.

It can be clearly seen that the system is at the marginal stability condition. Fig. 2.2 (a) shows that 7 Hz oscillations appear in PV's 500 V dc-link voltage, dc-side current and power. Fig. 2.2 (b) shows that 7 Hz oscillations appear in PV's ac side dq-frame current and voltage as well as real power and reactive power measured at the PCC bus.

Thus, it can be found that oscillations reduce the limit of operation from $X_g = 1.16$ pu to $X_g = 1.0$ pu.

Notation of Fig. 2.2: V^*_{PCC} steps from 1.0 to 0.99 at $t = 4$ s. (a) Detailed testbed: dc side variables (duty cycle of the dc/dc boost converter, PV side voltage, boost converter output voltage, dc side current and dc side power); (b) Detailed testbed: ac side variables (dq-axis GSC current to

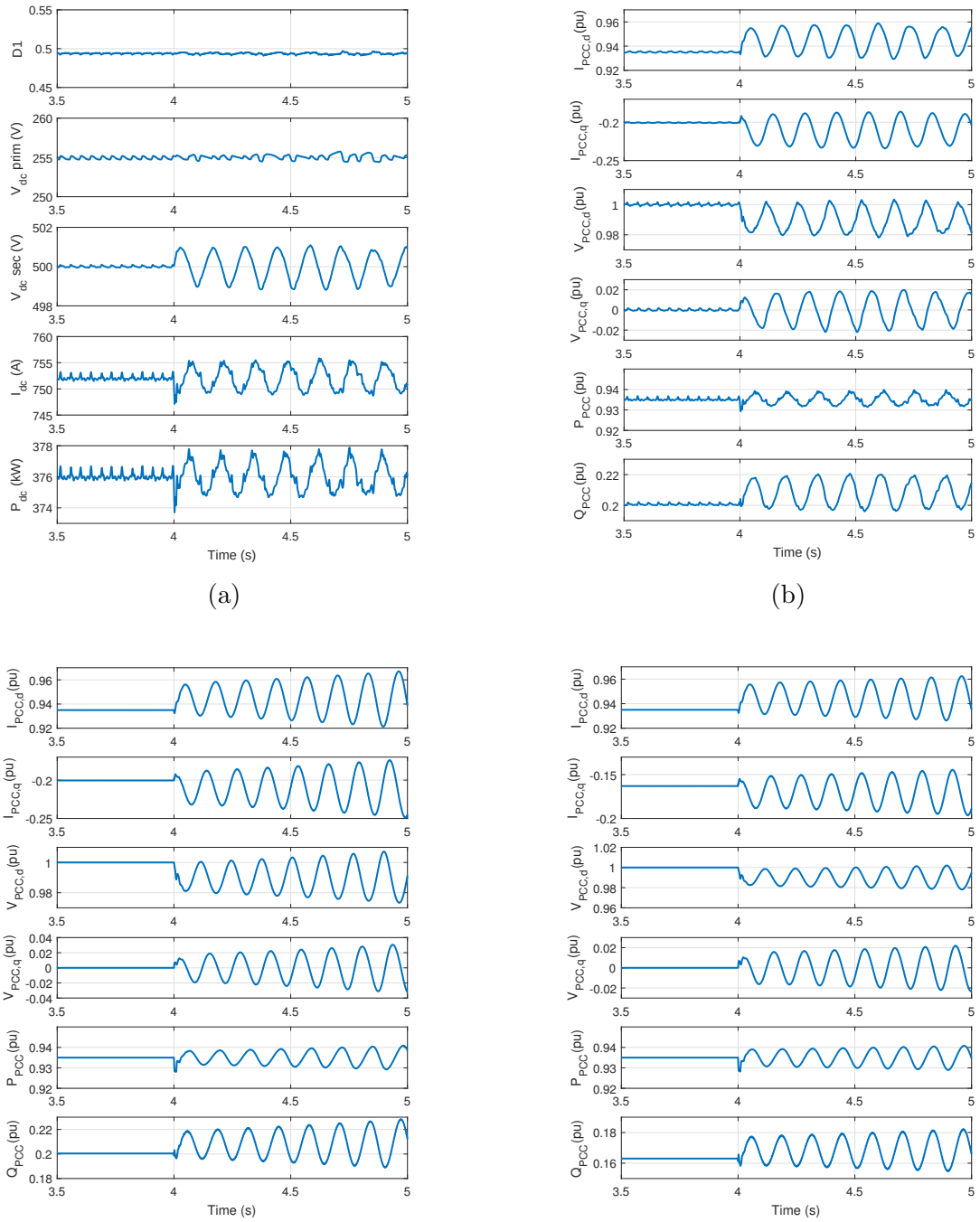

Figure 2.2: Dynamic responses of the EMT testbed with full details (a)(b) and two simplified models (c)(d)

the PCC bus, dq-axis PCC bus voltage, and real and reactive power to PCC bus), $X_g = 1.0$ pu; (c) Constant dc voltage simplified model: ac side variables (dq-axis GSC current to the PCC bus, dq-axis PCC bus voltage, and real and reactive power to PCC bus), $X_g = 1.0$ pu; (d) Constant input power simplified model: ac side variables (dq-axis GSC current to the PCC bus, dq-axis PCC bus voltage, and real and reactive power to PCC bus), $X_g = 0.96$ pu.

2.1.1 Solar PV Admittance Characterization

Harmonic injection method or frequency scan method is the most popular method applied for admittance or impedance characterization [32, 44–46]. A measurement testbed is first built with a PV farm connected to a voltage source at the measurement point. The measurement point has been notated as the dotted line after the 260 V/25 kV transformer in Fig. 1. First, the PV farm's operating condition, defined by the measured real power and reactive power to the PCC bus from the converter and the PCC bus voltage magnitude, is set to be the same as the EMT testbed. The dq-frame admittance characterization relies on d-axis voltage perturbation and q-axis voltage perturbation.

For harmonic injection method or frequency scan, the q-axis voltage is kept intact, sinusoidal injection at a frequency ω_p with a known magnitude is added on top of the d-axis voltage. The dq-axis currents from the converter are measured and the harmonic components at ω_p frequency are found via fast Fourier transform (FFT). From this set of experiment, three phasors are found $\Delta v_d(j\omega_p)$, $\Delta i_d(j\omega_p)$, and $\Delta i_q(j\omega_p)$. Thus, the admittance matrix's dd and qd components at ω_p frequency can be found as

$$Y_{dd}(j\omega_p) = -\frac{\Delta i_d(j\omega_p)}{\Delta v_d(j\omega_p)},\ Y_{qd}(j\omega_p) = -\frac{\Delta i_q(j\omega_p)}{\Delta v_d(j\omega_p)}.$$

Similarly, the dq and qq components can be found by v_q perturbation. To obtain the admittance measurement for a span of frequency range, hundreds of experiments need to be carried out. Fig. 2.4a presents the Bode plot of the measured admittance obtained by frequency scan.

An alternative method for admittance characterization is to use time-domain data. When the time-domain data of the input and output channels are obtained, well-known system identification algorithms, such as numerical algorithm for subspace state space system Identification (N4SID) [35], Multivariable Output-Error State Space (MOESP) [36], and Eigensystems Realization Algorithm (ERA) [37], can be employed. Among them, ERA has been applied in power systems to identify reduced-order input/output linear models for power system stabilizer design and FACTs controller design [38]. An in-house toolbox relying on ERA algorithm to estimate time-domain measurement's transfer function has been designed for PV farm admittance estimation in this research. Details of ERA can be found in a tutorial paper from the authors' research group [39].

The perturbation is designed as a step change in d-axis or q-axis voltage. Each small-signal perturbation generates two time-domain responses: dq-axis currents exporting from the PV farm to the voltage source: $i_d^{(k)}(t)$ and $i_q^{(k)}(t)$, where $k = 1, 2$ notates the index of each experiment. With the transfer functions of $i_d^{(k)}(s)$ and $i_q^{(k)}(s)$ being identified, the admittance model can be found as:

$$Y_{\text{GSC}} = -\begin{bmatrix} \frac{i_d^{(1)}(s)}{v_d^{(1)}(s)} & \frac{i_d^{(2)}(s)}{v_q^{(2)}(s)} \\ \frac{i_q^{(1)}(s)}{v_d^{(1)}(s)} & \frac{i_q^{(2)}(s)}{v_q^{(2)}(s)} \end{bmatrix} = -\frac{s}{p}\begin{bmatrix} i_d^{(1)}(s) & i_d^{(2)}(s) \\ i_q^{(1)}(s) & i_q^{(2)}(s) \end{bmatrix} \tag{2.1}$$

where p is the size of perturbation and $v_d^{(1)}(s) = v_q^{(2)}(s) = p/s$. The negative sign is due to the current direction as flowing out of the PV.

The measurement point is close to the PCC bus. A small impedance (e.g., $0.01 + j0.1$ pu) is usually inserted between the PCC bus and the measurement point.

First, 2% step change is applied to the d-axis voltage and $i_{g,d}^{(1)}$, $i_{g,q}^{(1)}$ are measured. Next, 2% step change is applied to the q-axis voltage and $i_{g,d}^{(2)}$, $i_{g,q}^{(2)}$ are measured.

$i_{g,d}^{(1)}$, $i_{g,q}^{(1)}$, $i_{g,d}^{(2)}$, $i_{g,q}^{(2)}$ are fed into the toolbox for estimation. The estimated currents by the toolbox are plotted along with the original measured data in Fig. 2.3. The estimated system order is defined as 18. Additionally, the sampling period is 0.25 second with 2 kHz sampling rate. The Bode plots of the estimated admittance are shown as the solid lines in Fig. 2.4a.

It can be seen that the time-domain data based estimation and frequency scan method lead to very similar admittance. In addition, frequency scan leads to admittance measurements at those perturbed frequencies while the time-domain data based method leads to an analytical model in s-domain. The latter can be directly used for eigenvalue analysis.

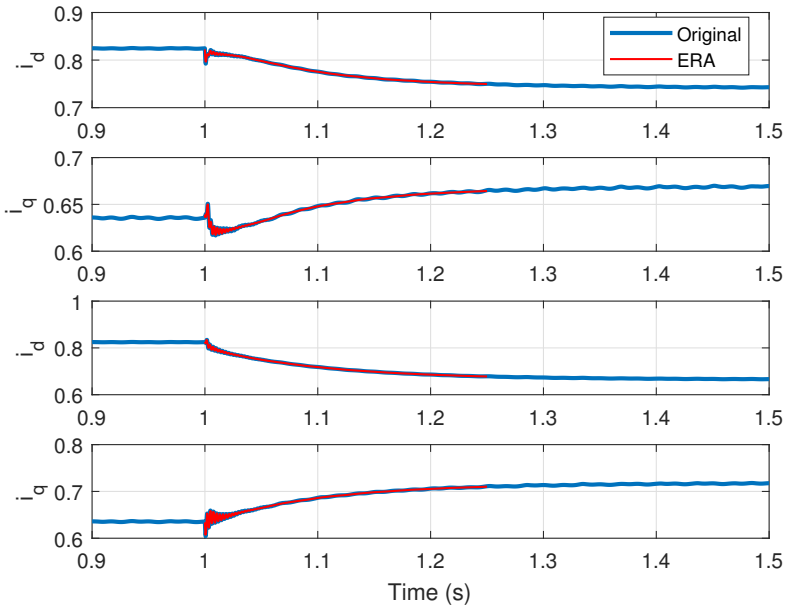

Figure 2.3: Original measurement and the reconstructed signal using estimated eigenvalues

2.1.2 s-domain Admittance-based Eigenvalue Analysis

In the power grid industry, small-signal analysis is usually conducted by examining the eigenvalues of linear models, which are obtained from nonlinear dq-frame models through numerical perturbation [47]. On the other hand, a system can be divided into subsystems. With each subsystem viewed as an admittance, the entire system may be viewed as a circuit consisting of admittances. Stability analysis can be carried out using the network admittance. The two approaches lead to the same eigenvalues with benchmarking results presented in [14].

The system in Fig. 1 is viewed at the measuring point with two shunt admittances: Y_{GSC} and Y_g, where Y_{GSC} is the admittance of the subsystem at the left of the measurement point and Y_g

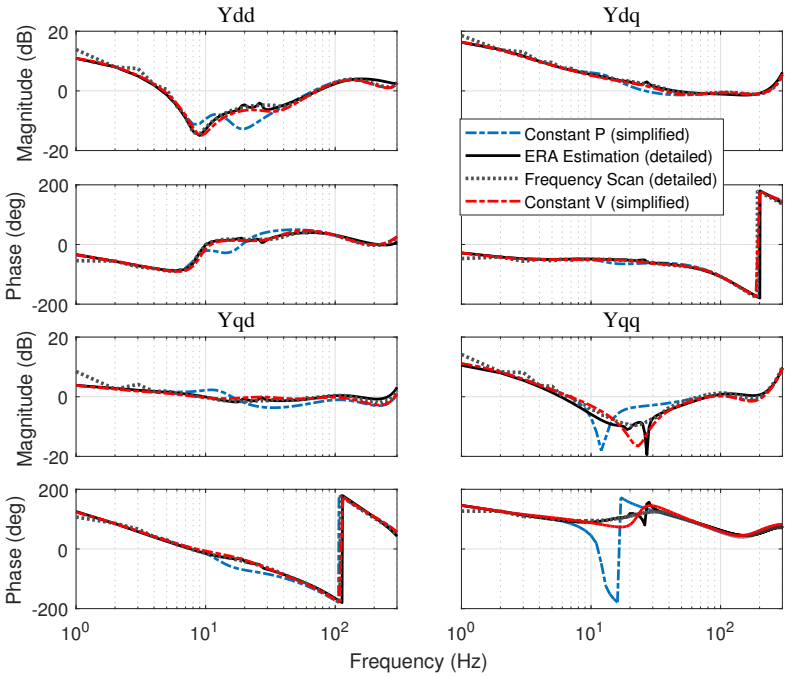

(a)

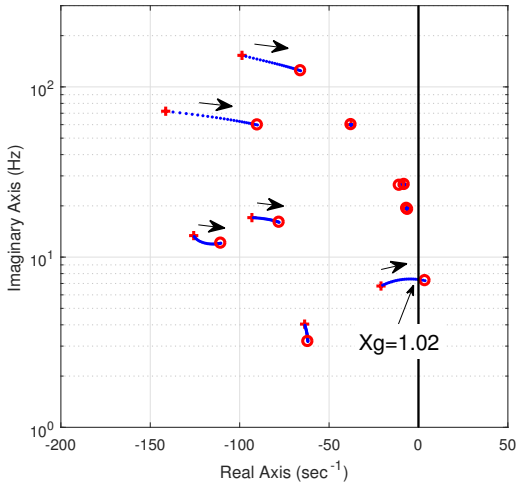

(b)

Figure 2.4: Bode plots of the admittance models and eigenvalues of the detailed model where X_g varies from 0.5 to 1.1 pu

is the Norton equivalent admittance of the grid interconnection at the right of the measurement point.

Applying circuit analysis, it can be found the relationship between the injected small current at the measuring point and the voltage of the measuring point as follows.

$$\begin{bmatrix} \Delta i_{d,\text{inj}} \\ \Delta i_{q,\text{inj}} \end{bmatrix} = (Y_{\text{GSC}} + Y_g) \begin{bmatrix} \Delta v_d \\ \Delta v_q \end{bmatrix} \tag{2.2}$$

If (2.2) is viewed as an input/output system, then the PCC voltage is the output (notated as y) and the injected current is the input (notated as u). Hence, the transfer function matrix notated as $G(s)$ from u to y is:

$$G(s) = (\underbrace{Y_{\text{GSC}} + Y_g}_{Y})^{-1} \tag{2.3}$$

where

$$Y_g = \begin{bmatrix} R_g + sL_g & -\omega_0 L_g \\ \omega_0 L_g & R_g + sL_g \end{bmatrix}^{-1},$$

and ω_0 is the nominal frequency 377 rad/s.

Poles of $G(s)$ are the eigenvalues of the system. In turn, roots of $\det(Y)$ or the zeros of the s-domain admittance matrix Y are the eigenvalues of the system.The eigenvalues of whole system can be found as the zeros of $(Y_{\text{GSC}}+Y_g)$. The aforementioned eigenvalue analysis tool was proposed in [41] by Semlyen and termed as s-domain admittance based eigenvalue analysis. Most recently, this approach has been adopted in [42, 48] for power grids with IBR penetrations.

By varying grid side admittance, the whole system eigenvalue trajectory can be found and presented in Fig. 2.4b. The marginal condition $X_g = 1.02$ pu is accurately predicted and corroborates with the simulation results in Fig. 2.2(a)(b).

2.2 Simplified Analytical Models

The simplified nonlinear analytical models are based on a per unit circuit diagram shown in Fig. 2.5. Resistances and inductances of the transformers and the transmission line are aggregated into R_g and L_g, respectively.

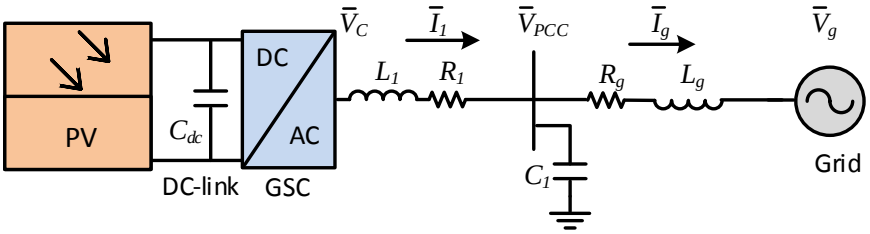

Figure 2.5: Per unit circuit diagram of a grid connected PV farm

2.2.1 DC Side Representation

The dc side dynamic has a coupling effect on ac side [49].

Thus, it is obvious that different dc side representations will have affect on the admittance viewed from the ac side.

Besides constant input power assumption adopted in [8], constant dc voltage assumption is examined. The circuit representations are presented in Fig. 2.6. Fig. 2.6(a) presents the constant input power assumption. In the case of constant input power, the dc side is assumed to be a controllable current source with its power P_{pv} given.

Fig. 2.6(b) is the constant dc voltage representation. The dc side is treated as an equivalent circuit: a constant dc voltage source behind an RLC circuit.

For constant power model, the input power from PV dc side to the dc-link is given as P_{pv}. The dc-link capacitor dynamic can be expressed by (2.4).

$$\frac{Cdc}{2}\frac{dVdc^2}{dt} = Ppv - Pconv \tag{2.4}$$

where Ppv is a constant value, and $Pconv$ is computed by the ac side variables (converter output voltage v_{dq} and current i_{1dq}) and $P_{\text{conv}} = v_d i_{1d} + v_q i_{1q}$ in per unit. The block diagram is presented

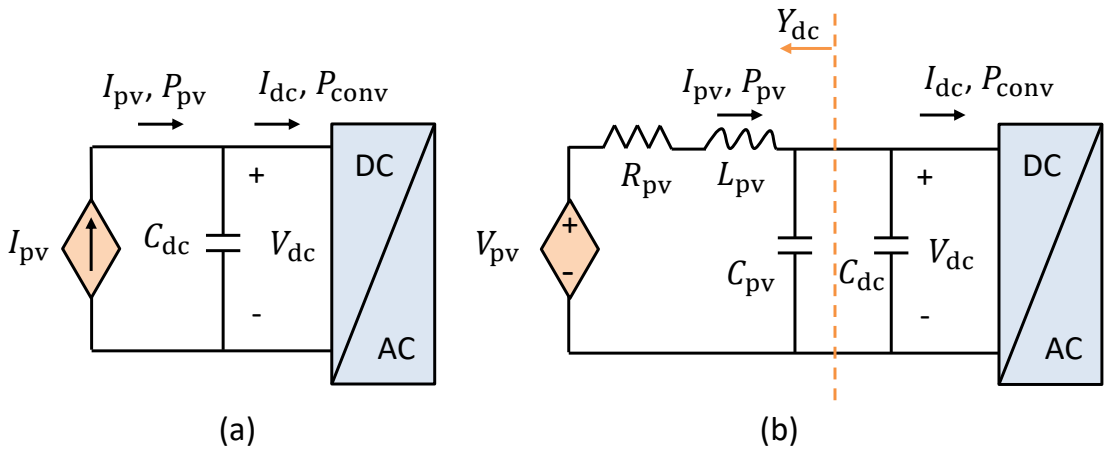

Figure 2.6: Simplified models to represent the dc-side dynamics of constant Ppv model (a) and constant Vpv model (b)

in Fig. 2.7 (a). The output Vdc^2 in per unit will be fed into VSC control in the analytical model block diagram in Fig. 2.13.

For constant voltage model, the shunt capacitor C_{pv} can be ignored if $C_{\text{pv}} \ll C_{\text{dc}}$. The dc-link capacitor dynamics and the inductor dynamics can be expressed in (2.5) and (2.6). Fig. 2.7 (b) presents the block diagram for the constant dc voltage source model.

$$\frac{Cdc}{2}\frac{dV_{\text{dc}}^2}{dt} = IpvV_{\text{dc}} - Pconv \tag{2.5}$$

$$Lpv\frac{dIpv}{dt} = Vpv - V_{\text{dc}} - IpvRpv \tag{2.6}$$

To determine R_{pv} and L_{pv}, the admittance viewed at the dc-link bus of the EMT testbed will be measured via the sinusoidal harmonic injection. The dc side measurement point (Y_{DC}) is marked in Fig. 2.1. The frequency responses are shown by Bode plots in Fig. 2.8 (a) with the three dotted lines representing three different irradiance conditions.

R_{pv}, L_{pv}, and C_{pv} are properly selected to fit the frequency responses of the measured admittance. In Fig. 2.8 (b), the constant voltage with $R_{\text{pv}} = 0.42\,\Omega$, $L_{\text{pv}} = 0.003$ H, $C_{\text{pv}} = 1e^{-4}$ F is adopted to represent the dc side system when the irradiance is 1000 W/m^2 or 800 W/m^2, since those two scenarios have very similar frequency responses. The constant voltage with $R_{\text{pv}} = 0.6\,\Omega$,

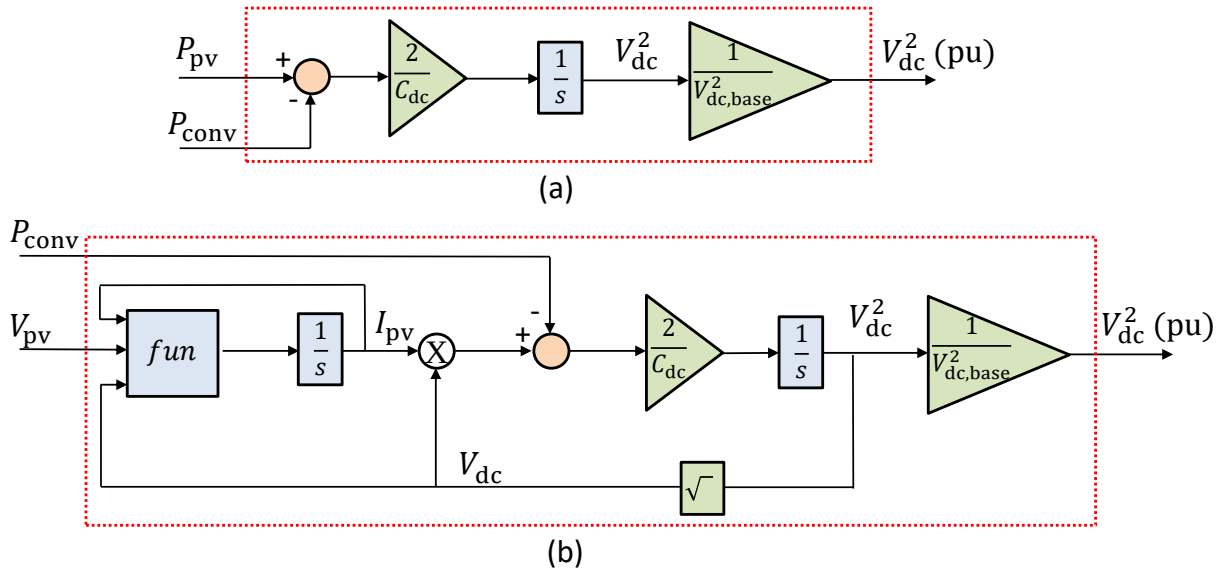

Figure 2.7: DC-side dynamics modeling of constant *Ppv* and constant *Vpv*

$L_{\text{pv}} = 0.003$ H, and $C_{\text{pv}} = 6e^{-5}$ F is adopted to represent the dc side system when the irradiance is 500 W/m^2. They are listed in Table 2.3. Notice that C_{pv} is very small comparing to C_{dc} (0.0543 F), so C_{pv} can be ignored in the simplified model.

Table 2.3: The corresponding R_{pv}, L_{pv}, and C_{pv} regarding different irradiance conditions

Irradiance (detailed)	Constant voltage R_{pv}, L_{pv} (simplified)
1000 W/m^2	$R_{\text{pv}} = 0.42\,\Omega$, $L_{\text{pv}} = 0.003$ H, $C_{\text{pv}} = 1e^{-4}$ F
800 W/m^2	$R_{\text{pv}} = 0.42\,\Omega$, $L_{\text{pv}} = 0.003$ H, $C_{\text{pv}} = 1e^{-4}$ F
500 W/m^2	$R_{\text{pv}} = 0.60\,\Omega$, $L_{\text{pv}} = 0.003$ H, $C_{\text{pv}} = 6e^{-5}$ F

As a comparison, the Bode plot of constant power assumption is presented as the black dash-dot line in Fig. 2.8 (b). The dc side can be viewed as a resistor under the constant dc power source assumption:

$$\Delta P_{\text{pv}} = V_{\text{dc}}\Delta I_{\text{dc}} + I_{\text{dc}}\Delta V_{\text{dc}} = 0$$
$$R_{\text{pv}} = -\frac{\Delta V_{\text{dc}}}{\Delta I_{\text{dc}}} = \frac{V_{\text{dc}}}{I_{\text{dc}}},$$

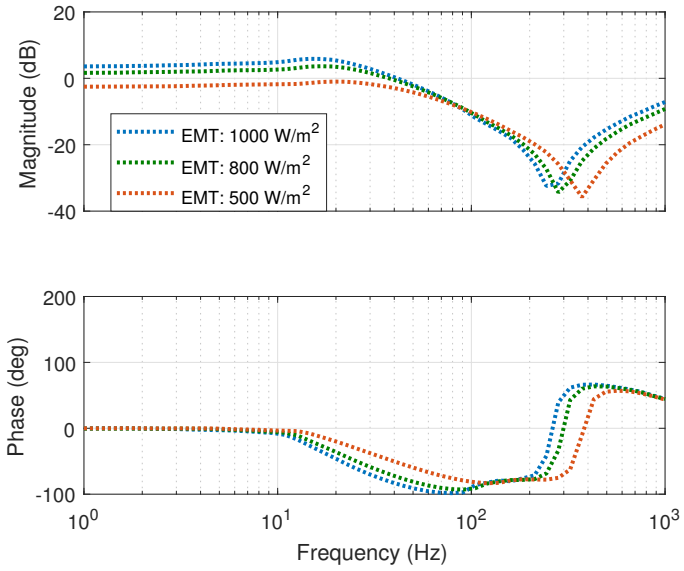

(a)

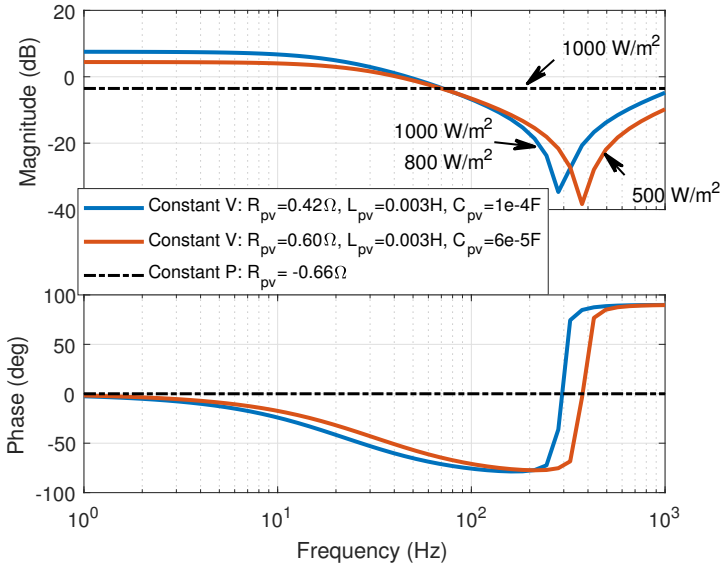

(b)

Figure 2.8: The DC side admittance viewed from the dc-link bus in measured EMT testbed and simplified model

where I_{dc} is the dc current when the irradiance is 1000 W/m^2. Significant difference exists between this admittance and the measured admittance.

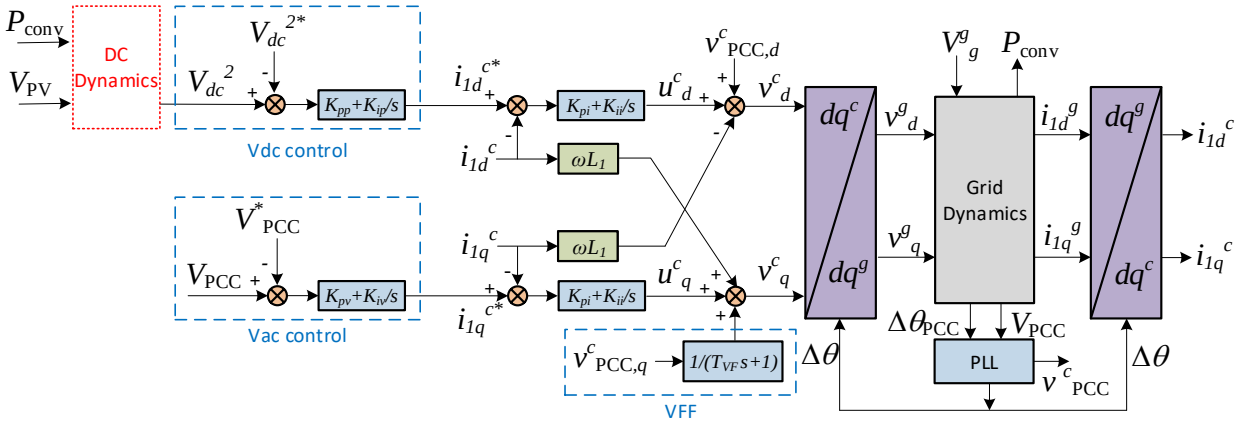

Figure 2.9: Block diagram of the grid-connected VSC dynamic model

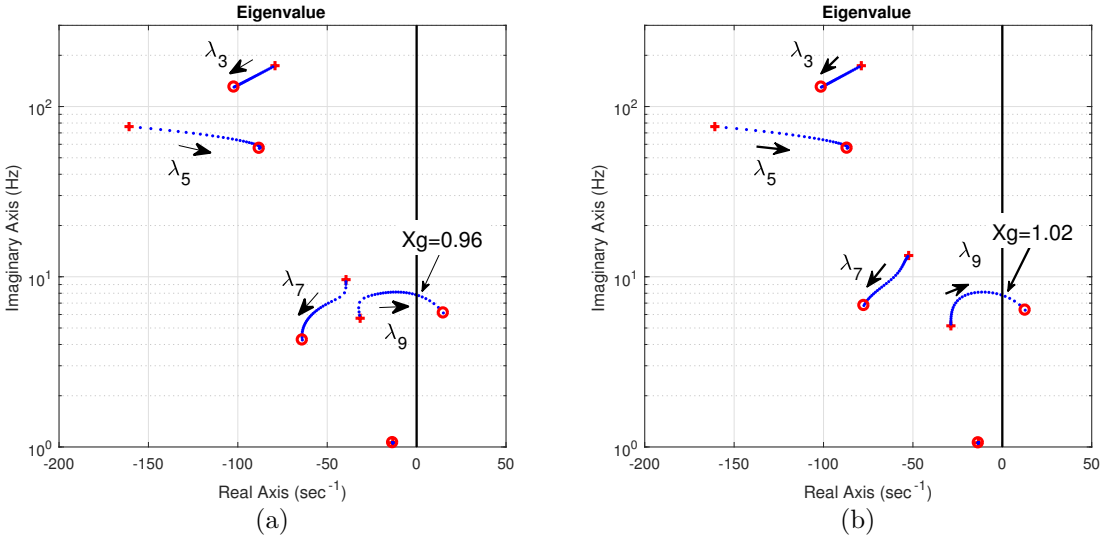

Figure 2.10: Eigenvalues of simplified models where X_g varies form 0.5 to 1.10 pu with each step 0.02 pu under constant input power (a) and constant dc voltage (b)

2.2.2 Grid-Connected VSC Representation

Modeling of grid-connected VSC has been addressed in the authors prior work, e.g., [6–8]. Brief explanation of the modeling assumption is given in the following.

The block diagram of the *dq*-frame based model is shown in Fig. 2.13. The two simplified models have orders of 14 (constant input power assumption) and 15 (constant dc voltage assumption).

This dynamic model consists of a 6-order grid dynamic block where two inductors and one shunt capacitor dynamics are considered, a 2-order synchronous reference frame-based PLL, a 4-order vector control, a 1-order voltage feedforward low-pass filter and a 1-order (for constant power assumption) or 2-order (for constant dc voltage assumption) dc side dynamics.

The grid-connected converter model is based on two dq reference frames: converter-based frame (denoted as superscript c) for vector control and grid frame (denoted as superscript g) for grid dynamics. At steady-state, the d-axis of the converter frame aligns with the PCC voltage space vector, while the d-axis of the grid frame aligns with the grid voltage space vector. The converter frame is based on the PLL output angle. Thus, the converter frame leads the grid frame by the PLL output angle $\Delta\theta$.

More details on dq-frame based dynamic modeling, PLL details for a grid-connected VSC in real power control and ac voltage control mode can be found in the authors' prior work [6–8].

The converter control is based on the converter frame. In the outer loop of the converter control, d-axis is for dc-link voltage regulation while the q-axis is for ac voltage or reactive power regulation. The dc-link voltage control generates d-axis current reference i_{1d}^{c*} while the voltage or var control generates q-axis current reference i_{1q}^{c*}. The inner current controls have faster bandwidth to track the current orders. Current decoupling feedforward [50] has been adopted in the inner control. The q-axis voltage feedforward $v_{\mathrm{PCC},q}^{c}$ with a voltage feedforward filter (VFF) has been added in VSC control to enhance the system stability.

The converter control leads to controllable dq-axis converter output voltage in the converter frame. In the dynamic model block diagram in Fig. 2.13, the converter is treated as controllable voltage source for the circuit. This voltage source is converted into a voltage source in the grid frame and fed into the grid dynamics block. Outputs of the grid dynamics block are dq-axis converter current and PCC voltage in the grid frame. In turn, the PCC voltage phase angle $\Delta\theta_{\mathrm{PCC}}$ are also exported to feed into the PLL block to generate the PLL angle $\Delta\theta$. $\Delta\theta$ is used as the input for frame conversion. Real and reactive power of converter output may also be calibrated by the grid dynamics block.

Thus, the entire analytical model is built in dq-frames. The model is a nonlinear model since no assumption of linearization has been made. For example, power expressions are nonlinear to voltage and currents; frame conversion uses sine and cosine of the PLL output angle. At balanced operating conditions, this model has state variables as constants at equilibrium points. Numerical perturbation can be implemented to easily extract the linearized models for small-signal analysis.

2.2.3 Comparison with EMT Testbed

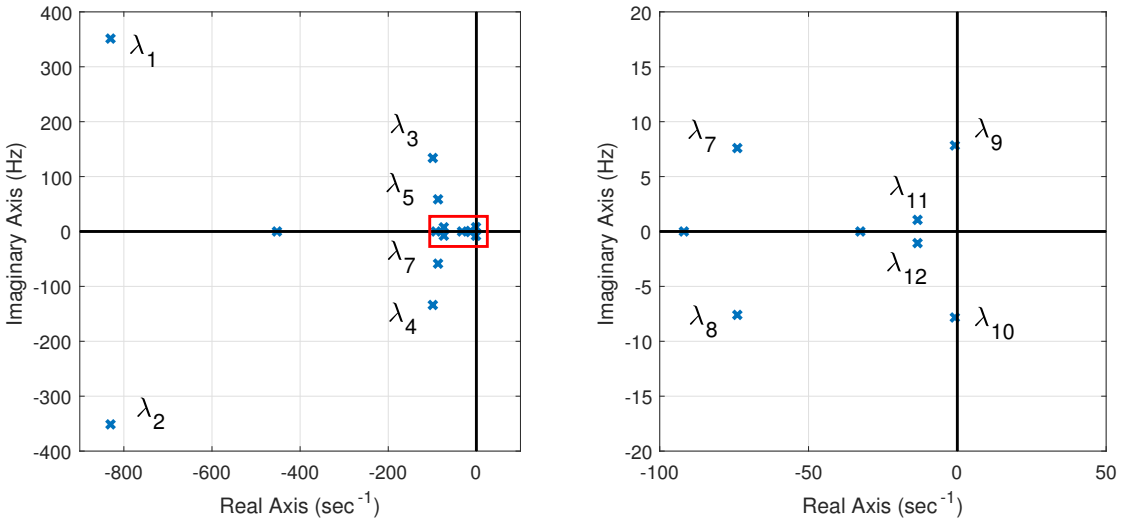

Figure 2.11: Constant dc voltage model's eigenvalues when $X_g = 1.0$ pu

Fig. 2.10 presents the loci of eigenvalues with a varying X_g. It can be seen that the dominant 7.8 Hz mode moves towards the right half plane (RHP) when X_g increases or the grid becomes weaker. Thus, both of the two simplified models can demonstrate low-frequency oscillations due to weak grid interconnection. The constant input power model identifies $X_g = 0.96$ pu as the marginal condition, while the constant dc voltage model identifies $X_g = 1.02$ pu as the marginal condition. Note that the detailed model indicates that 1.02 pu is the marginal condition. The prediction of the constant dc voltage model is the same as that from the s-domain admittance-based eigenvalue analysis in Fig. 2.4b.

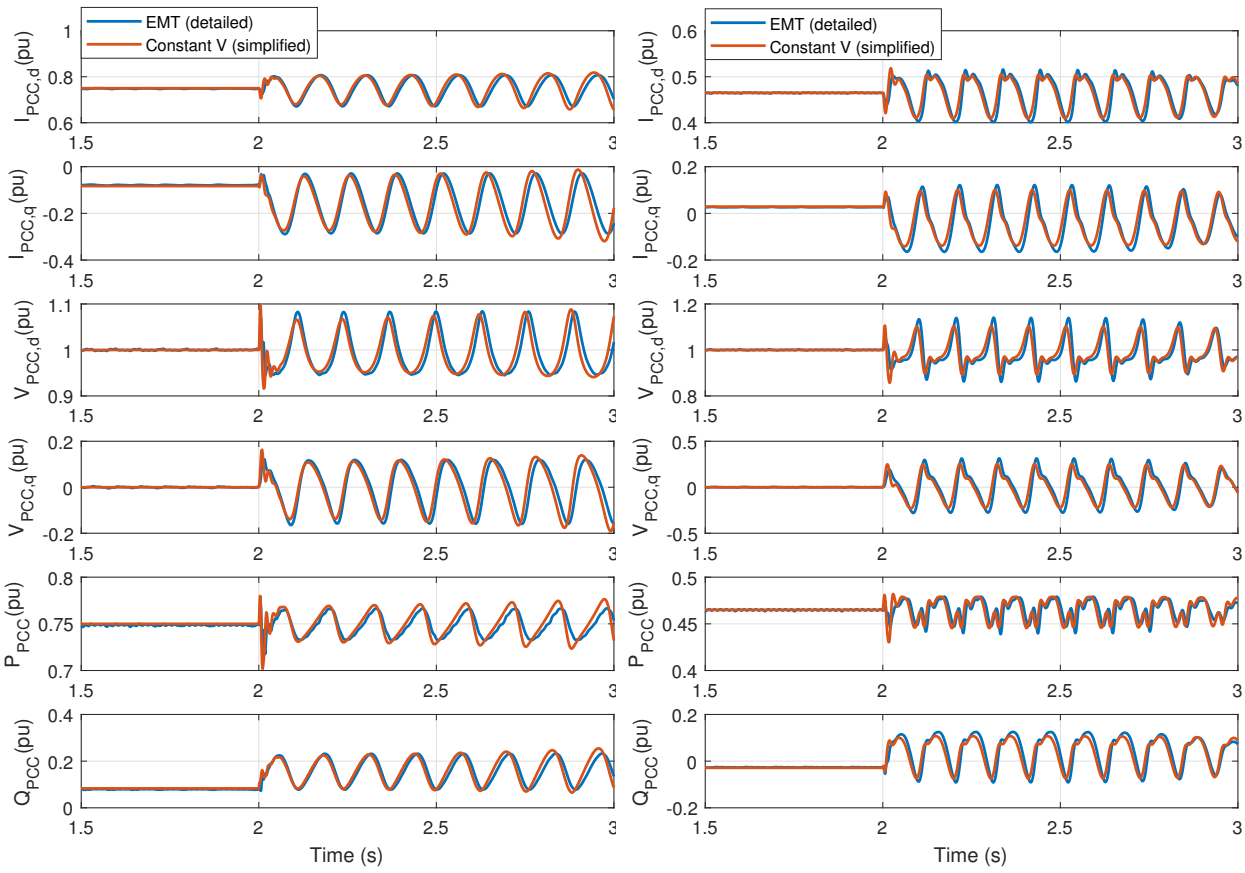

Figure 2.12: Time-domain dynamic responses of line tripping in the EMT testbed and the constant voltage model

Dynamic simulation with irradiance at 1000 W/m^2 is carried out using the simplified models. Fig. 2.2 (c)(d) present the constant dc voltage model 's and constant input power model's dynamic responses at the corresponding marginal conditions (X_g at 1.00 pu and 0.96 pu, respectively). The dynamic event is a small change in the PCC voltage order. It can be seen that 7 $\sim$ 8 Hz oscillations appear in both models. Furthermore, another two irradiance conditions are examined using constant voltage simplified model and the simulation results line tripping events are presented in Fig. 2.12. (a) X_g steps from 1.20 to 1.30 p.u. Blue line: irradiance at 800 W/m^2 in the EMT testbed. Red line: $R_{\text{pv}} = 0.42\,\Omega$, $L_{\text{pv}} = 0.003$ H in the simplified model. (b) X_g steps from 2.00

to 2.19 p.u. Blue line: irradiance at 500 W/m^2 in the EMT testbed. Red line: $R_{\text{pv}} = 0.6\,\Omega$, $L_{\text{pv}} = 0.003$ H in the simplified model.

Finally, frequency-domain responses of the two simplified models and EMT detailed model are compared. The Bode plots are presented in Fig. 2.4a. It can be seen that the two simplified models and the detailed model have comparable frequency-domain responses, especially in the low-frequency range. Among the two simplified models, the constant dc voltage model is more similar to the EMT detailed model. It is found that the qq component of the admittance (Y_{qq}) shows notable difference in magnitude and phase angle near 10 Hz for the constant input power model and the detailed EMT model. That is due to the dc side frequency responses mismatching shown in Fig. 2.8 (b).

Based on comparison of time-domain simulation results, eigenvalue-based stability analysis results, and frequency-domain responses of admittances, it is found that the 15th-order constant dc voltage model is more accurate for low-frequency oscillation analysis.

2.3 Eigenvalue and Participation Factor Analysis

In this section, eigenvalue and participation factor analysis is conducted for the simplified model with constant dc voltage assumption. Fig. 2.11 gives an overall eigenvalue plot for the constant dc voltage model at the marginal condition of $X_g = 1$ pu. The system has 15 eigenvalues with ten complex conjugate eigenvalues denoting five oscillation modes. These ten eigenvalues are noted as λ_i, where $i = 1, \cdots, 10$. Among them, λ_9 and λ_{10} notate the an oscillation mode of 7.4 Hz close to the imaginary axis.

The participation factor table for the constant power model is presented in Table 2.4. The participation factor table for the constant voltage model is presented in Table 2.5 for the five modes. Those two models have very similar participation factor analysis results. In Table 2.5, the leftmost column notates the 15 state variables. Those participation factors with relatively large values are highlighted in bold. Based on the participation factor table, Table 2.6 lists the most relevant factors for the five oscillation modes.

Table 2.4: Participation factor table for the constant dc power model.

State Variable	$\lambda_{1,2}$	$\lambda_{3,4}$	$\lambda_{5,6}$	$\lambda_{7,8}$	$\lambda_{9,10}$
V_{dc}^2	0.0002	0.037	0.029	**0.2526**	**0.246**
i_{1d}^g	**0.3633**	0.0752	0.0994	0.0208	0.0035
i_{1q}^g	**0.1343**	0.17	**0.1163**	0.0476	0.0059
i_{gd}^g	0.0471	**0.1446**	**0.2865**	0.0589	0.0146
i_{gq}^g	0.0186	**0.2851**	**0.5107**	**0.1092**	0.0385
$v_{\text{PCC},d}^g$	**0.3731**	**0.1568**	**0.1199**	0.0293	0.0105
$v_{\text{PCC},q}^g$	0.1117	**0.3075**	**0.1035**	0.0167	0.0043
θ	0.0117	0.0095	**0.1064**	**0.7867**	**0.3109**
$\Delta\omega$	0.0001	0.0003	0.0066	**0.3591**	**0.1335**
VFF	0.164	0.1187	0.433	0.0912	0.0392
V_{dc} PI	0	0.0043	0.0078	**0.5153**	**0.2217**
V_{PCC} PI	0.0018	0.014	**0.1143**	**0.638**	**0.3596**
q-axis current PI	0.0012	0.0014	0.0182	0.017	0.0118
d-axis current PI	0.0001	0.0012	0.0097	0.0536	0.0086

Table 2.5: Participation factor table for the constant dc voltage model

State Variable	$\lambda_{1,2}$	$\lambda_{3,4}$	$\lambda_{5,6}$	$\lambda_{7,8}$	$\lambda_{9,10}$
V_{dc}^2	0.0002	0.0391	0.0353	**0.4985**	**0.2519**
i_{1d}^g	**0.3832**	0.0612	0.0968	0.0135	0.0047
i_{1q}^g	**0.1146**	**0.1605**	**0.1207**	0.0481	0.0087
i_{gd}^g	0.0469	**0.1242**	**0.3302**	0.0546	0.0193
i_{gq}^g	0.0161	**0.3067**	**0.4698**	**0.1089**	0.0482
$v_{\text{PCC},d}^g$	**0.3892**	**0.1344**	**0.1207**	0.0333	0.0134
$v_{\text{PCC},q}^g$	0.0943	**0.3279**	**0.1049**	0.0195	0.0029
θ	0.0118	0.0100	**0.1061**	**0.5326**	**0.3930**
$\Delta\omega$	0.0001	0.0003	0.0066	**0.1787**	**0.1694**
VFF	**0.1646**	**0.1192**	**0.4271**	**0.1413**	0.0526
V_{dc} PI	0.0000	0.0046	0.0093	**0.4236**	**0.1708**
V_{PCC} PI	0.0018	0.0152	**0.1170**	**0.4449**	**0.4296**
q-axis current PI	0.0012	0.0015	0.0182	0.0205	0.0159
d-axis current PI	0.0000	0.0003	0.0016	**0.4607**	0.0710
I_{pv}	0.0001	0.0013	0.0101	0.0420	0.0063

The two high-frequency ($>$ 100 Hz) modes $\lambda_{1,2}$, $\lambda_{3,4}$ are mainly due to grid LC dynamics. Note that VFF influences these two modes. The 58.5 Hz mode $\lambda_{5,6}$ is mainly related to grid dynamics and VFF. The two low-frequency modes $\lambda_{7,8}$ at 7.5 Hz $\lambda_{9,10}$ at 7.8 Hz are influenced by the outer controls and PLL.

Table 2.6: Constant dc voltage model's eigenvalues and influencing factors

Modes	**Eigenvalue**	**Freq. (Hz)**	**Most relevant factors**
$\lambda_{1,2}$	$-830.2 \pm j2207.4$	351.3	LC dynamics
$\lambda_{3,4}$	$-98.5 \pm j841.0$	133.8	LC dynamics
$\lambda_{5,6}$	$-87.0 \pm j368.1$	58.5	VFF and grid dynamics
$\lambda_{7,8}$	$-73.9 \pm j47.70$	7.5	Outer control and PLL
$\lambda_{9,10}$	$-0.8 \pm j49.2$	7.8	Outer control and PLL

The participation factor analysis of the dominant oscillation mode at 7.8 Hz indicates that this mode is influenced by the PLL and the VSC outer controls. In addition, this mode moves to the RHP when the grid becomes weaker. The characteristics of the low-frequency oscillation mode identified using the simplified model indeed matches the existing knowledge on low-frequency oscillations due to VSC in weak grids. To this end, the proposed 15th-order model fulfills the goal of providing both time-domain simulation and small-signal stability analysis for low-frequency oscillations due to weak grid interconnection.

2.4 Sensitivity Analysis and Validation

In this section, the stability sensitivity regarding controller parameters are investigated based on the constant power control assumption, shown in Fig, 2.13. We will first analyze the impact of V_q feedforward with first-order filter (VFF) on both unity power factor (UPF) control and V_{ac} voltage control. The root locus, participation factor (PF), and eigenvalue are conducted. Additionally, the analysis on PLL, V_{ac} gain and DC-link capacitor size will be investigated. Finally, we will validate the analysis through PV Simpower testbed.

2.4.1 Impact of VFF

Fig. 2.14 gives the V_q feedforward open-loop diagrams, which are applied for UPF control and V_{ac} control. Figure (a) is for V_q feedfoward open-loop without the filter, while the figure (b) is for V_q feedfoward open-loop with the filter.

Root locus analysis can be used for examining how modes of the system change with variation of open-loop gain. Based on the diagram in Fig. 2.14, we can use MATLAB `rlocus` command to

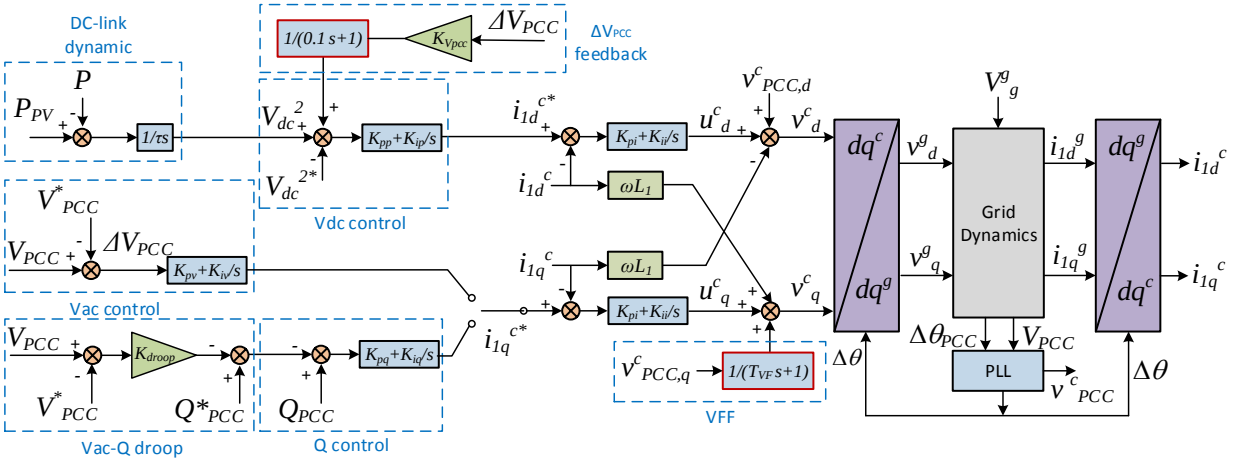

Figure 2.13: Block diagram of the dynamic system model

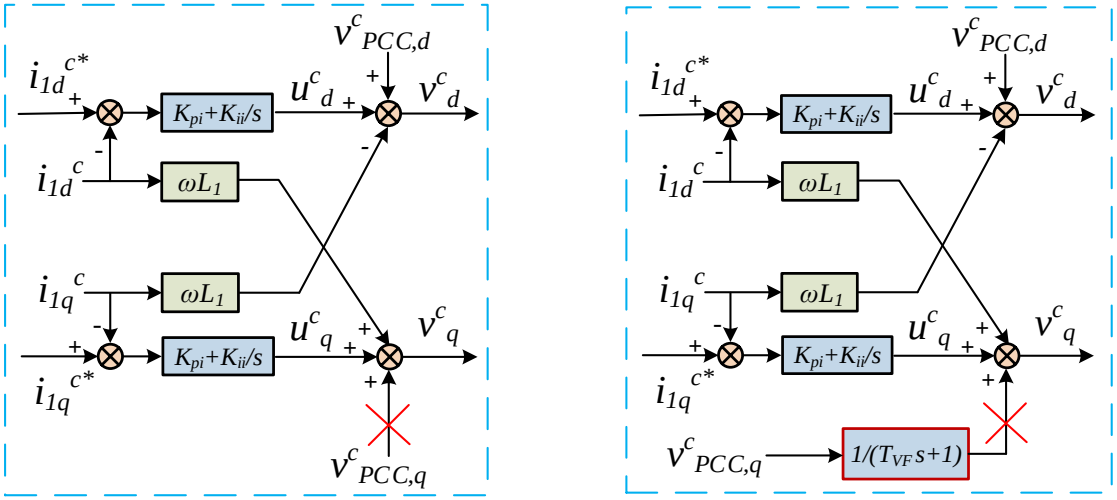

(a) (b)

Figure 2.14: V_q feedforward open-loop diagrams without/with filter

carry out the root locus plot in Fig. 2.15. We assume X_g is 0.72 pu. Note that the imaginary is in rad/second and divide it by 2π to get the frequency in Hz. The gain direction is from "×" to "o". The gain equals zero represents the mode positions without V_q feedforward, and the gain equals one represents the mode positions with V_q feedforward.

The V_q feedforward open-loop root locus of UPF control is resented in Fig. 2.15 (a)(b). Subplot (a) indicates adding V_q feedforward without filter will lead the high-frequency mode λ_3 to left. And subplot (b) shows that adding V_q feedforward with filter (VFF) still lead the λ_3 to left-half plane

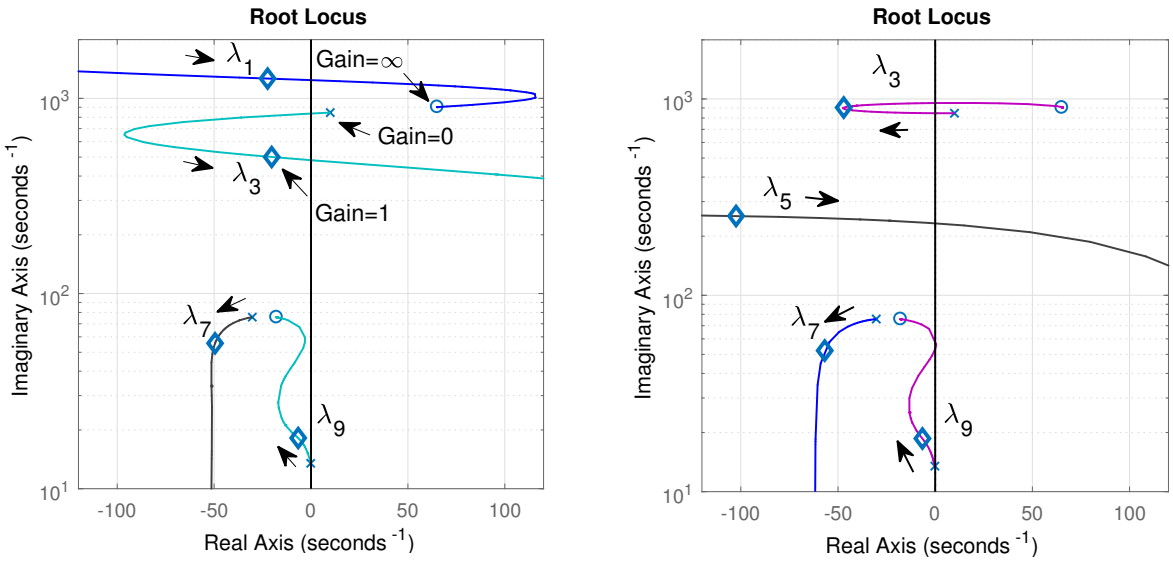

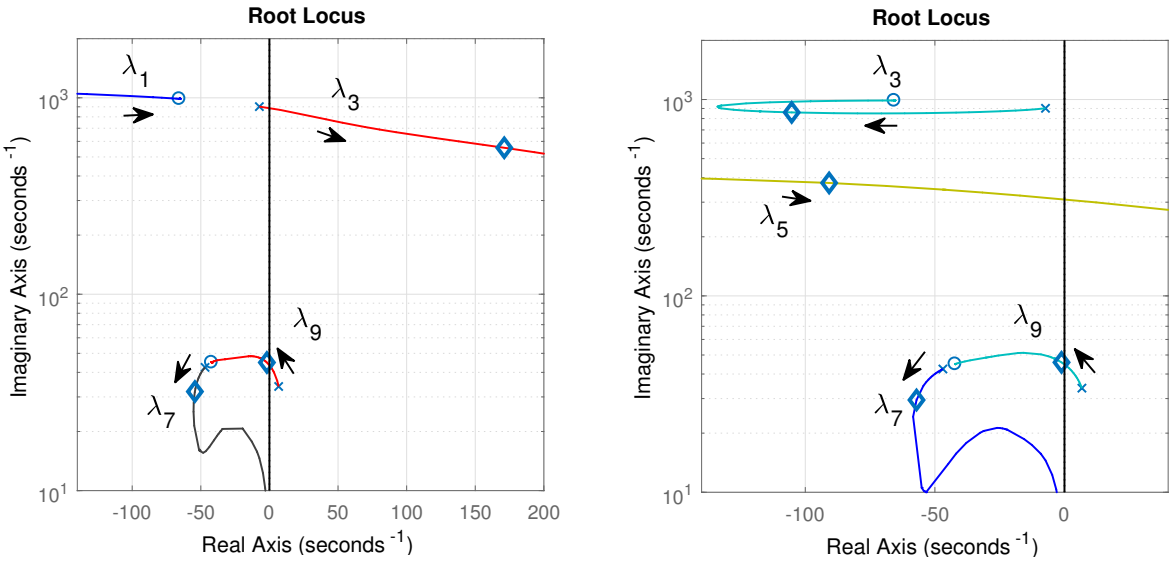

Figure 2.15: Root locus of V_q feedforward open-loop

(LHP) from right-half plane (RHP). Both (a) and (b) shows the low-frequency modes $\lambda_{7,9}$ move to left when $X_g = 0.72$ pu.

The V_q feedforward open-loop root locus of V_{ac} control is presented in Fig. 2.15 (c)(d). Subplots (c) is the scenario without filter, which is based on Fig. 2.14 (b). We can observe that the high-frequency mode λ_3 moves toward RHP if the V_q feedforward is added. On the other hand, adding

V_q feedforward with filter can lead the high-frequency mode λ_3 to left in subplot (d). And low-frequency modes $\lambda_{7,9}$ moves left when $X_g = 0.92$ pu.

UPF and V_{ac} control root locus analysis indicate VFF will lead the high-frequency mode λ_3 and low-frequency modes $\lambda_{7,9}$ to left, which improves the system stability. Also, VFF will introduce a high-frequency mode λ_5.

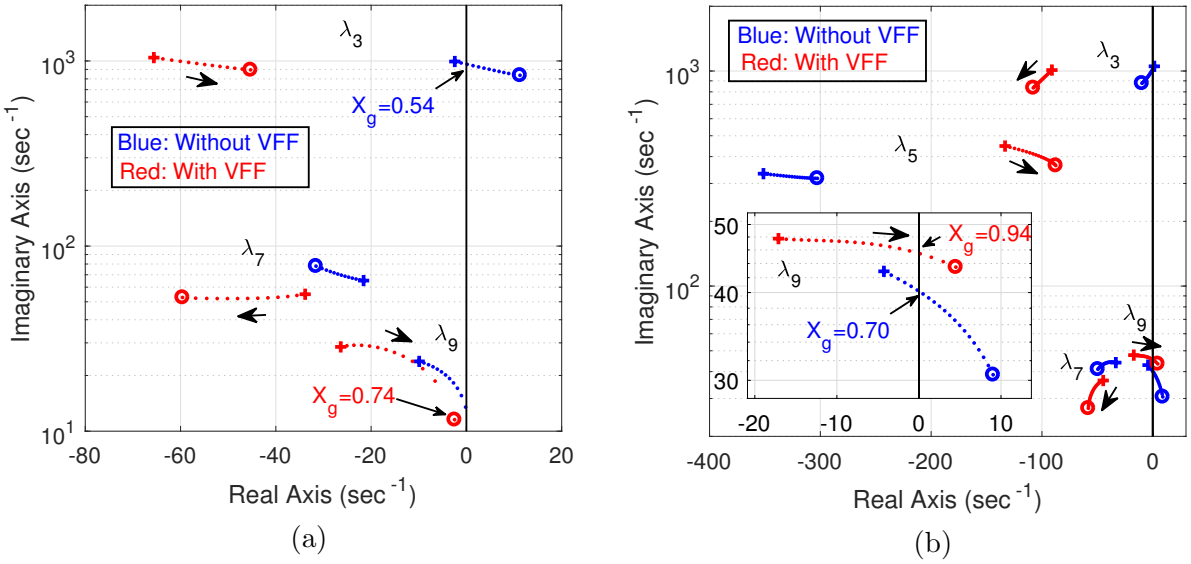

Figure 2.16: Eigenvalue loci of UPF control and V_{ac} control with varying X_g

To validate the conclusion from root locus analysis, the eigenvalue loci for UPF control and V_{ac} control are plotted in Fig. 2.16. First, we can see that V_{ac} voltage control is better than UPF control on marginal condition. Second, adding VFF improves system stability condition. In subplots (a), we notice that the oscillation can only appear when there is no VFF under UPF control. Once VFF is added, the stability marginal X_g is improved. Eigenvalue loci will not go across imaginary axis since $X_g = 0.74$ pu is the steady-state limit, seen Table 2.2. On the other hand, oscillation can happen under V_{ac} control. Since $X_g = 0.94$ pu is still under the steady-state limit.

The participation factors (PFs) against dominated low-frequency mode λ_9 are listed in Table 2.7. Four scenarios are investigated here. PFs are generated in the marginal condition. It can be

Table 2.7: PFs of dominated mode λ_9

Description	State Variable	UPF Control		V_{ac} control	
		Without VFF	With VFF	Without VFF	VFF
DC-link Dynamic	V_{dc}^2	0.0699	0.0788	0.2010	0.2475
Grid Dynamic	$i_{1,d}^g$	0.0026	0.0029	0.0008	0.0215
	$i_{1,q}^g$	0.0436	0.0485	0.0060	0.0504
	$i_{g,d}^g$	0.0148	0.0160	0.0072	0.0594
	$i_{g,q}^g$	0.0168	0.0181	0.0354	0.1124
	$v_{PCC,d}^g$	0.0018	0.0020	0.0055	0.0278
	$v_{PCC,q}^g$	0.0020	0.0023	0.0025	0.0153
PLL Dynamic	θ	**0.4266**	**0.4465**	**0.3016**	**0.9678**
	$\Delta\omega$	**0.4193**	**0.4359**	0.1513	0.5456
Outer-loop PI	i_{1d}	0.0713	0.0804	0.1868	0.4665
	i_{1q}	-	-	**0.2897**	**0.7414**
Inner-loop PI	u_d	0.0007	0.0008	0.0647	0.0168
	u_q	0.0348	0.0077	0.0697	0.0598
VFF	$V_{PCC,q}^c$	-	0.0357	-	0.0745

noticed that the PLL dynamic has the greatest impact on the dominant eigenvalue. After adding V_{ac} outer loop control, both PLL and V_{ac} control have the most impact on dominant mode.

2.4.2 Impact of PLL

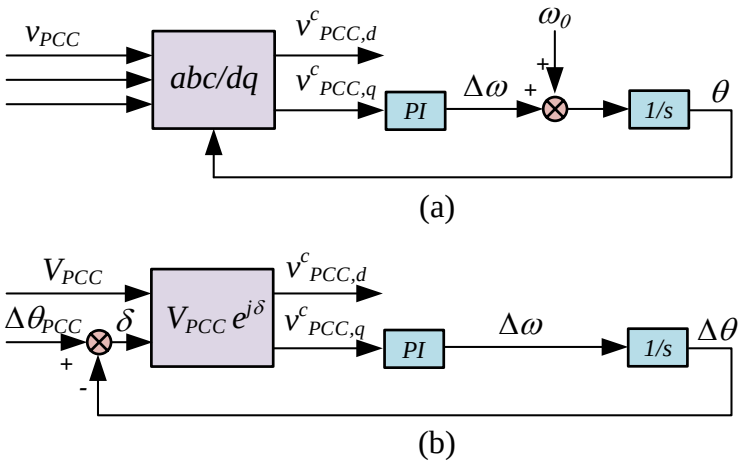

Figure 2.17: Block diagrams of a PLL

We already know PLL dynamic has a great effect on dominated mode $\lambda_{9,10}$. This part is to investigate PLL's effect on system stability through Bode plots and reactance and resistance (XR) crossover criteria based on impedance model.

Adding VFF gives PLL a better capability to synchronize converter's voltage with PCC's voltage in q-axis. A general second-order PLL, which is detailed in Chapter 6 [51], is adopted here. Fig. 2.17 gives the control blocks. (a) indicates the original PLL control block in Simpower testbed. And (b) represents the PLL in analytical model dq-frame. We can see θ is integrated from $\Delta\omega$ and $\Delta\omega$ is generated from $v^c_{PCC,q}$ through proportional integral (PI) controller. Although V_q feedforward ($V^c_{PCC,q}$) is zero in steady state. We notice that $V^c_{PCC,q}$ has a great effect on the low-frequency modes since $V^c_{PCC,q}$ is directly computed from PLL.

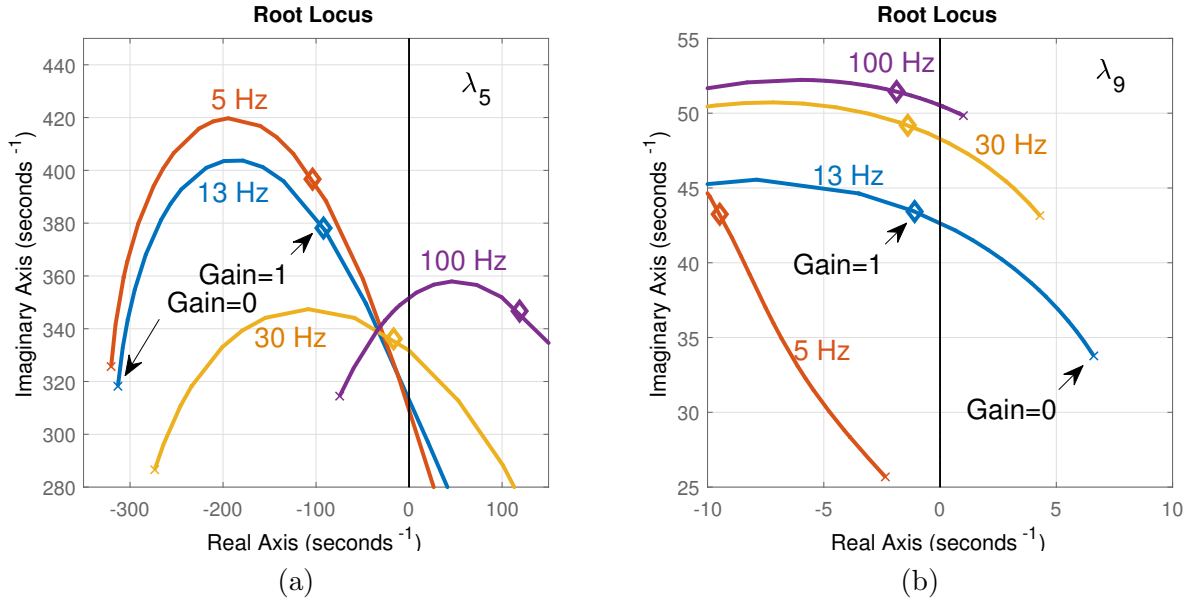

Figure 2.18: Root locus of VFF open-loop under V_{ac} control with varying PLL bandwidth where $X_g = 0.9$ pu

Table 2.8: PLL parameters and corresponding bandwidth

$K_{\text{p,PLL}}$, $K_{\text{i,PLL}}$ (pu)	[28, 100]	[60, 1400]	[180, 1400]	[600, 1400]
Bandwidth (Hz)	5	13	30	100

The VFF open-loop root locus under V_{ac} control is firstly given in Fig. 2.18. Four PLLs are tested. Their corresponding parameters and bandwidth are listed in TABLE 2.8. We treat 13 HZ PLL as the benchmark and compare it with lower and higher bandwidth PLLs. In Fig. 2.18 (a) we

can see the PLL with higher bandwidth leads SSR mode to RHP. In Fig. 2.18 (b), 13 Hz PLL is the worst scenario. Increasing PLL bandwidth can mitigate the effect of VFF and moves low-frequency mode λ_9 away from imaginary axis. But the very slow PLL, i.e. with 5 Hz bandwidth, can pull the λ_9 to left dramatically. In another word, increasing PLL bandwidth can worsen mode $\lambda_{5,6}$ but improve mode $\lambda_{9,10}$. And the stability can be improved by tuning PLL to very small bandwidth.

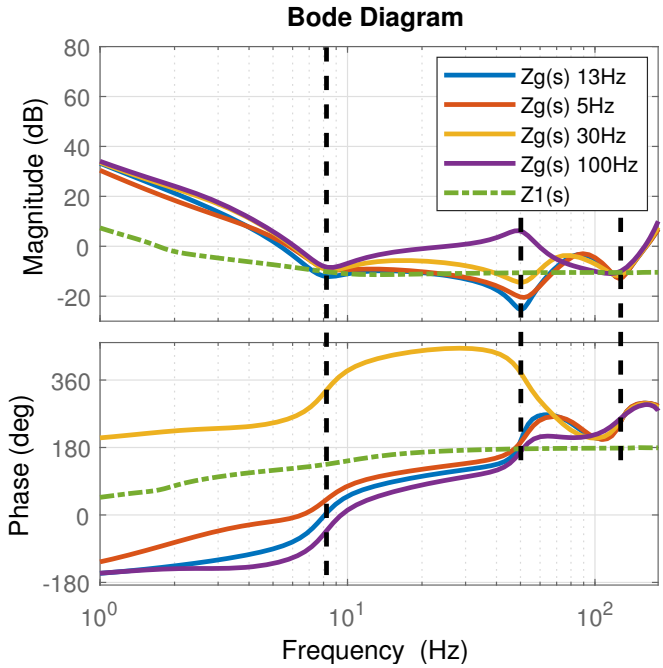

Figure 2.19: Bode plots of $Z_g(s)$ and $Z_1(s)$ with varying PLL bandwidth

Table 2.9: SSR stability criteria

X zero crossover	$R > 0$	$R < 0$
X slope > 0	Stable	Unstable
X slope < 0	Unstable	Stable

Open-loop analysis is used to generate the s-domain transfer functions of grid side impedance $Z_g(s)$ and converter side impedance $Z_1(s)$ in q-axis. $Z_g(s)$ can be carried out by open-loop linear analysis between v_q^c and i_{1q}^c in Fig. 2.13. Similarly, we can get $Z_1(s)$ from i_{1q}^c to v_q^c. Varying PLL affect directly on grid side impedance. The bode plots are presented in Fig. 2.19. There are three dips where $Z_g(s)$ magnitude crossing $Z_1(s)$ magnitude. They can be used to judge the potential

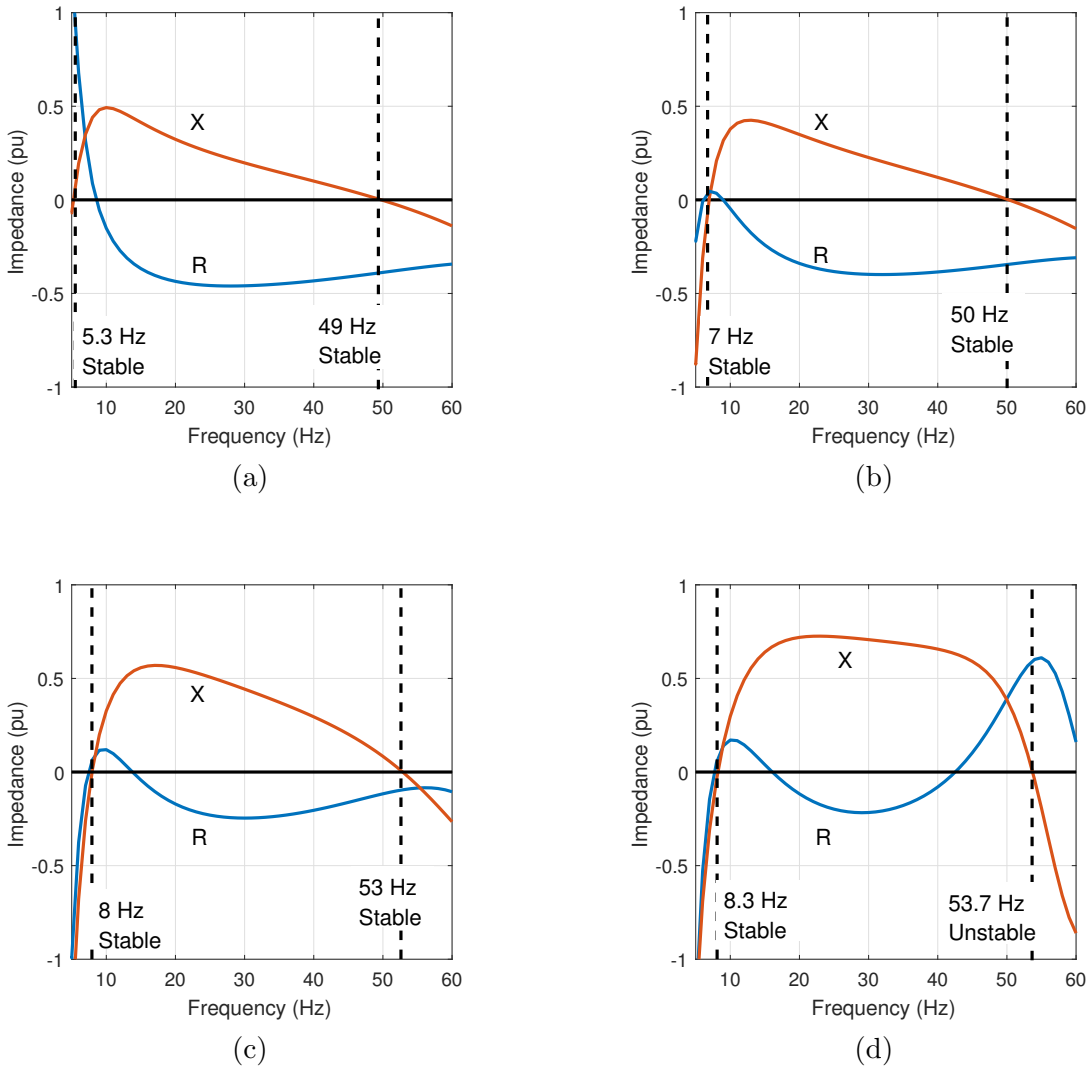

Figure 2.20: q-axis total impedance XR zero crossover check

oscillation modes. And the system is unstable if the corresponding phase difference is smaller than -180 degree. We can use the dips where frequency is 8 Hz to verify stability. Only the scenario with 100 Hz PLL is unstable. That matches with our root locus analysis in Fig. 2.18.

Furthermore, reactance zero crossover criteria [52] can be used to judge the subsynchronous resonant (SSR) based on impedance model. The effect of PLL bandwidth on total q-axis impedance can be observed. The total q-axis impedance can be computed from the sum of $Z_g(s)$ and $Z_1(s)$. Then we can plot the subsynchronous frequency response of resistance (R) and reactance (X),

which are plotted in Fig.2.20. (a)(b)(c)(d) are representing 5-Hz PLL, 13-Hz PLL, 30-Hz PLL, and 100-Hz PLL, respectively. The XR zero crossover criteria is listed in TABLE 2.9. We can see high frequency bandwidth PLL results a 53.7 Hz SSR to cause system unstable. Therefore, q-axis total impedance frequency response stability analysis matches with previous two approaches. In a word, tuning PLL bandwidth can improve system stability. But too fast PLL will cause a SSR in the system.

2.4.3 Impact of V_{ac} Gain

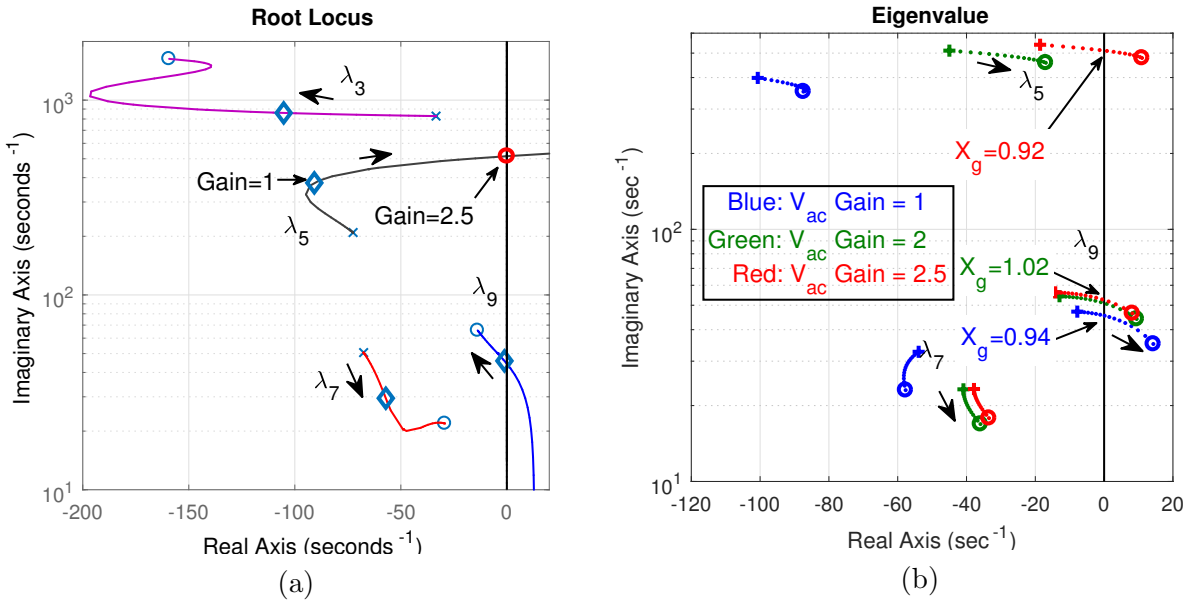

Figure 2.21: Root locus and Eigenvalue analysis of V_{ac} gain

Based on previous discussion, we already know the V_{ac} control performs better with VFF under our parameters setting. Now the effect of V_{ac} control gain will be analyzed with adding VFF. The time constant T_{VF} is assumed to be $1e^{-3}$. First, the root locus against V_{ac} gain open-loop is carried out in Fig. 2.21. The V_{ac} control PI controller parameters are $K_{pv} = 1$, $K_{iv} = 100$ when the gain is 1. Subplot (a) shows larger gain will lead high-frequency mode λ_3 to left when $X_g = 0.92$ pu.. While λ_5 moves to left first, then to right if gain is greater than 1. λ_5 will move to RHP when gain

is larger than 2.5. The low-frequency mode λ_9 moves to left with V_{ac} gain increasing. Thus, larger voltage gain is better. But it will lead λ_5 to RHP if the gain is too large.

Fig. 2.21 (b) gives eigenvalue loci under different voltage control gains. For each scenario, X_g increases from 0.8 to 1.1 pu. High-frequency modes is not shown due to little changing. Different V_{ac} gains can result different marginal X_g. When gain is 1, the marginal X_g is smaller than the one when gain is 2. Also it can be seen λ_5 is closer to imaginary-axis with increasing V_{ac} gain. What we observed from eigenvalue loci matches with the root locus analysis in Fig. 2.21 (a).

2.4.4 Impact of DC-link Capacitor

In this part, the analysis of DC-link capacitor (C_{dc}) will be conducted. Both UPF control and V_{ac} control will be analyzed and compared together.

The DC-link dynamic is analyzed to build the relationship between V_{dc} and active power on DC side. It can be described by the following equation:

$$\frac{C_{dc}}{2}\frac{dV_{dc}^2}{dt} = P_{PV} - P \tag{2.7}$$

where P_{PV} is the active power generated by PV farm and P is the active power transfered from converter to grid. We can rewrite it in per unit format in (2.8).

$$\underbrace{\frac{C_{dc}V_{dc,base}^2}{2P_{base}}}_{\tau}\frac{d(V_{dc}^{pu})^2}{dt} = P_{PV}^{pu} - P^{pu} \tag{2.8}$$

The superscript "pu" indicate per unit values. $V_{dc,base}$ and P_{base} denote the base voltage on DC bus and base active power on PCC bus, respectively.

$$\frac{d(V_{dc}^{pu})^2}{dt} = \underbrace{\frac{1}{C_{dc}}}_{\text{Gain}}\frac{2P_{base}(P_{PV}^{pu} - P^{pu})}{V_{dc,base}^2} \tag{2.9}$$

Rewrite the equation (2.8) in (2.9). The DC-link open-loop analytical model can be carried out using $\frac{1}{C_{dc}}$ as the gain. The root locus for UPF control and V_{ac} control are given in Fig. 2.22.

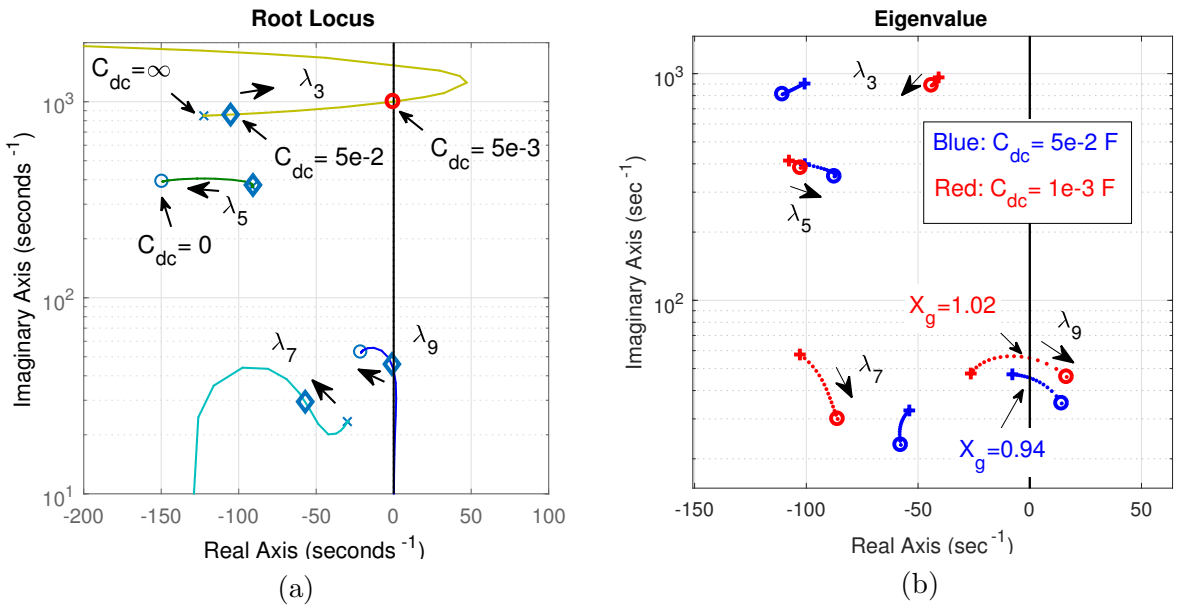

Figure 2.22: Root locus and Eigenvalue analysis of C_{dc}

In Fig. 2.22 (a) and (b) present root locus and eigenvalue analysis on different C_{dc}. (a) is the root locus of $1/C_{dc}$ open-loop when $X_g = 0.92$ pu. Only the modes λ_3 and λ_9 will cause stability issues. For λ_9, we notice the smaller C_{dc} the better. Too small C_{dc} will cause λ_3 to RHP. The eigenvalue loci of different DC-link capacitors is given in Fig. 2.22 (b). We can see the smaller DC capacitor size results a higher marginal X_g. Hence, a relatively smaller DC-link capacitor size is preferred.

2.4.5 Adding ΔV_{PCC} Feedback

In [31], a stability control is introduced to enhance the stability for wind in weak grid. One of the stability control strategy, ΔV_{PCC} feedback, is examined in our PV weak grid system under V_{ac} control. The ΔV_{PCC} feedback is to modulate the power order using the PCC voltage difference (ΔV_{PCC}), which is shown in Fig. 2.14.

The ΔV_{PCC} feedback open-loop root locus when $X_g = 0.9$ pu is given in Fig. 2.23 (a). It can be seen that adding ΔV_{PCC} feedback with a proper gain leads modes $\lambda_{3,5,9}$ to left. But it results

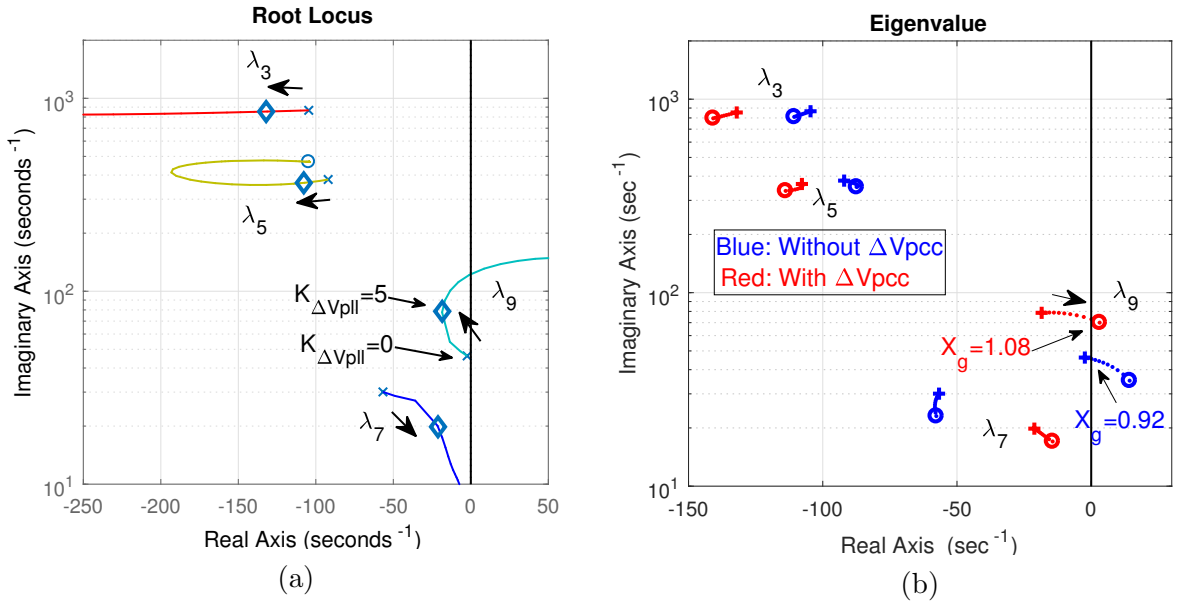

Figure 2.23: Root locus and Eigenvalue analysis of ΔV_{PCC}

low-frequency mode λ_7 closer to imaginary axis. The eigenvalue loci comparison is conducted in Fig. 2.23 (b). It shows adding ΔV_{PCC} feedback with $K_{Vpcc} = 5$ can improve the system mariginal condition from $X_g = 0.92$ pu to $X_g = 1.08$ pu.

2.4.6 Volt/var Droop

In Fig. 2.13, reactive power (Q) control is an alternative outer control strategy to generate i_{1a}^{c*} for inner loop. The Q control system has a same marginal condition to UPF control if $Q*$ is set as zero. Note that the outer PI controller is set as $K_{pq} = 1, K_{iq} = 100$. The volt/var droop control is to add a proportional ΔV_{PCC} error to modulate the active power control reference. The control principle can be explained by the equation (2.10). Thus, the reactive power set-point will be decreased if too high V_{PCC} causes stability issues.

$$Q = Q^* - K_{droop}(V_{PCC} - V_{PCC}^*) \tag{2.10}$$

The root-locus of volt/var droop gain open-loop when $X_g = 0.74$ pu is plotted in Fig. 2.24 (a). Comparing with only Q control, droop control can lead the dominated mode λ_9 to left to increase the system stability. However, mode λ_5 will cause stability issue if the droop gain K_{droop} is larger than 1.6. The corresponding eigenvalue analysis is given in Fig. 2.24 (b). It is obvious add a volt/var droop with $K_{droop} = 1$ can increase the system marginal condition from $X_g = 0.74$ pu to $X_g = 0.82$ pu.

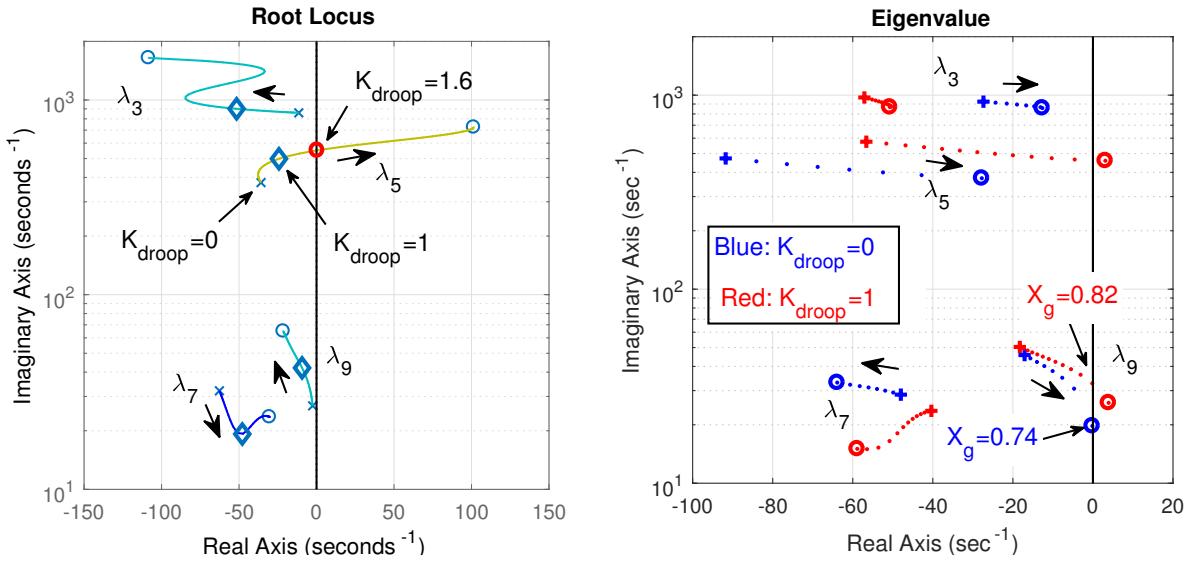

Figure 2.24: Root locus and Eigenvalue analysis of droop gain

2.4.7 Testbed Validation

Then we use MATLAB/Simpower PV testbed to validate the above analysis. We will apply a small voltage signal change in the system under different conditions to see their dynamic responses.

First, the impact of VFF is tested. Both UPF control and one V_{ac} control are presented in Fig. 2.25. Subplot (a) is UPF control where X_g steps from 0.52 to 0.58 pu. And subplot (b) is V_{ac} control where X_g steps from 0.7 to 0.74 pu. For each control strategy, a transmission line tripping

is simulated to increase X_g. We can see VFF's effect on improving system stability under weak grid condition. Those simulation results matches with eigenvalue analysis in Fig. 2.16.

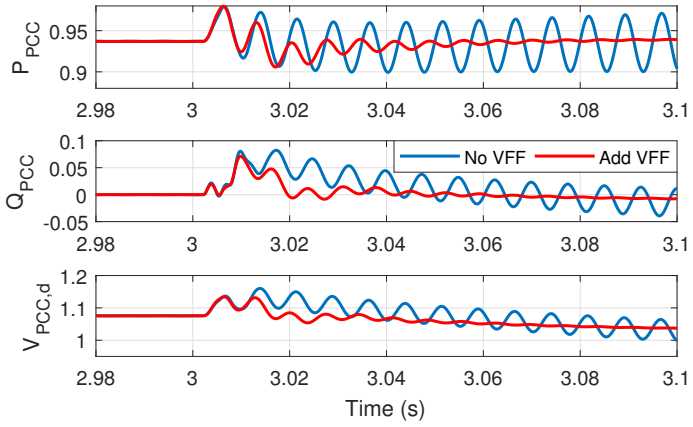

(a)

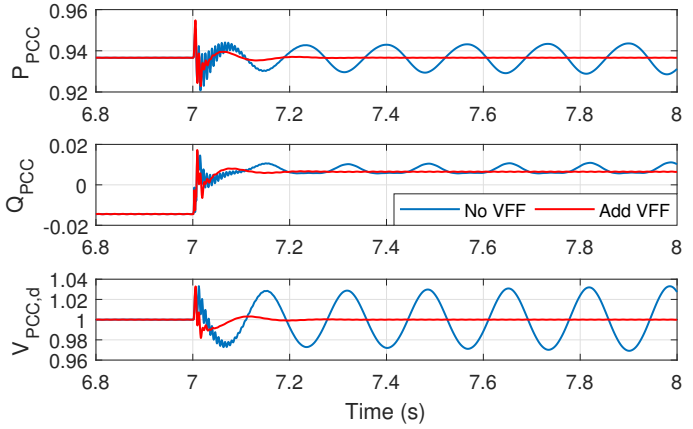

(b)

Figure 2.25: EMT validation for VFF

Second, the impact of PLL is tested. In Fig. 2.26, we validated PLL's impact on stability under weak grid condition. Subplot (a) is to compare 13Hz PLL and 5Hz PLL when $X_g = 0.92$ pu. Subplot (b) is to compare 30Hz PLL and 40Hz PLL when $X_g = 0.80$ pu. A 0.02 pu small disturbance is applied on V^*_{PCC} to exam the system stability. We first compared 13 Hz PLL to 5 Hz PLL. It can be seen that well tuned PLL can improve system stability. Additionally, a 55 Hz SSR will occur if keep increasing PLL bandwidth to 40 Hz, i.e., $K_{p,PLL} = 240$, $K_{i,PLL} = 1400$. It matches with our analysis on PLL.

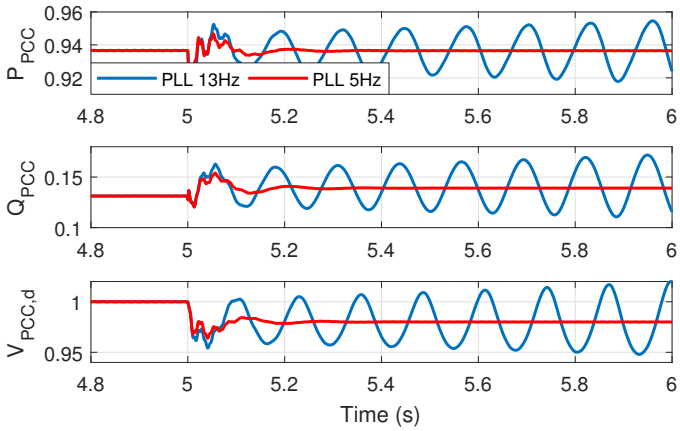

(a)

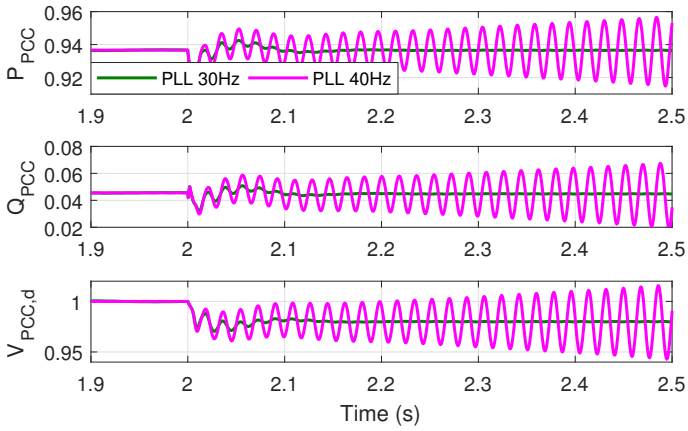

(b)

Figure 2.26: EMT validation for different PLLs

Third, the impact of V_{ac} gain is tested. In Fig. 2.27, V_{ac} gain's effect is tested in EMT testbed. Subplot (a) gives dynamic responses of decreasing V^*_{PCC} order, which shows increasing V_{ac} PI controller parameters from [1, 100] to [2, 200] improves system stability when $X_g = 0.92$ pu. And (b) is to prove the grid strength is increased to $X_g = 1.0$ pu. (C) is to validate that system will have 80 Hz stability issue if the V_{ac} gain is increased to 2.4 when X_g steps from 0.92 to 0.94 pu. This observation matches with Fig. 2.21 (b) marginal conditions.

Fourth, the impact of C_{dc} is tested. In Fig. 2.28, DC-link capacitor's effect is examined in our EMT testbed. (a) is to validate decreasing C_{dc} from $5e^{-2}$ F to $1e^{-2}$ F improves system stability when $X_g = 0.92$ pu. In (b), mode λ_9 caused 8 Hz undamped oscillation and the mode λ_3 caused

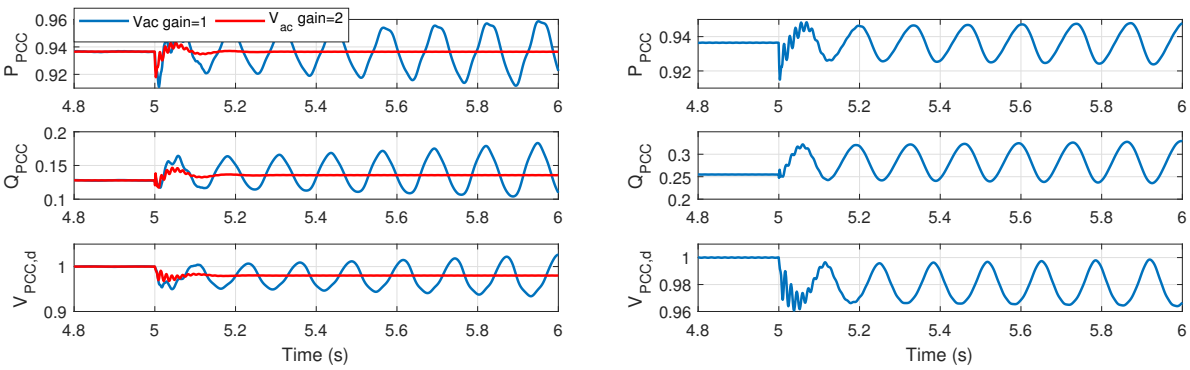

(a) (b)

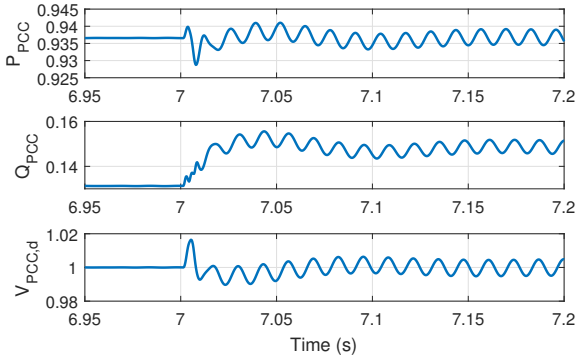

(c)

Figure 2.27: EMT validation for different V_{ac} gains

high-frequency damped oscillation can be seen when approaching $X_g = 1.0$ pu. This observation matches to eigenvalue loci analysis in Fig. 2.22 (b).

Fifth, the impact of ΔV_{PCC} feedback is tested. The EMT testbed validation is conducted in Fig. 2.29. In (a), we can see the ΔV_{PCC} feedback with $K_{Vpcc} = 5$ can make the system still stable comparing to without ΔV_{PCC} feedback condition when $X_g = 0.92$ pu. In (b) case study, it has been proved ΔV_{PCC} feedback with $K_{Vpcc} = 5$ increased the system marginal condition to $X_g = 1.06$ pu. It matches with above root locus and eigenvalue analysis in Fig. 2.23.

Sixty, the impact of volt/var droop is tested. The volt/var droop's effect is validated in our PV EMT testbed. And the performances are shown in Fig. 2.30. In Fig. 2.30 (a) X_g steps from 0.7 to 0.74 pu. It indicates the system will be over the limitation when $X_g = 0.74$ pu without droop control. And Fig. 2.30 (b) X_g steps from 0.8 to 0.82 pu. It can prove our analysis that

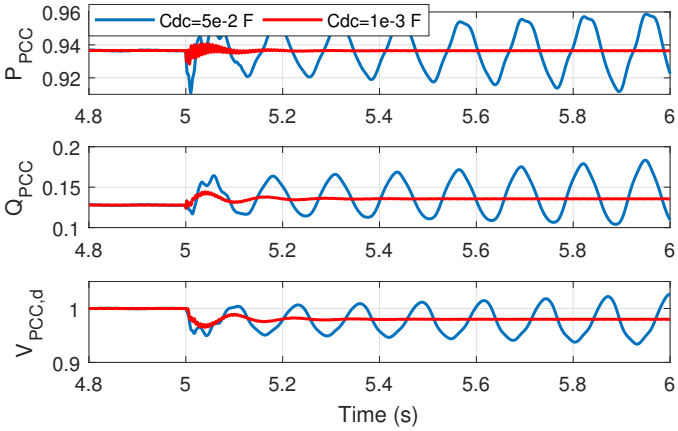

(a)

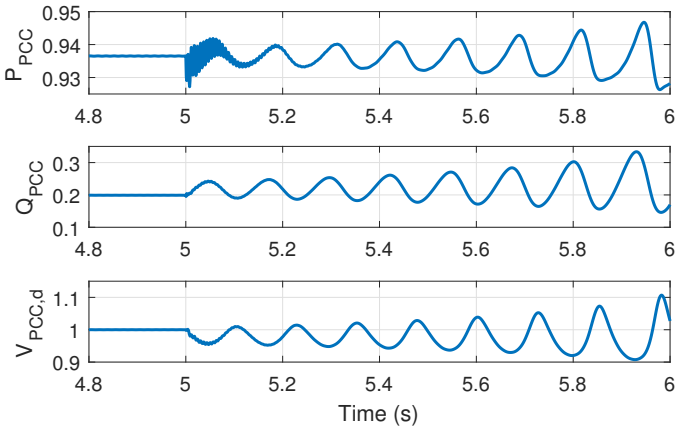

(b)

Figure 2.28: EMT validation for different DC-link capacitors

system stability can be improved and a 4.5 Hz oscillation will be observed once $X_g = 0.82$ pu. Additionally, there is a 60-70 Hz high-frequency oscillation damped oscillation which attributes to λ_5. It matches to root locus and eigenvalue analysis in Fig. 2.24.

2.5 Conclusion

In this chapter, two state-space models are proposed to represent a grid-connected PV system for low-frequency oscillation analysis. The two models simplify the dc side of the PV system with two different assumptions: constant input power and constant dc voltage. Those two models are

compared with an EMT testbed with full details on time-domain simulation results, frequency-domain responses of admittance models, and eigenvalue analysis results. The comparison indicates that the constant voltage model can accurately capture the low-frequency oscillation dynamics at weak grid conditions. Influencing factors of low-frequency oscillations are identified as grid strength, PLL, and inverter's outer controls. Additionally, the stability sensitivity of control parameters are examined. The Vq feedforward with first-order filter on unit power control and V_{ac} control are identified. Also, the impact of PLL, V_{ac} outer loop controller, DC-link capacitor size, stability control, and volt/var droop control are analyzed and validated, respectively.

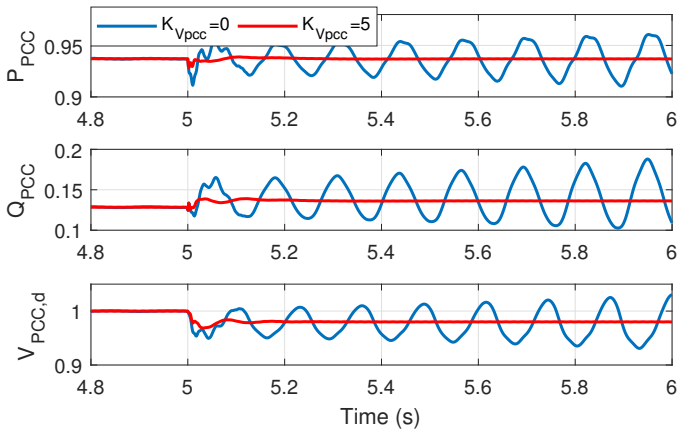

(a)

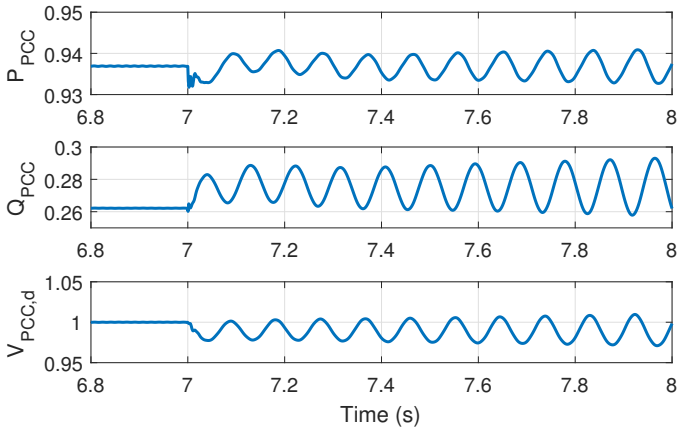

(b)

Figure 2.29: EMT validation for with/without ΔV_{PCC} control

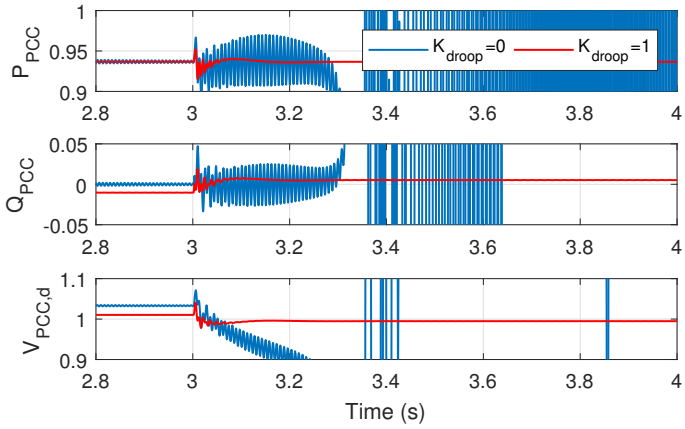

(a)

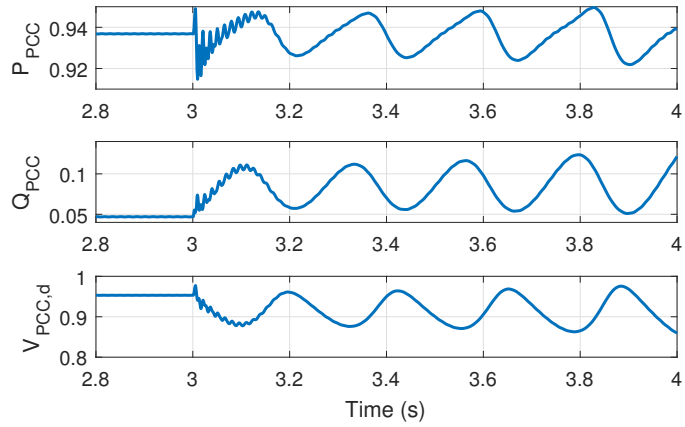

(b)

Figure 2.30: EMT validation for introducing volt/var droop control

Chapter 3: Scalable IBR Integrated Network Modeling

In this chapter, two approaches to conduct scalable IBR (inverter-based resources) integrated network dynamic modeling are proposed. The first one is nonlinear state-space modeling method. This is an extended work from IBR simplified modeling in the previous chapter. And the another one is s-domain linear admittance modeling method, which will be implemented for integrating with measured admittance IBR in the next chapter. A 9-bus system is adopted as an example to demonstrate the detailed process of two approaches. Finally, the eigenvalue analysis is carried out via those two methods.

3.1 9-bus System Example

This demonstration is based on 100 MVA IEEE 9-bus system, known as the Western System Coordinated Council (WSCC) 9-bus system. The system topology is shown in Fig. 3.1. The network parameters are from MATPOWER toolbox [53] and power flow is computed via `runpf` command. The IBR block is used to replace the synchronous generators on bus 2 and 3. Table 4.1 gives the branch data in per unit. The loads and generations are modified to satisfy the IBR's operation condition. They are listed in Table 4.2.

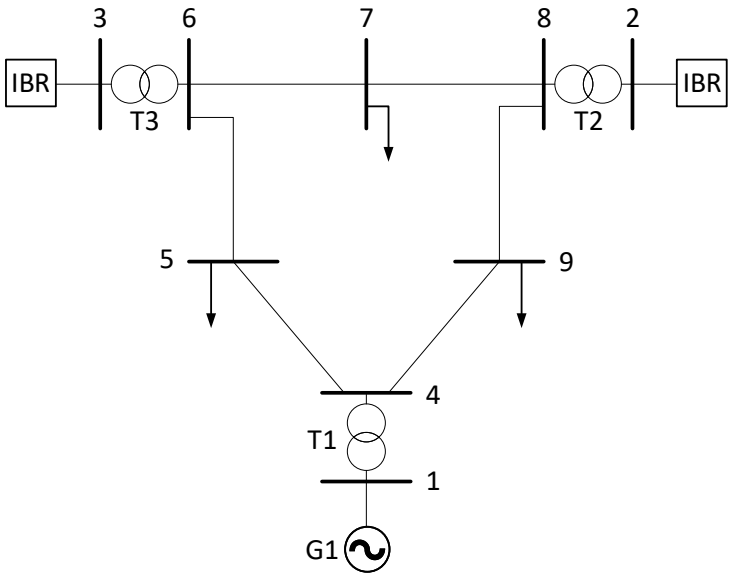

Figure 3.1: IBR integrated 9 bus network system

Table 3.1: 9 bus branch data

From	To	R (p.u.)	X (p.u.)	B (p.u.)
1	4	0	0.0576	0
4	5	0.017	0.092	0.158
5	6	0.039	0.17	0.358
3	6	0	0.0586	0
6	7	0.0119	0.1008	0.209
7	8	0.0085	0.072	0.14
8	2	0	0.0625	0
8	9	0.032	0.161	0.306
9	4	0.01	0.085	0.176

Table 3.2: 9 bus generators and loads data

Gen Bus	Bus type	P_g (p.u.)	V (p.u.)
1	Swing	0.71	1.0
2	PV	1.63	1.025
3	PV	0.85	1.025

Load Bus	$P_{d,r}$ (p.u.)	$Q_{d,l}$ (p.u.)	$Q_{d,c}$ (p.u.)
5	0.90	0.3	0
7	1.0	0.35	0
9	1.25	0.5	0

3.2 Nonlinear State-Space Modeling

The scalable nonlinear state-space model is built in MATLAB Simulink. It can be used for not only conducting the large-signal time-based dynamic simulation but also linearized small-signal analysis. Fig. 3.2 is the screenshot of the Simulink model, which applied to 9 bus system. In the following subsections, each block will be illustrated in detail.

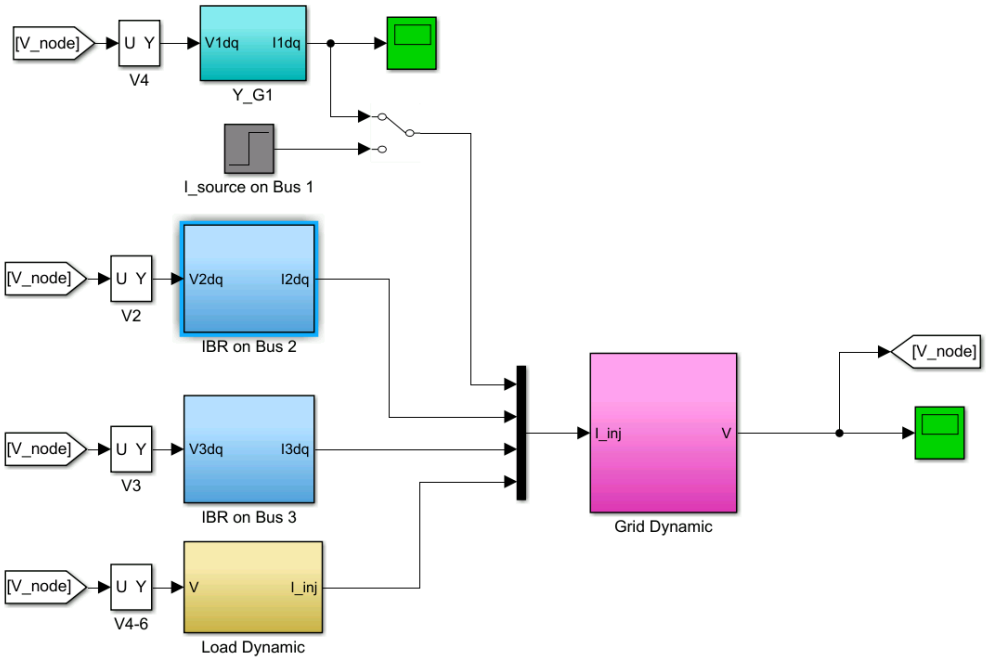

Figure 3.2: 9 bus nonlinear system in Simulink

3.2.1 Kron Reduction

The Kron reduction is required for two considerations. First, reduce the bus number for large scale network system by removing zero current injection buses. Second, some buses don't have shunt capacitor in the original grid circuit. Conducting Kron reduction can add a shunt capacitor to provide the bus voltage dynamic equations on the remaining bus.

The Kron reduction script is included, i.e., `Reduced_Y_test.m`. It is built based on Chapter 9 in Bergen's book [54]. For a $n-$bus system, if node k has zero current injection (i.e, $I_k = 0$), then we

can eliminate node k to get the reduced admittance matrix. The obtained item can be expressed by (4.3).

$$Y'_{ij} = Y_{ij} - \frac{Y_{ik}Y_{kj}}{Y_{kk}} \tag{3.1}$$

To validate the Kron reduction derived admittance matrix, the new node current injection should be identical to the original non-zero node current injection.

3.2.2 Grid Dynamic Block

Fig. 3.3 gives the inside view of grid dynamic block. The grid dynamic input and output are bus current injection and bus voltage, respectively. The derivative equations are written into the MATLAB function block.

The following illustration is given in the block script. The input signals are listed as follows:

- uv: node voltage
- ui: branch current
- ui inj: node current injection

The parameters are listed as follows:

- w0: 377rad/s
- G: conductance on each bus
- C: B/w0, susceptance on each bus
- Rij: R on branch i-j
- Lij: L on branch i-j
- Brn: number of branch
- Brc: all branch index, e.g., [i,j]

The output signals are listed as follows:

- dvdq: derivative of node voltage
- didq: derivative of branch current

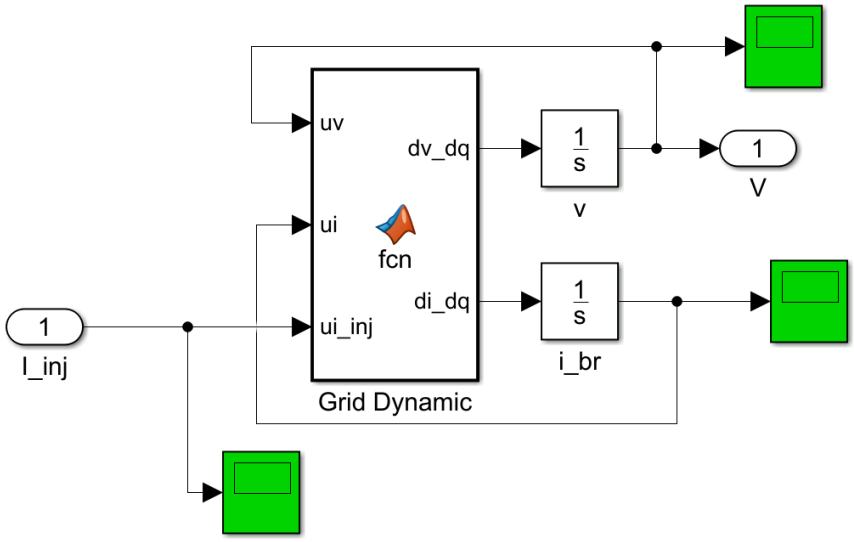

Figure 3.3: Grid dynamic block

The dq-frame bus voltage and branch current dynamic equations are given as (3.2).

$$\frac{dv_{i,d}}{dt} = \frac{1}{C_i}(i_{i,d} + \sum i_{ij,d} - G_i v_{i,d} + \omega_0 C_i v_{i,q}) \tag{3.2a}$$

$$\frac{dv_{i,q}}{dt} = \frac{1}{C_i}(i_{i,q} + \sum i_{ij,q} - G_i v_{i,q} - \omega_0 C_i v_{i,d}) \tag{3.2b}$$

$$\frac{di_{ij,d}}{dt} = \frac{1}{L_{ij}}(v_{i,d} - v_{j,d} - R_{ij} i_{ij,d} + \omega_0 L_{ij} i_{ij,q}) \tag{3.2c}$$

$$\frac{di_{ij,q}}{dt} = \frac{1}{L_{ij}}(v_{i,q} - v_{j,q} - R_{ij} i_{ij,q} - \omega_0 L_{ij} i_{ij,d}) \tag{3.2d}$$

where $v_{i,dq}$ and $i_{i,dq}$ are the bus voltage and current injection on bus i. $i_{ij,dq}$ is the current on branch $i-j$.

3.2.3 Load Dynamic Block

The load dynamic block is shown in Fig. 3.4. The input is load bus voltage and output is load current injection. Note that the positive direction is from bus to load. The parameter is load equivalent impedance $Z_{l,i}$, which equals $R_{l,i} + \omega_0 L_{l,i}$. And the derivative dynamic equation in the function box is expressed as (3.3).

$$\frac{di_{i,d}}{dt} = \frac{1}{L_{l,i}}(v_{i,d} - R_{l,i}i_{i,d} + \omega_0 L_{l,i} i_{i,q}) \tag{3.3a}$$

$$\frac{di_{i,q}}{dt} = \frac{1}{L_{l,i}}(v_{i,q} - R_{l,i}i_{i,q} - \omega_0 L_{l,i} i_{i,d}) \tag{3.3b}$$

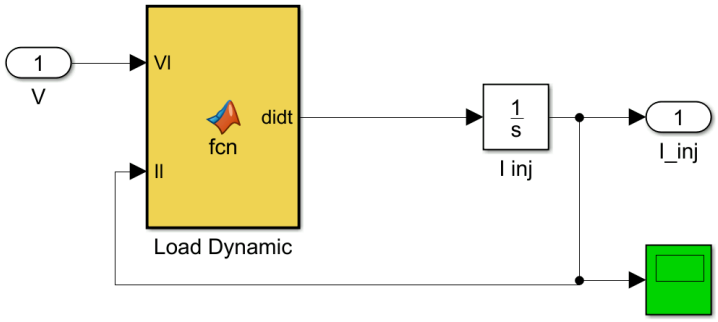

Figure 3.4: Load dynamic block

3.2.4 Synchronous Generator Block

To learn the synchronous generator admittance on bus 1, G1 is taken from 9-bus MATLAB SimPowerSystems EMT model [55]. Then maintain the steady state condition of G1 and perform frequency scan from 1 Hz to 1000 Hz with 0.01 p.u. sinusoidal perturbation. The measured admittance Bode plot is shown as the blue dotted lines in Fig. 3.5.

The cheapest way to represent the G1 synchronous generator is using a RL circuit shown in Fig. 3.6. V_s is a voltage source behind a series resistor (R_s) and inductor (L_s). And V_1 is the voltage on bus 1. Assume $R_s = 0.01\Omega$ and $L_s = 0.001H$, the RL circuit admittance is shown as the

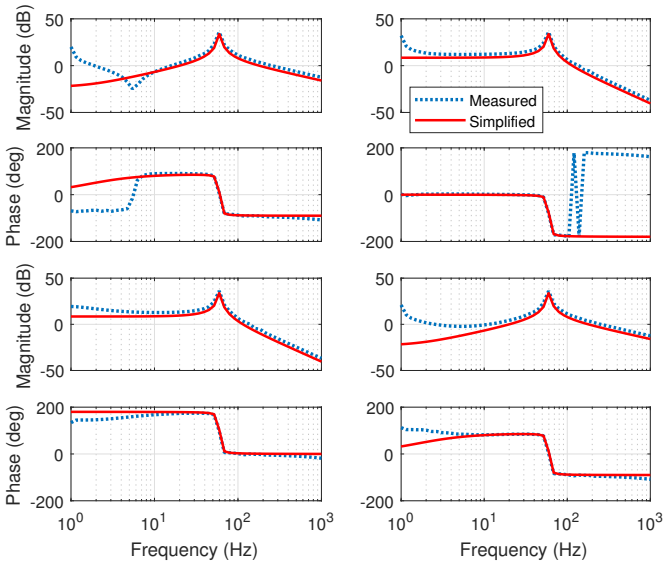

Figure 3.5: Bode plot of G1 admittance in *dq*-frame

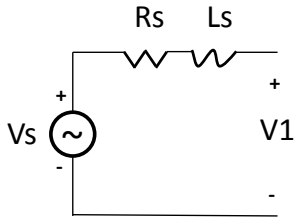

Figure 3.6: G1 simplified RL circuit

red solid lines in Bode plot Fig. 3.5. Hence, it is a acceptable assumption although the matching is not good at range of [1, 10] Hz.

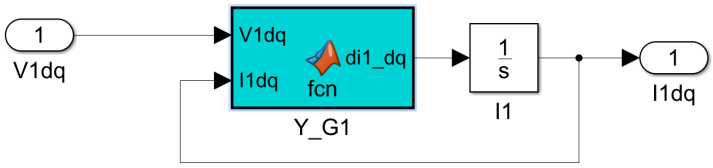

Figure 3.7: Synchronous generator G1 dynamic block

The RL circuit dynamic equation is written into function block in Fig. 3.7. With given R_s and L_s, the derivative equation is shown as (3.4).

$$\frac{di_{1,d}}{dt} = \frac{1}{L_s}(v_{1,d} - R_s i_{1,d} + \omega_0 L_s i_{1,q}) \tag{3.4a}$$

$$\frac{di_{1,q}}{dt} = \frac{1}{L_s}(v_{1,q} - R_s i_{1,d} - \omega_0 L_s i_{1,d}) \tag{3.4b}$$

3.2.5 IBR Block

Inside the IBR dynamic block, there are three components: battery block, PV block, and VSC control block. They are shown in Fig. 3.8. We can select to use battery or PV on the dc side.

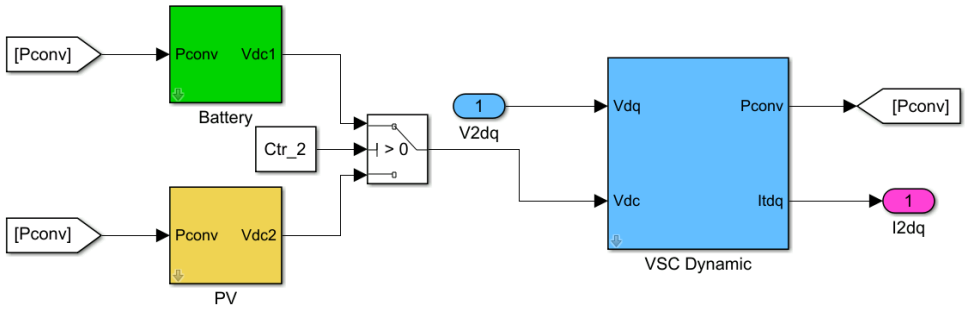

Figure 3.8: IBR dynamic block

3.2.5.1 VSC Control Dynamic

The VSC control dynamic block includes few major subsystems shown in Fig. 3.9. Double click the block, then all the parameters can be defined in the mask interface. It is presented in Fig. 3.10. Those values are defined in the initial file.

Fig. 3.11 presents the outer loop and inner loop subsystem. The outer loop consists of different control strategies. On d-axis, it can be chosen to use active power (P) control or dc voltage (V_{dc}) control. On q-axis, it can be chosen to use reactive power (Q) control or PCC voltage (V_{ac}) control. The can be selected in the mask interface. Current control is adopted in the inner loop control. A low-pass filter is added on V_q voltage feedforward to improve the control stability.

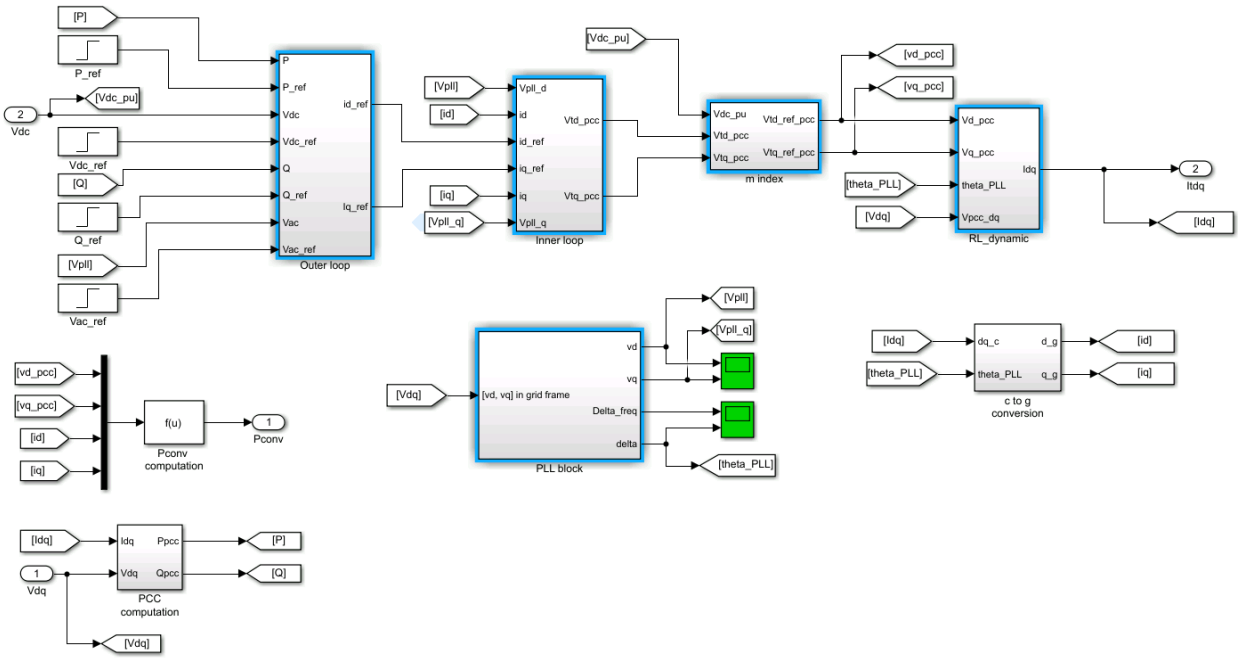

Figure 3.9: VSC control dynamic block

Fig. 3.12 shows the modulation index block. The input is *dq*-frame converter reference voltage and dc voltage in p.u. value. And the output is converter voltage for RL filter dynamic computation. The purpose is to couple with dc-link voltage in VSC control.

Fig. 3.13 gives the insight of RL filter dynamic block. The converter voltage is firstly converted from converter reference to grid reference using PLL computed angle difference. Then, the PCC current is computed by derivative equations. Eq. 3.5 gives an example of dynamic equations on bus 2, where $v_{2t,dq}$ is the voltage on converter terminal. R_f and L_f represents the RL filter.

$$\frac{di_{2,d}}{dt} = \frac{1}{L_f}(v_{2t,d} - v_{2,d} - R_f i_{2,d} + \omega_0 L_f i_{2,q}) \tag{3.5a}$$

$$\frac{di_{2,q}}{dt} = \frac{1}{L_f}(v_{2t,q} - v_{2,q} - R_f i_{2,q} - \omega_0 L_f i_{2,d}) \tag{3.5b}$$

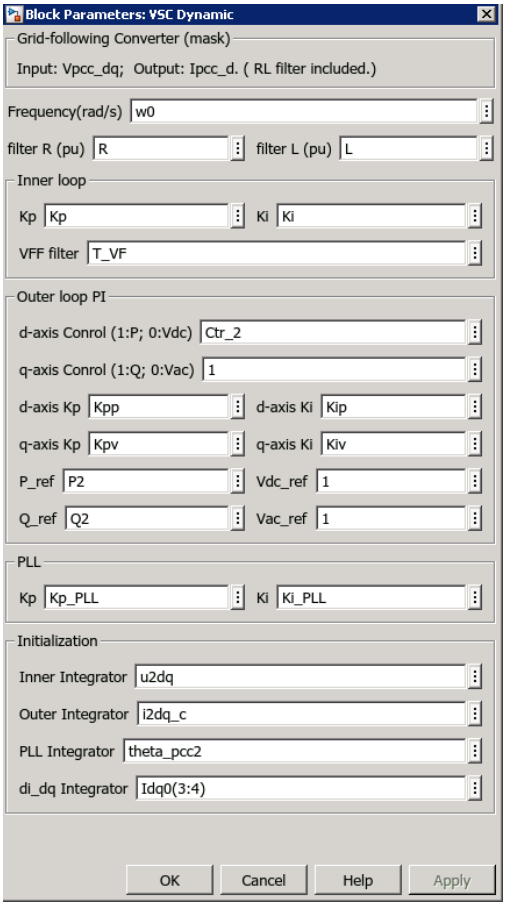

Figure 3.10: VSC control dynamic mask parameters

3.2.5.2 Battery Dynamic

The battery dynamic block is built based on a battery model and a DC/DC boost converter circuit, which is presented in Fig. 3.14. The battery output voltage V_{bat} is not constant. So that a DC/DC converter with controlled duty ratio (D) is required to regulate the output DC-link voltage (V_{dc}).

Based on the dc side circuit assumption in Fig. 3.14, the battery and DC/DC converter dynamic blocks are proposed in Fig. 3.15. The input is converter active power (P_{conv}) and output is DC side voltage (V_{dc}).

The battery model function is based on the lithium-ion battery model in [56]. E_s is expressed in (3.6).

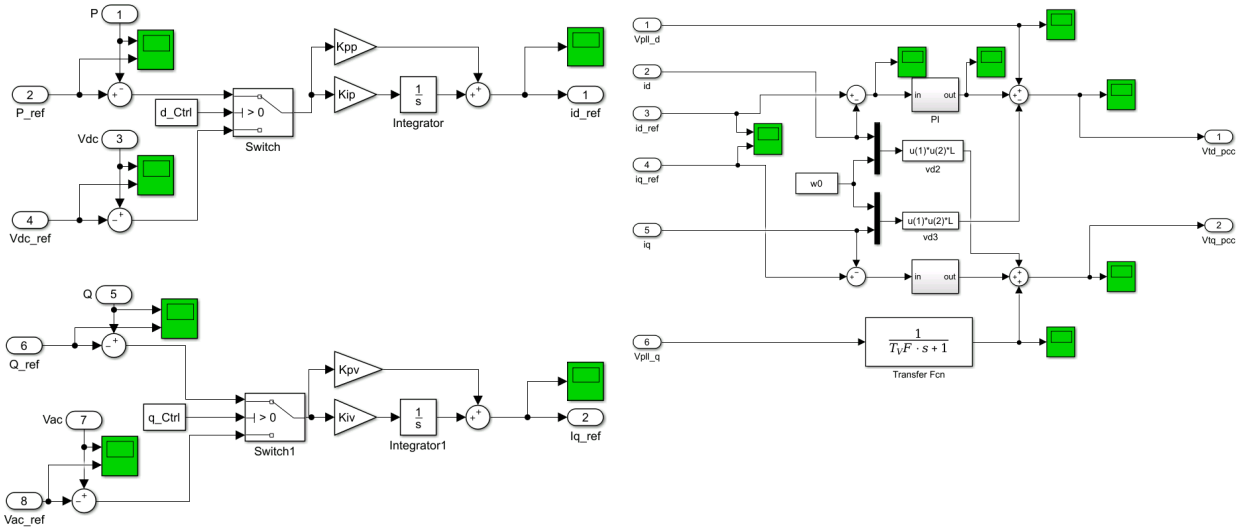

Figure 3.11: VSC control outer loop and inner loop

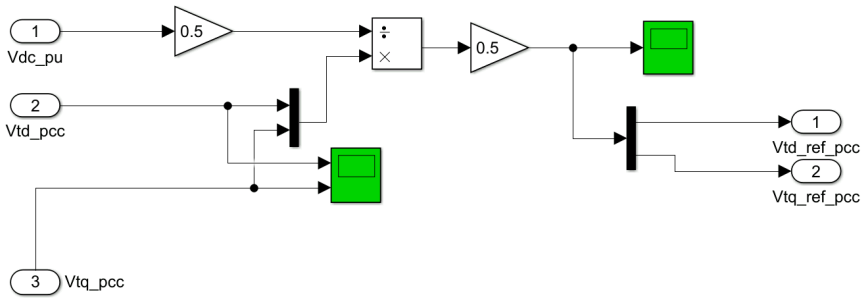

Figure 3.12: Modulation index block

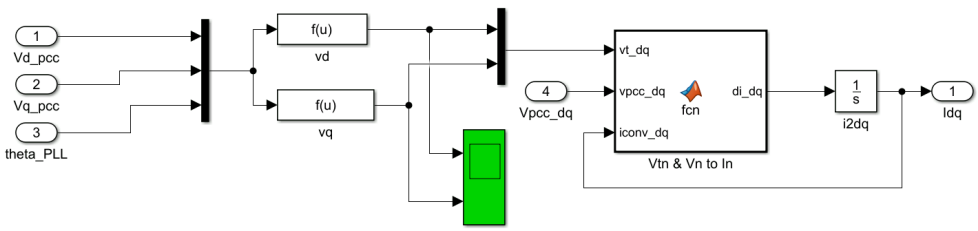

Figure 3.13: IBR RL filter dynamic block

$$E_s = E_0 - K\frac{Q}{Q - \int I_L} + A\exp(-B \cdot \int I_L) \tag{3.6}$$

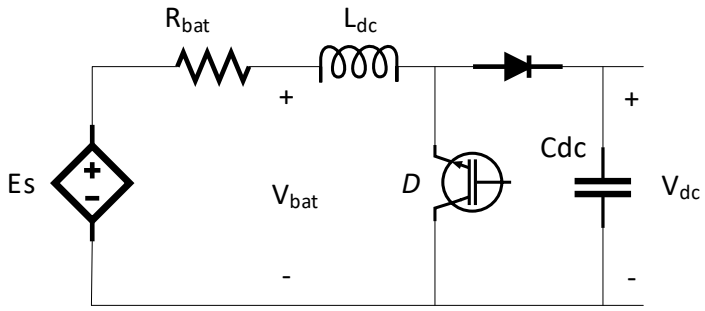

Figure 3.14: Battery dynamic circuit

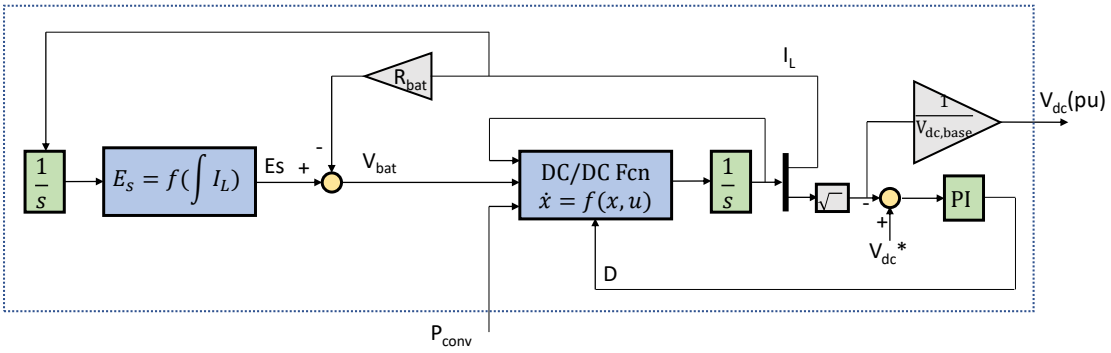

Figure 3.15: Battery dynamic blocks

There are two derivative dynamic equations in DC/DC function block. They are given in (3.7).

$$\frac{dI_L}{dt} = \frac{1}{L_{\text{dc}}}(V_{\text{bat}} - (1-D)V_{\text{dc}}) \tag{3.7a}$$

$$\frac{dV_{\text{dc}}^2}{dt} = \frac{2}{C_{\text{dc}}}(I_L \cdot V_{\text{bat}} - P_{\text{conv}}) \tag{3.7b}$$

All the parameters and initial values are defined in the mask, which shown in Fig. 3.16.

3.2.5.3 PV Dynamic

The PV solar dynamic block is built based on a circuit shown in Fig. 3.17. There is a constant DC voltage source behind a series RL circuit.

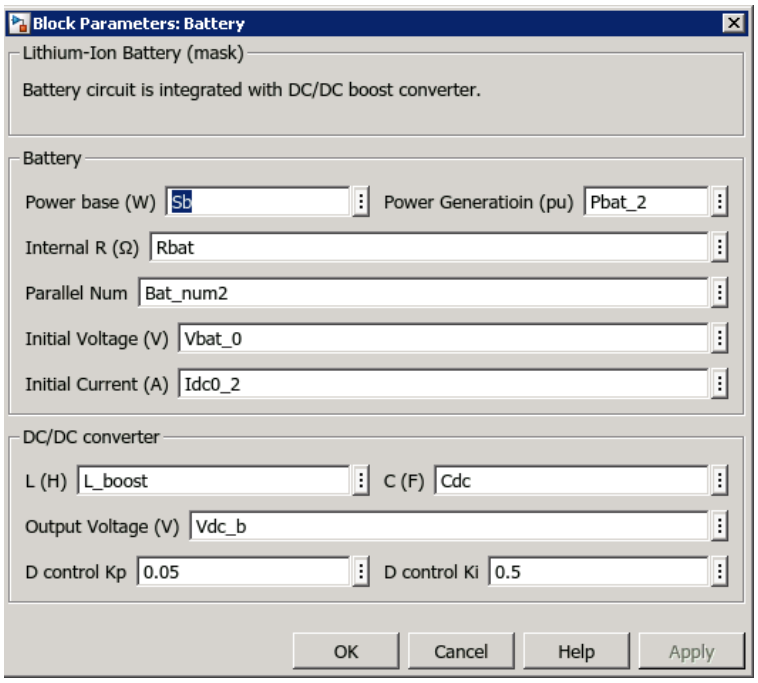

Figure 3.16: Battery mask parameters

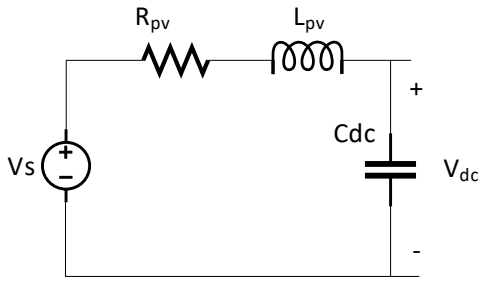

Figure 3.17: PV dynamic circuit

According to the assumption in Fig. 3.17, the PV dynamic block diagram is proposed as Fig. 3.18.

In PV dynamic block, there are two derivative equations are included. They are expressed in (3.8).

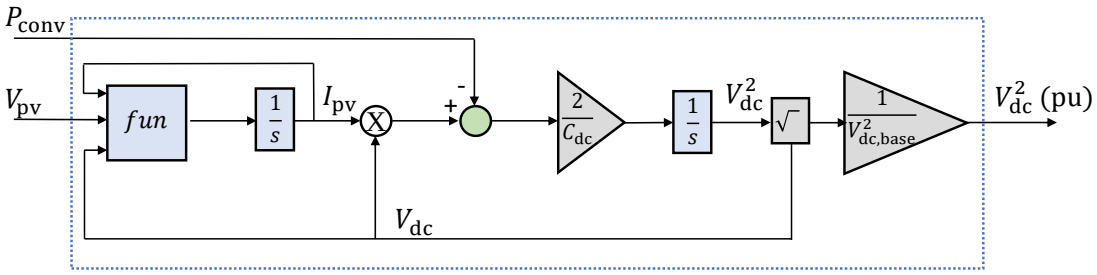

Figure 3.18: PV dynamic blocks

$$\frac{dI_{pv}}{dt} = \frac{1}{L_{pv}}(V_s - V_{dc} - R_{pv}I_{pv}) \tag{3.8a}$$

$$\frac{dV_{dc}^2}{dt} = \frac{2}{C_{dc}}(I_{pv} \cdot V_{dc} - P_{conv}) \tag{3.8b}$$

All parameters can be access through the mask of PV block in Fig. 3.19. Those values are defined in the initial file.

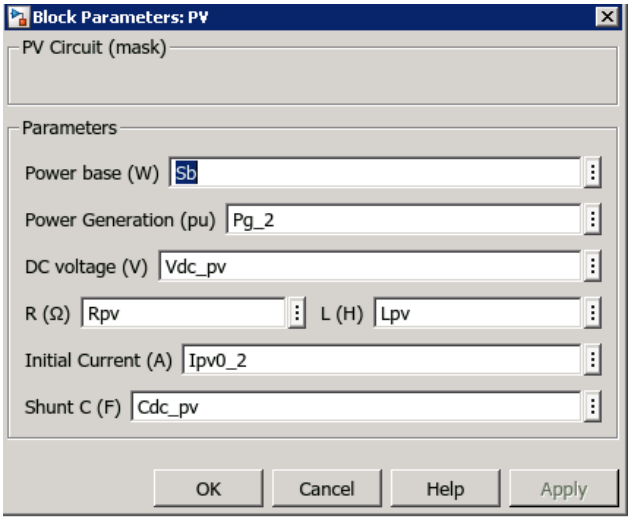

Figure 3.19: PV mask parameters

3.2.6 Time-based Simulation

Using the Simulink state-space model, a test simulation case it presented here. At $t = 1s$, the active power order on bus 2 IBR are increased 0.1 p.u. The node voltages and current injections on 6 buses are shown in Fig. 3.20. (a) is active power on bus 2 IBR control, where blue line is P_2^{ref}, red line is P_2^{meas}. (b) is node voltage in dq-domain. (c) is node current injection in dq-domain. It can be seen the model initialization is correct since it has a flat run. And the VSC control loop works well.

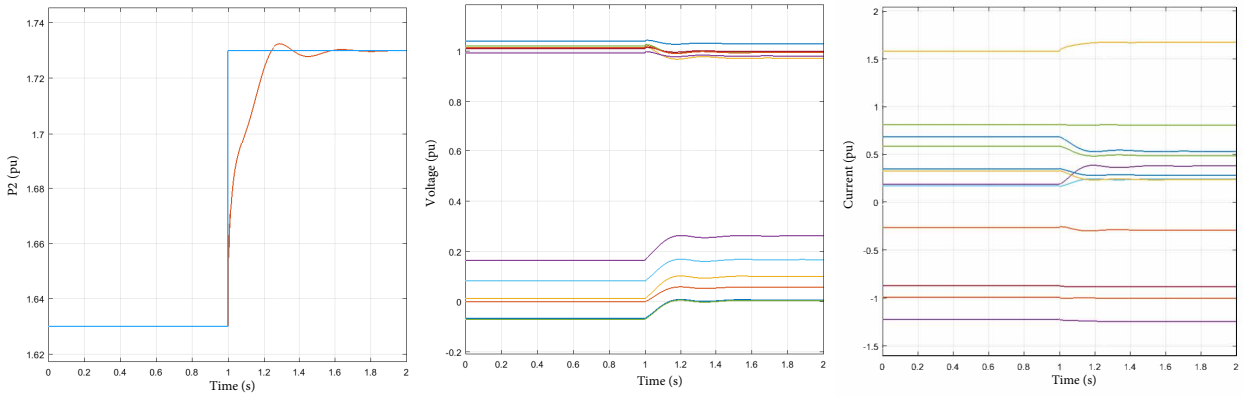

(a) (b) (c)

Figure 3.20: State-space model dynamic responses on bus 2 IBR control active power order step change

3.3 Linear Admittance Modeling

In this section, it will illustrate the detailed process of dq-frame admittance modeling in s-domain. Similar to the nonlinear state-space modeling process, the Kron reduction will be first conducted to reduce the system size.

3.3.1 Network Admittance Matrix

For a n-bus system, the n by n $\boldsymbol{Y}_{\text{bus}}$ matrix will be converted to a $2n$ by $2n$ dq-frame s-domain transfer function $\boldsymbol{Y}_{\text{net}}^{dq}$.

3.3.1.1 Off-Diagonal Elements

The off-diagonal elements are decided by the branch admittance from $\boldsymbol{Y}_{\text{bus}}$ matrix. Assume the admittance between two different buses i and j is $Y_{ij} = G_{ij} + jB_{ij}$. The impedance can be get by

$$Z_{ij} = \frac{1}{Y_{ij}} = R_{ij} + jX_{ij} \tag{3.9}$$

Written it in dq-frame s-domain:

$$\boldsymbol{Z}_{ij}^{dq} = \begin{bmatrix} R_{ij} + \dfrac{X_{ij}}{\omega_0}s & -X_{ij} \\ X_{ij} & R_{ij} + \dfrac{X_{ij}}{\omega_0}s \end{bmatrix} \tag{3.10}$$

Then the 2 by 2 branch admittance transfer function between bus i and bus j can be got by $\boldsymbol{Y}_{ij}^{dq} = \dfrac{1}{\boldsymbol{Z}_{ij}^{dq}}$. Therefore, the off-diagonal element related to bus i and j will be

$$\boldsymbol{Y}_{\text{net}}^{dq}((2i-1):2i,\ (2j-1):2j) = -\boldsymbol{Y}_{ij}^{dq} \tag{3.11}$$

3.3.1.2 Diagonal Elements

There are three components are considered on the diagonal elements computation: branch admittance, capacitance, and load admittance.

At bus i, the connected branch admittance is carried out by (3.12).

$$\boldsymbol{Y}_{l,i}^{dq} = \sum_j \boldsymbol{Y}_{ij}^{dq}, \quad j \in \mathcal{N}_i \tag{3.12}$$

where $\mathcal{N}_i$ indicates the set of bus i's neighbors.

The equivalent capacitance on bus i can be converted to s-domain using (3.13). Note that B_{ij} is the capacitance on branch $i - j$.

$$\boldsymbol{Y}_{c,i}^{dq} = \begin{bmatrix} \dfrac{B_i}{\omega_0}s & -B_i \\ B_i & \dfrac{B_i}{\omega_0}s \end{bmatrix}, \quad \text{where } B_i = \frac{1}{2}\sum_j B_{ij},\ j \in \mathcal{N}_i \tag{3.13}$$

To compute the load admittance on bus i. We should first identify it is a RL load or RC load. If it is a RL load, i.e., $Q_d > 0$, the impedance can be got by (3.14).

$$Z_{d,i} = -\frac{\overline{V_i}}{\overline{I_i}} = R_{d,i} + jX_{d,i} \tag{3.14}$$

where $\overline{V_i}$ and $\overline{I_i}$ are voltage and injected current on bus i.

$$\boldsymbol{Z}_{d,i}^{dq} = \begin{bmatrix} R_{d,i} + \dfrac{X_{d,i}}{\omega_0}s & -X_{d,i} \\ X_{d,i} & R_{d,i} + \dfrac{X_{d,i}}{\omega_0}s \end{bmatrix} \tag{3.15}$$

The s-domain admittance of RL load on bus i can be got by (3.16).

$$\boldsymbol{Y}_{d,i}^{dq} = \frac{1}{\boldsymbol{Z}_{d,i}^{dq}} \tag{3.16}$$

If the load is a RC load, i.e., $Q_d < 0$, the load admittance is calculated by

$$Y_{d,i} = -\frac{\overline{I_i}}{\overline{V_i}} = G_{d,i} + jB_{d,i} \tag{3.17}$$

Then,

$$\boldsymbol{Y}_{d,i}^{dq} = \begin{bmatrix} G_{d,i} + \dfrac{B_{d,i}}{\omega_0}s & -B_{d,i} \\ B_{d,i} & G_{d,i} + \dfrac{B_{d,i}}{\omega_0}s \end{bmatrix} \tag{3.18}$$

Finally, the diagonal element of $\mathbf{Y}_{\text{net}}^{dq}$ can be calculated by sum of (3.12), (3.13), (3.16) or (3.18).

$$\mathbf{Y}_{\text{net}}^{dq}((2i-1):2i,(2i-1):2i) = \mathbf{Y}_{l,i}^{dq} + \mathbf{Y}_{c,i}^{dq} + \mathbf{Y}_{d,i}^{dq} \tag{3.19}$$

The s-domain n-bus network admittance modeling process can be included in Algorithm 1.

Algorithm 1: $n-$bus network admittance modeling

Get $\boldsymbol{Y}_{\text{bus}}$ via MATPOWER toolbox;
for $i = 1:n,\ j = 1:n$ **do**
  if $i \neq j$ **then**
    $Z_{ij} = \frac{1}{Y_{ij}} = R_{ij} + jX_{ij}$;
    $$\boldsymbol{Y}_{\text{net}}^{dq}((2i-1):2i,\ (2j-1):2j) = -\begin{bmatrix} R_{ij} + \dfrac{X_{ij}}{\omega_0}s & -X_{ij} \\ X_{ij} & R_{ij} + \dfrac{X_{ij}}{\omega_0}s \end{bmatrix}^{-1};$$
  else
    $\boldsymbol{Y}_{l,i}^{dq} = \sum_j \boldsymbol{Y}_{ij}^{dq}, \quad j \in \mathcal{N}_i$;
    $$\boldsymbol{Y}_{c,i}^{dq} = \begin{bmatrix} \dfrac{B_i}{\omega_0}s & -B_i \\ B_i & \dfrac{B_i}{\omega_0}s \end{bmatrix}, \quad B_i = \tfrac{1}{2}\sum_j B_{ij}, j \in \mathcal{N}_i;$$
    if $Q_{d,j} > 0$ **then**
      $$\boldsymbol{Y}_{d,i}^{dq} = \begin{bmatrix} R_{d,i} + \dfrac{X_{d,i}}{\omega_0}s & -X_{d,i} \\ X_{d,i} & R_{d,i} + \dfrac{X_{d,i}}{\omega_0}s \end{bmatrix}^{-1}, \ R_{d,i} + jX_{d,i} = -\overline{V_i}/\overline{I_i};$$
    else
      $$\boldsymbol{Y}_{d,i}^{dq} = \begin{bmatrix} G_{d,i} + \dfrac{B_{d,i}}{\omega_0}s & -B_{d,i} \\ B_{d,i} & G_{d,i} + \dfrac{B_{d,i}}{\omega_0}s \end{bmatrix}, \quad G_{d,i} + jB_{d,i} = -\overline{I_i}/\overline{V_i};$$
    end
    $\boldsymbol{Y}_{\text{net}}^{dq}((2i-1):2i, (2i-1):2i) = \boldsymbol{Y}_{l,i}^{dq} + \boldsymbol{Y}_{c,i}^{dq} + \boldsymbol{Y}_{d,i}^{dq}$
  end
end

3.3.2 Generation Bus Admittance

Next, the admittance on the generation buses will be computed. The simplified synchronous generator can be replaced by a RL circuit admittance. And the IBR admittance can be carried out via linearizing the nonlinear state-space Simulink model.

3.3.2.1 Simplified Synchronous Generator

For the simplified RL circuit synchronous generator, we can get the impedance directly by (3.20).

$$\boldsymbol{Z}_{G,i}^{dq} = \begin{bmatrix} R_{s,i} + \dfrac{X_{s,i}}{\omega_0}s & -X_{s,i} \\ X_{s,i} & R_{s,i} + \dfrac{X_{s,i}}{\omega_0}s \end{bmatrix} \tag{3.20}$$

The s-domain admittance of synchronous generator on bus i can be got by (3.21).

$$\boldsymbol{Y}_{G,i}^{dq} = \frac{1}{\boldsymbol{Z}_{G,i}^{dq}} \tag{3.21}$$

3.3.2.2 IBR Admittance

Since the nonlinear state-space IBR dynamic block has been built in Simulink system. The IBR system linearzing admittance can be extracted by using MATLABT function `linmod`. In Fig. 3.21, the bus 2 IBR system s-domain admittance is abstracted by defining voltage as input and current as the output.

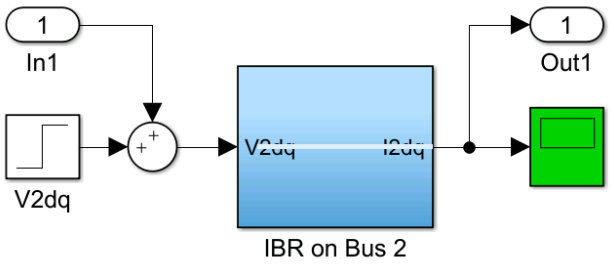

Figure 3.21: Abstract IBR admittance from Simulink block

3.3.3 Whole System Admittance

The whole system admittance can be obtained by adding generators admittance and IBR admittance to generation bus on the diagonal elements in $\boldsymbol{Y}$ matrix. (4.4) gives an example of

$$\boldsymbol{Y}_{\text{total}}(s) = \begin{bmatrix} \boldsymbol{Y}_{\text{net}}^{dq}(1:2,1:2) + \boldsymbol{Y}_{\text{G},1}^{dq} & \dots & \dots & \dots \\ \dots & \boldsymbol{Y}_{\text{net}}^{dq}(3:4,3:4) + \boldsymbol{Y}_{\text{IBR},2}^{dq} & \dots & \dots \\ \dots & \dots & \boldsymbol{Y}_{\text{net}}^{dq}(5:6,5:6) + \boldsymbol{Y}_{\text{IBR},3}^{dq} & \dots \\ \dots & \dots & \dots & \dots \end{bmatrix} \tag{3.22}$$

3.4 Eigenvalue Analysis

The eigenvalue analysis can be accessed from above mentioned two approaches. For the nonlinear state-space model, the integrated system will be linearized via `linmod` and use command `eig(A)` to get the eigenvalue from A matrix. For the linear admittance model, the eigenvalue of the whole system can be carried out by the $\texttt{det}[\boldsymbol{Y}_{\text{total}}(s)] = 0$.

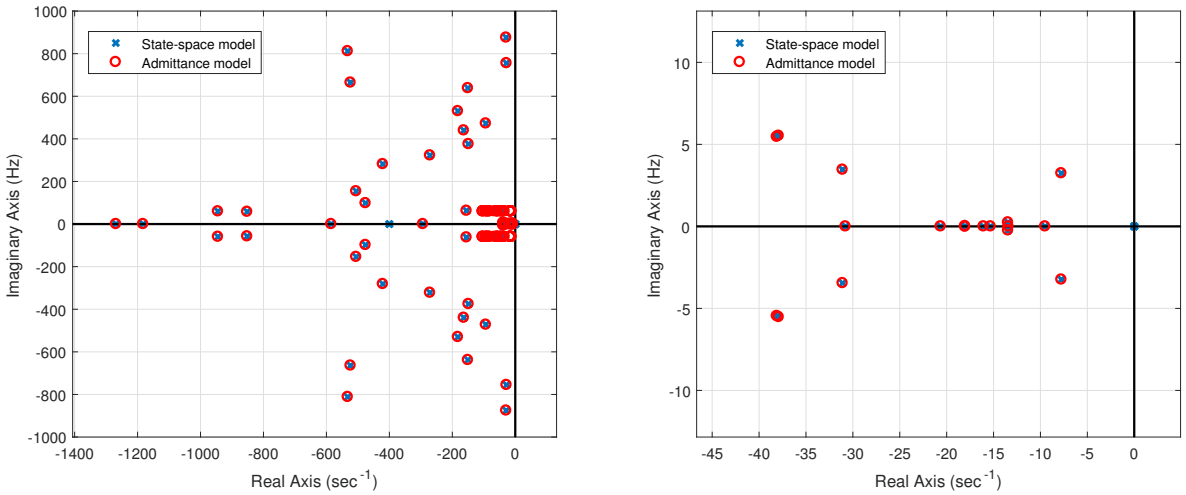

Figure 3.22: Eigenvalue analysis from two models

Fig. 3.22 shows the eigenvalue analysis conducted from two different approaches: nonlinear state-space model and linear admittance model. In this case, Two IBRs both adopt battery on DC

side dynamic assumption. It can be seen that two models can carry out same eigenvalues under a common assumption.

3.5 Conclusion

This chapter introduced two modeling approaches to integrate IBRs to scalable network system. One is extended work from chapter 1 to build scalable and general nonlinear state-space model in MATLAB/Simulink. Another is numerical linear s-domain network admittance modeling, which will be applied in the following admittance-based model analysis. Those two methods can conduct same eigenvalue analysis results, which can be used for system stability analysis.

Chapter 4: Admittance-based Small-Signal Analysis Using Frequency Scan Identification

In this chapter [2], it demonstrated how to perform eigenvalue-based stability analysis with only black-box original equipment manufacturer (OEM) models provided for a 100% IBR-penetrated IEEE 9-bus network. Frequency scanning measurement-based approach provides a basis of a new paradigm for small-signal analysis. The eigenvalue analysis can tell two things. One is that we can predict the system stability in small-signal analysis. Another is that the carried out modal analysis can tell which IBRs are associated to a particular oscillation mode. The analysis results are all confirmed by the electromagnetic transient (EMT) simulation results in PSCAD model. Some existing other recent papers [58–60] adopted the similar philosophy with admittance-based framework for meshed network analysis. In this research part, there are two unique features should be mentioned.

- A scalable Laplacian-domain admittance-based mode shape analysis toolbox is proposed and it will be verified via the IEEE 9-bus network with 3 IBRs system. Compared to the existing works on admittance-based modal analysis utilizing participation factor, obervability or controllability related voltage and current only [58–60]. Here, we significantly expands this type of analysis to not only *dq*-frame nodal voltage, but also any measurement, including voltage magnitudes, current magnitudes, real power, reactive power, and phase angles. The admittance-based mode shape analysis is able to predict involvement of each IBR in the dominant mode accurately.

- From both PSCAD EMT simulation and admittance-based mode shape analysis, it has been found that inter-area oscillations exist for a 100% IBR penetrated power grid. Different to

[2]The majority of this chapter has been submitted to IEEE Transactions on Power Delivery [57], which is under review by Oct 29th 2021.

the traditional inter-area oscillation frequency range, e.g., 0.25 Hz in the Western Electricity Coordinating (WECC) system, the investigated oscillation is about 3 Hz which caused by interaction between two GFM converters in this particular case.

The remaining part of this chapter is organized as follows. The first section introduces the IEEE 9-bus network and measurement-based admittance modeling. The second section presents the mode shape analysis techniques. The third section shows the EMT simulation results to validate the above analysis. Finally, it is concluded in the fourth section.

4.1 9-bus Network with 3-IBR Integrated System

In this section, IEEE 9-bus network system with 100% IBR penetration in PSCAD testbed will be introduced first. From on this EMT PSCAD model, three IBRs are measured to get their admittance and 9-bus system network admittance can be conducted based on system branch parameters. Therefore, the whole system Laplace-domain admittance-based matrix is integrated in dq-frame.

4.1.1 9-bus System Description

This 9-bus system is built in PSCAD software platform and shown as Fig. 4.1. It is modified by [9] with a zero-inertia operational scenario of 100% inverter-based generation where consists of two grid-forming (GFM) converters and one grid-following (GFL) converter. The total load size is 315 MW and the transmission network voltage level is 230 kV. The power base is 100 MW. Three IBRs are connected at Bus 1, Bus 2, and Bus 3 to be integrated into the 230-kV system via step up transformer. The IBRs are modeled as controllable three-phase voltage sources.

To create poorly damped 3-Hz oscillations, the GFL's outer control loop parameters and the GFM's virtual impedance parameters have been adjusted. The system branch parameters are listed in Table 4.1. The generation and load information is given in Table 4.2.

GFL and GFM converters control diagram is presented in Fig. 4.2. The corresponding circuit and control parameters are given in Table 4.3. For the GFL converter on bus 2, it adopts PQ power control loop in outer loop and current control in inner control loop. The PLL is enabled to

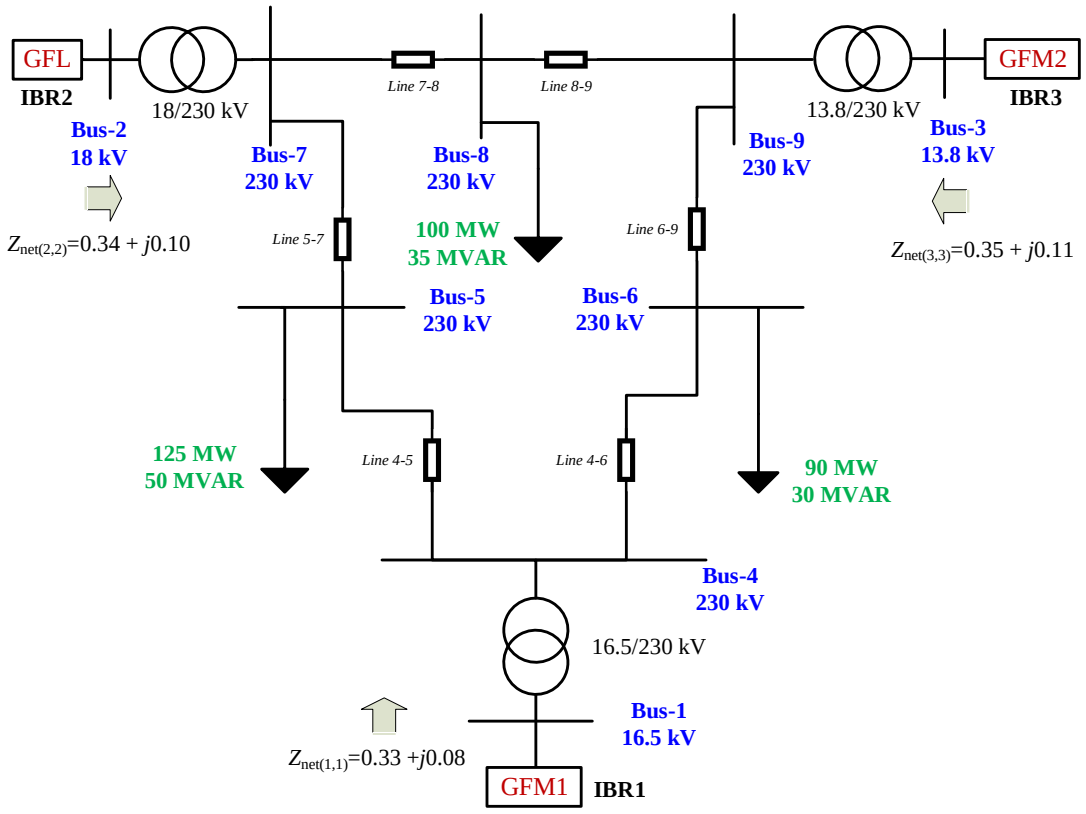

Figure 4.1: IEEE 9-bus network system with 100% IBR penetration

Table 4.1: IEEE 9-bus branch data

From	To	R (p.u.)	X (p.u.)	B (p.u.)
1	4	0	0.0576	0
4	8	0.017	0.092	0.158
6	9	0.039	0.17	0.358
3	9	0	0.0586	0
8	9	0.0119	0.1008	0.209
7	8	0.0085	0.072	0.14
2	7	0	0.0625	0
5	7	0.032	0.161	0.306
4	9	0.01	0.085	0.176

track the grid frame for controllers. For the GFM converters on bus 1 and bus 3, the outer control loop adopts virtual resistor adjusted voltage control loop with P/f and Q/V droop. PLL is only for measurement purpose and frequency is regulated by the P/f droop control. Note that the dc side dynamic is ignored and the converter terminal voltage is directly driven by controller three-phase signal ($V_{\text{tabc,ref}}$).

Table 4.2: 9 bus generators and loads data

Gen Bus	P_g (p.u.)	Q_g (p.u.)	$\overline{V}$ (p.u.)
1	0.71	0.27	$1.04\angle 0°$
2	1.63	0.04	$1.025\angle 9.3°$
3	0.85	-0.11	$1.025\angle 5.1°$

Load Bus	P_d (p.u.)	Q_d (p.u.)
5	0.90	0.3
6	1.0	0.35
8	1.25	0.5

Table 4.3: 9-bus GFL,GFM circuit and control parameters

Description	**Parameters**	**Value**
Power base	S_{b}	100 MVA
System frequency	f_{o}	60 Hz
GFL filter circuit	L_f, R_f	0.009, 0.016
GFL coupling circuit	L_c, R_c	0.0017,0.003
GFL current loop	K_{pi}, K_{ii}	0.38, 0.70
GFL power loop	K_{pp}, K_{ip}	0.5, 5
GFL PLL	$K_{\mathrm{p,pll}}$, $K_{\mathrm{i,pll}}$	52, 415
GFM filter circuit	L_f, R_f, C_f	0.15, 0.005, 2.6,
GFM coupling circuit	L_c, R_c	0.015, 0.0005
GFM virtual resistor	R_v	0.4
GFM current loop	K_{pi}, K_{ii}	0.73, 1.19
GFM voltage loop	K_{pv}, K_{iv}	0.52, 1.16
GFM P-f, Q-V droop	K_{pf}, K_{qv}	0.05, 0.05

4.1.2 IBR Admittance Measurement

Fig. 4.3 shows the frequency scan [32, 33] measurement methodology to get the admittance for each IBR. Each one is taken off from the grid and connected to a 60-Hz controllable voltage source via a RL branch. The voltage source's dq components are adjusted so that the IBR's terminal voltage phasor, real power, reactive power are exactly the same as those in the IEEE 9-bus system.

An injection of 0.1 p.u. magnitude at a frequency f_i, notated as ($V_{\mathrm{s,dinj}}$), is superimposed on the d-axis voltage. This dq frame is based on the angle $\omega_0 t$ where $\omega_0 = 377$ rad/s. The three-phase current flowing into the IBR is converted to the same dq frame. The phasors at that frequency are extracted via Fourier transform from the dq currents. Ratios of the dq current phasors against

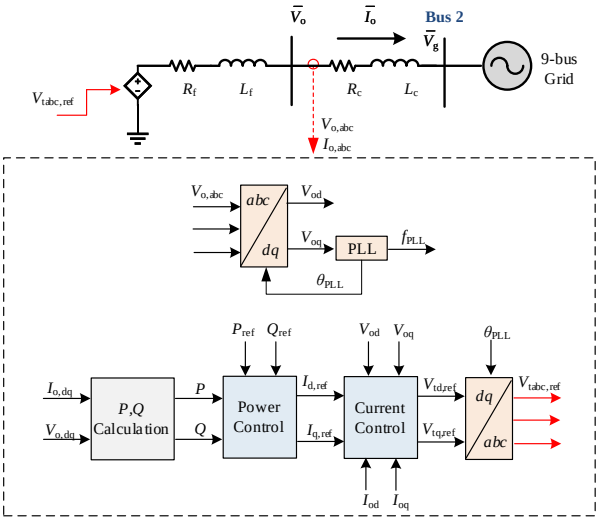

(a)

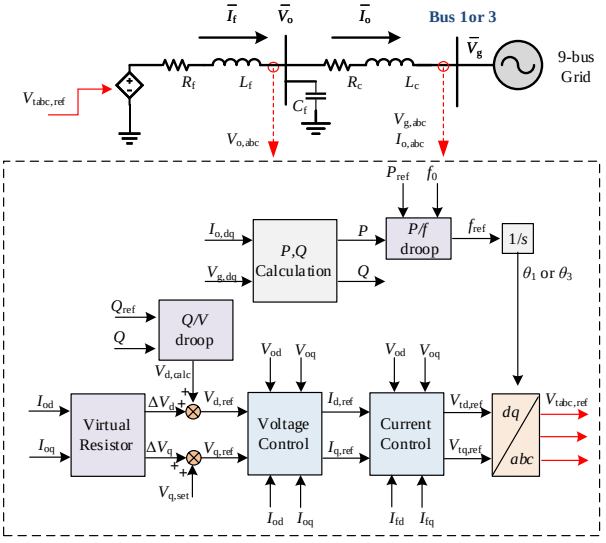

(b)

Figure 4.2: GFL and GFM converters control diagram

the injected d-axis voltage are the admittance components $Y_{\mathrm{s,dd}}$ and $Y_{\mathrm{s,qq}}$. Similarly, a harmonics injection at the q-axis voltage and the processing of the dq frame current measurement lead to the identification of $Y_{\mathrm{s,dq}}$ and $Y_{\mathrm{s,qq}}$. At each frequency measurement point, the measured admittance in dq-domain is written as equation (4.1).

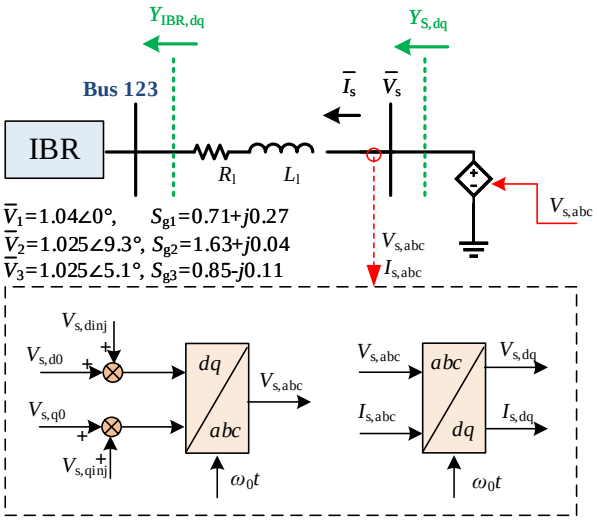

Figure 4.3: IBR admittance measurement using frequency scan method in dq-frame

$$\boldsymbol{Y}_{\mathrm{s}}(f_i) = \begin{bmatrix} Y_{\mathrm{s,dd}}(f_i) & Y_{\mathrm{s,dq}}(f_i) \\ Y_{\mathrm{s,qd}}(f_i) & Y_{\mathrm{s,qq}}(f_i) \end{bmatrix} = \begin{bmatrix} \dfrac{I_{\mathrm{s,d}}(f_i)}{V_{\mathrm{s,d}}(f_i)} & \dfrac{I_{\mathrm{s,d}}(f_i)}{V_{\mathrm{s,q}}(f_i)} \\ \dfrac{I_{\mathrm{s,q}}(f_i)}{V_{\mathrm{s,d}}(f_i)} & \dfrac{I_{\mathrm{s,q}}(f_i)}{V_{\mathrm{s,q}}(f_i)} \end{bmatrix} \tag{4.1}$$

It should be pointed out that admittance measurements are influenced by not only operation conditions but also the assumed reference frame. Therefore, all three IBRs are measured using a unique reference based on IBR1's angle. Additionally, each IBR's operating condition have to be kept the same as the online working condition during the measurement process. Using Python programming to call the PSCAD testbed model from 1 Hz to 100 Hz, the frequency scanning procedure are conducted automatically.

With the measured $\boldsymbol{Y}_s$ in range of [1,100] Hz, The IBR admittance can be obtained by removing the RL branch line. The frequency responses of $Y^{dq}_{\mathrm{IBR},1}$, $Y^{dq}_{\mathrm{IBR},2}$, $Y^{dq}_{\mathrm{IBR},3}$ are presented in Fig. 4.4. (a) is IBR1 (GFM1); (b) is IBR2 (GFL); (c) is IBR3 (GFM2). IBR1 and IBR3 measured admittance includes a RL $(0.03 + j0.3$ p.u.) branch. It shows two GFM converters have very similar frequency-domain responses although they are working in different conditions. The GFL converter has a different frequency response. Vector fitting [34] is implemented to find each IBR's admittance transfer function. And Fig. 4.4 shows that the model generated from vector fitting has a matching result with the measurement data.

4.1.3 Electric Network Admittance

In the last chapter, the derivation of IEEE 9-bus network has been introduced. Thus, the s-domain network admittance matrix can be built analytically. The loads are assumed as constant impedance loads and can be included in the network admittance matrix.

For an n-bus system, its dq admittance matrix has a dimension of $2n \times 2n$. The bandwidth of the EMT dynamics of the network is in the high frequency range if there is no series compensation in the system.

4.1.3.1 Kron Reduction

For a large network, the system should be simplified to have a low order $\boldsymbol{Y}$ matrix and make the computation efficient. Kron reduciton is an approach to achieve that purpose.

Kron reduction methodology has been applied to electrical system graphs [61]. For a $3-$bus system, if node 3 has zero current injection (i.e, $I_3 = 0$). Then we can eliminate node 3 to get the reduced admittance matrix, shown as (4.2). The obtained item can be expressed by (4.3).

$$\begin{bmatrix} \boldsymbol{I}_1 \\ \boldsymbol{I}_2 \\ 0 \end{bmatrix} = \begin{bmatrix} \boldsymbol{Y}_{11} & \boldsymbol{Y}_{12} & \boldsymbol{Y}_{13} \\ \boldsymbol{Y}_{21} & \boldsymbol{Y}_{22} & \boldsymbol{Y}_{23} \\ \boldsymbol{Y}_{31} & \boldsymbol{Y}_{32} & \boldsymbol{Y}_{33} \end{bmatrix} \begin{bmatrix} \boldsymbol{V}_1 \\ \boldsymbol{V}_2 \\ \boldsymbol{V}_3 \end{bmatrix} \tag{4.2a}$$

$$\begin{bmatrix} \boldsymbol{I}_1 \\ \boldsymbol{I}_2 \end{bmatrix} = \begin{bmatrix} \boldsymbol{Y}'_{11} & \boldsymbol{Y}'_{12} \\ \boldsymbol{Y}'_{21} & \boldsymbol{Y}'_{22} \end{bmatrix} \begin{bmatrix} \boldsymbol{V}_1 \\ \boldsymbol{V}_2 \end{bmatrix} \tag{4.2b}$$

$$\boldsymbol{Y}'_{\mathrm{ij}} = \boldsymbol{Y}_{\mathrm{ij}} - \frac{\boldsymbol{Y}_{\mathrm{ik}} \boldsymbol{Y}_{\mathrm{kj}}}{\boldsymbol{Y}_{\mathrm{kk}}} \tag{4.3}$$

Hence, the IEEE 9-bus system can be reduced to a 3-bus system, which only include three generation buses. For the load bus, we just need to equivalent the load to a shunt admittance branch and attach it to $\boldsymbol{Y}$ bus matrix. Then the current injection on load bus will be zero and ready to be removed.

To validate the Kron reduction derived admittance matrix, eigenvalues from original 9-bus system and reduced 3-bus system should be exactly same. They are plotted together in Fig. 4.5.

4.1.4 Total Admittance

With the three IBR's admittances and network admittance known, the total admittance model may be constructed, as shown in (4.4). Therefore, the eigenvalues of the system can be found by the zeros of total admittance matrix $\boldsymbol{Y}_{\text{total}}(s)$ or the poles of the impedance matrix $\boldsymbol{Z}_{\text{total}}(s)$.

$$\boldsymbol{Y}_{\text{total}}(s) = \begin{bmatrix} \boldsymbol{Y}^{dq}_{\text{net}}(1:2,1:2) + \boldsymbol{Y}^{dq}_{\text{IBR},1} & \dots & \dots & \dots \\ \dots & \boldsymbol{Y}^{dq}_{\text{net}}(3:4,3:4) + \boldsymbol{Y}^{dq}_{\text{IBR},2} & \dots & \dots \\ \dots & \dots & \boldsymbol{Y}^{dq}_{\text{net}}(5:6,5:6) + \boldsymbol{Y}^{dq}_{\text{IBR},3} & \dots \\ \dots & \dots & \dots & \dots \end{bmatrix} \tag{4.4}$$

From Fig. 4.5, it can be seen that the system has a 3-Hz mode close to the imaginary axis, indicating poor damping of the oscillation mode. In addition, the system has a few real-axis eigenvalues in the right-half-plane (RHP). These modes are questionable since the IBRs are measured for a frequency range of 1 Hz to 100 Hz, the fitted models of IBR may not capture the dynamics below 1 Hz accurately. The resulting modes or eigenvalues beyond this region (1 Hz to 100 Hz) may not be accurate.

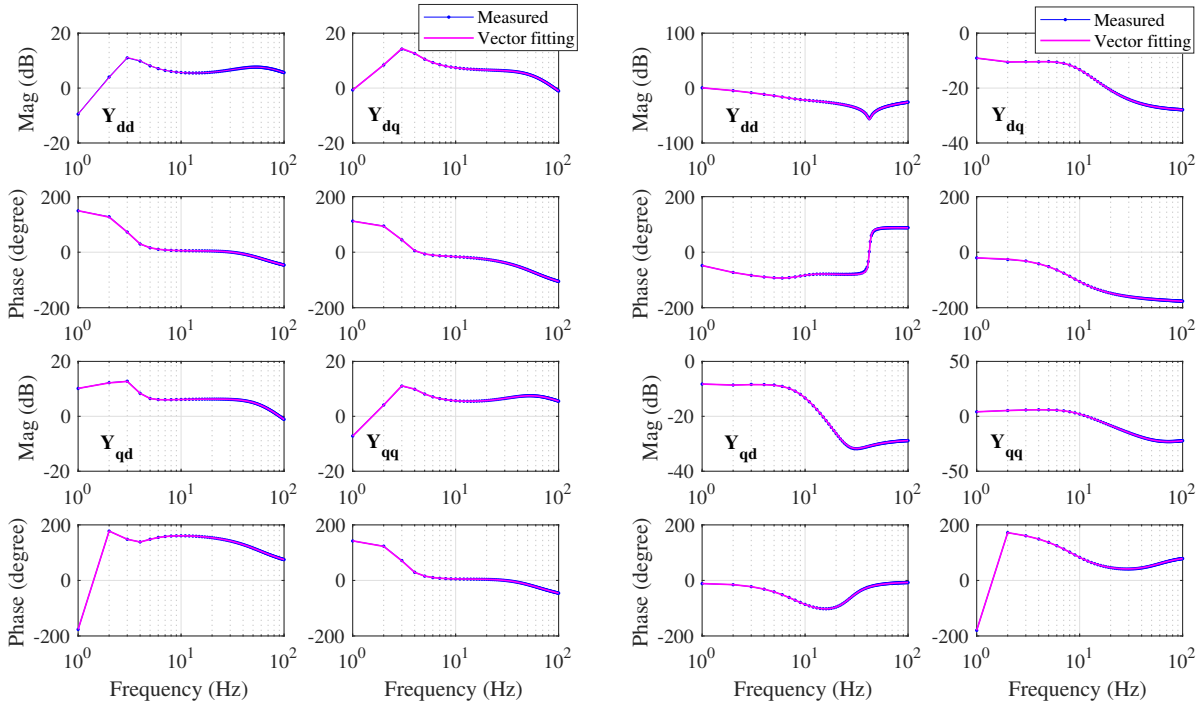

(a)

(b)

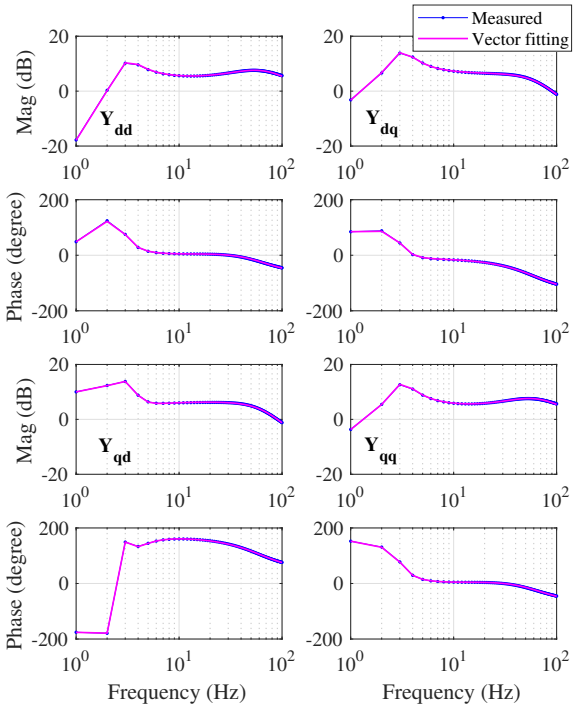

(c)

Figure 4.4: Admittance measurement of IBR1, IBR2, and IBR3 in *dq*-frame

4.2 Admittance-Based Model Analysis

s-domain admittance matrix has been used to compute system eigenvalues to predict system stability since 1999 [41]. And participation factor analysis can be applied to find influencing factors via eigenvalue decomposition of admittance or impedance matrix [58].

Instead of using participation factor, here we employ mode shape analysis. The basic mode shape analysis is limited to the dq-frame nodal voltages. On the other hand, how a mode influences the measurements, i.e, nodal voltage magnitudes and angles, current magnitudes, real and reactive power output from IBRs.

4.2.1 Basic Mode Shape Analysis

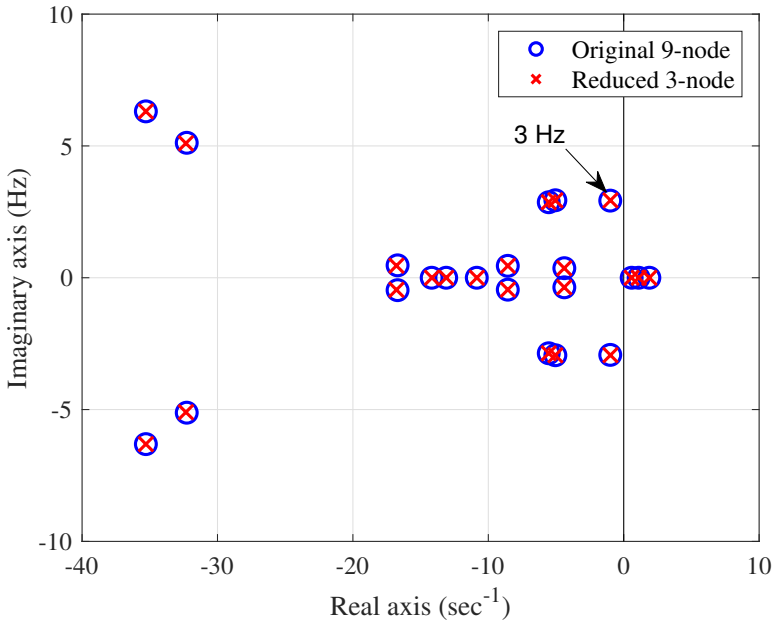

Figure 4.5: Poles in low-frequency range of $\boldsymbol{Z}_{\text{total}}(s)$

An eigenvalue λ_i can be carried out from the impedance matrix using $\texttt{pole}(\boldsymbol{Z}_{rmtotal}(s))$. The eigenvalues of IEEE 9-bus system with three IBRs are shown in Fig. 4.5. A 3-Hz mode can indicate the reason that caused a poorly damped 3-Hz oscillation.

Evaluate the bus impedance matrix $\boldsymbol{Z}_{\text{total}}(s)$ for an eigenvalue λ_i by letting $s = \lambda_i$. Since the eigenvalue is a pole of the bus impedance matrix, the evaluation at impedance matrix $\boldsymbol{Z}(\lambda_i)$ will approach infinity. Eigenvalue decomposition of $\boldsymbol{Z}(\lambda_i)$ leads to matrix factorization as follows.

$$\boldsymbol{Z}(\lambda_{\text{i}}) = \boldsymbol{Q}\boldsymbol{\Gamma}\boldsymbol{Q}^{-1} \tag{4.5}$$

where Q is the right eigenvector of $\boldsymbol{Z}(\lambda_i)$ and and $\boldsymbol{\Gamma}$ is a diagonal matrix consisting of $2n$ eigenvalues: γ_i, $i = 1, \ldots, 2n$.

Fig. 4.6 give the magnitude of the 18 eigenvalues of the bus impedance matrix at 3-Hz dominant mode $\boldsymbol{Z}(\lambda_{3\text{Hz}})$. And γ_1 is the maximum one. It can be seen from Fig. 4.6 that compared to γ_1, the rest eigenvalues have negligible magnitudes.

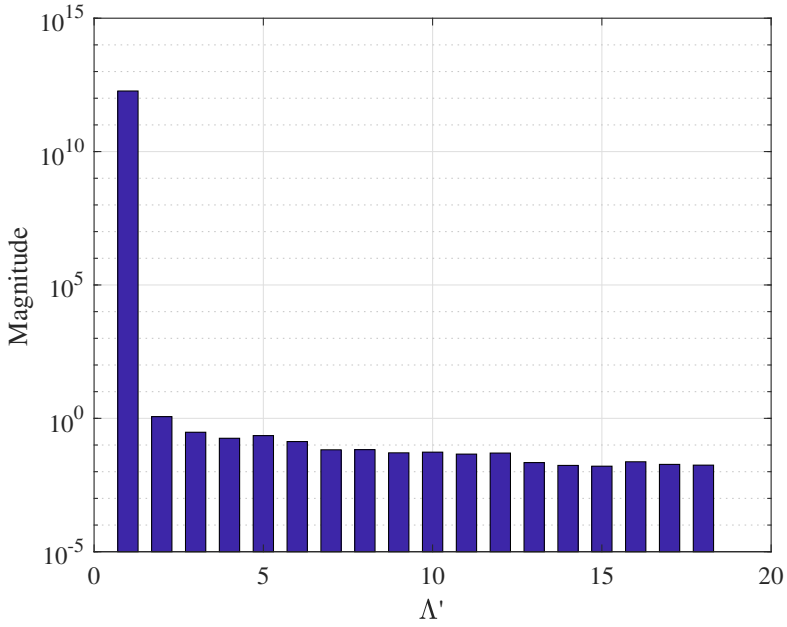

Figure 4.6: Magnitude plot of $\boldsymbol{\Gamma}$ regarding $Z(\lambda_{3\text{Hz}})$ eigenvalue decomposition

The relationship between the nodal voltage vector and the nodal current injection vector can be written follows.

Rewrite (4.5) as (4.6a).

$$\boldsymbol{V} = \boldsymbol{Z}(\lambda_i)\boldsymbol{I}(\lambda_i) \tag{4.6a}$$

$$= [\boldsymbol{Q}_{c,1}\ \boldsymbol{Q}_{c,2} \cdots \boldsymbol{Q}_{c,2n}] \begin{bmatrix} \gamma_1 & & & \\ & \gamma_2 & & \\ & & \ddots & \\ & & & \gamma_{2n} \end{bmatrix} \begin{bmatrix} \boldsymbol{Q}_{r,1}^{-1} \\ \boldsymbol{Q}_{r,2}^{-1} \\ \vdots \\ \boldsymbol{Q}_{r,2n}^{-1} \end{bmatrix} \boldsymbol{I} \tag{4.6b}$$

$$= \sum_{i=1}^{2n} \boldsymbol{Q}_{c,i}\gamma_i\boldsymbol{Q}_{r,i}^{-1}\boldsymbol{I} \approx \boldsymbol{Q}_{c,1}\gamma_1\boldsymbol{Q}_{r,1}^{-1}\boldsymbol{I} \tag{4.6c}$$

where $\boldsymbol{Q}_{c,i}$ is the ith column vector of $\boldsymbol{Q}$ and $\boldsymbol{Q}_{r,i}^{-1}$ is the ith row vector in $\boldsymbol{Q}^{-1}$. γ_1 is the eigenvalue with maximal absolute value, or the one reaching infinity. The corresponding 1st column eigenvector is expressed as:

$$\boldsymbol{Q}_{c,1} = \begin{bmatrix} \mathcal{V}_{\mathrm{d1}} & \mathcal{V}_{\mathrm{q1}} & \dots & \mathcal{V}_{\mathrm{dn}} & \mathcal{V}_{\mathrm{qn}} \end{bmatrix}^T \tag{4.7}$$

$\mathcal{V}_{\mathrm{d1}}$ and $\mathcal{V}_{\mathrm{q1}}$ can be used to examine how eigenvalue λ_i contribute to each bus voltage in dq-frame. For the 9-bus system, n is 9. E.g., V_{d1} and V_{q1} represent the contributions of eigenvalue λ_i to bus 1 voltage. The column vector $Q_{c,1}$ is the mode shape vector of the eigenvalue λ_i. Each element is a complex number reflecting the observability of the eigenvalue λ_i in the corresponding measurement.

4.2.2 Extended Mode Shape Analysis

The basic mode shape is not sufficient enough to evaluate the observability of an eigenvalue on measurements such as nodal voltage magnitudes, angles, or IBRs' output currents, real and reactive power. To find any mode shape for a general measurement, the relationship of the measurement of interest against the nodal voltage in the dq-frame is explored.

Thus, the bus i's voltage magnitude mode shape can be derived in (4.8).

$$\mathcal{V}_{\mathrm{mi}} = \frac{\partial V_{\mathrm{mi}}}{\partial V_{\mathrm{di}}}\mathcal{V}_{\mathrm{di}} + \frac{\partial V_{\mathrm{mi}}}{\partial V_{\mathrm{qi}}}\mathcal{V}_{\mathrm{qi}}, \text{ where } V_{\mathrm{mi}} = \sqrt{V_{\mathrm{di}}^2 + V_{\mathrm{qi}}^2} \tag{4.8}$$

Substitute the value of V_{di}, V_{qi} in steady state, the value of $\mathcal{V}_{\mathrm{mi}}$ can be obtained. Fig. 4.7 (a) plots the voltage magnitude mode shape for bus 1,2,3.

An IBRs dq-frame current and its terminal voltage are related with its dq admittance. By evaluating the IBR1 admittance matrix frequency responses at eigenvalue $\lambda_{3\mathrm{Hz}}$. Using IBR1 as an example, bus 1 current mode shape on dq-frame can be calculated via (4.9).

$$\begin{bmatrix} \mathcal{I}_{\mathrm{d1}} \\ \mathcal{I}_{\mathrm{q1}} \end{bmatrix} = \mathbf{Y}_{\mathrm{IBR},1}^{dq}(\lambda_{3\mathrm{Hz}}) \begin{bmatrix} \mathcal{V}_{\mathrm{d1}} \\ \mathcal{V}_{\mathrm{q1}} \end{bmatrix} \tag{4.9}$$

Similarly, the current magnitude mode shape of bus 1 can be got from (4.10). The corresponding mode shape plot is given in Fig. 4.7 (b).

$$\mathcal{I}_{\mathrm{m1}} = \frac{\partial I_{\mathrm{m1}}}{\partial I_{\mathrm{d1}}}\mathcal{I}_{\mathrm{d1}} + \frac{\partial I_{\mathrm{m1}}}{\partial I_{\mathrm{q1}}}\mathcal{I}_{\mathrm{q1}}, \text{ where } I_{\mathrm{m1}} = \sqrt{I_{\mathrm{d1}}^2 + I_{\mathrm{q1}}^2} \tag{4.10}$$

Based on power computation equation (4.11). They can be linearized and active power and reactive power mode shape is conducted via (4.12). Fig. 4.7 (c) and (d) shows the mode shape plots of P and Q.

$$P_1 = V_{1\mathrm{d}}I_{1\mathrm{d}} + V_{1\mathrm{q}}I_{1\mathrm{q}} \tag{4.11a}$$

$$Q_1 = -V_{1\mathrm{d}}I_{1\mathrm{q}} + V_{1\mathrm{q}}I_{1\mathrm{d}} \tag{4.11b}$$

$$\begin{bmatrix} \mathcal{P}_1 \\ \mathcal{Q}_1 \end{bmatrix} = \begin{bmatrix} V_{\mathrm{d1}} & V_{\mathrm{q1}} \\ V_{\mathrm{q1}} & -V_{\mathrm{d1}} \end{bmatrix} \begin{bmatrix} \mathcal{I}_{\mathrm{d1}} \\ \mathcal{I}_{\mathrm{q1}} \end{bmatrix} + \begin{bmatrix} I_{\mathrm{d1}} & I_{\mathrm{q1}} \\ -I_{\mathrm{q1}} & I_{\mathrm{d1}} \end{bmatrix} \begin{bmatrix} \mathcal{V}_{\mathrm{d1}} \\ \mathcal{V}_{\mathrm{q1}} \end{bmatrix} \tag{4.12}$$

And the bus 1 angle mode shape can be carried out using (4.13). The angle 1,2,3 mode shape plot is given in Fig. 4.7 (e). That can be used for frequency oscillation dynamic analysis.

$$\mathcal{A}_1 = \frac{\partial \theta_1}{\partial V_{\mathrm{d1}}}\mathcal{V}_{\mathrm{d1}} + \frac{\partial \theta_1}{\partial V_{\mathrm{q1}}}\mathcal{V}_{\mathrm{q1}}, \text{ where } \theta_1 = \arctan(\frac{V_{\mathrm{q1}}}{V_{\mathrm{d1}}}) \tag{4.13}$$

In Fig. 4.7, the mode shape plots all show that the 3-Hz mode is more related to IBR1 and IBR3, while relatively less related to IBR2. IBR1 and IBR3 are two GFM converters. Furthermore, mode shapes of voltage, current, real and reactive power and angle all show that IBR1 and IBR3 oscillate against each other for this mode.

To understand how each IBR is related to the dominant 3-Hz oscillation, further eigenvalue analysis is conducted.

With the measured three admittances of IBR1, IBR2, and IBR3, there are seven scenarios are examined as follows.

- Case 1: all three IBRs are online.
- Case 2: only IBR1 is online. The other two IBRs are replaced by constant voltage sources.
- Case 3: only IBR2 is online. The other two IBRs are replaced by constant voltage sources.
- Case 4: only IBR3 is online. The other two IBRs are replaced by constant voltage sources.
- Case 5: IBR1 and IBR2 are online. The rest IBR is replaced by a constant voltage source.
- Case 6: IBR1 and IBR3 are online. The rest IBR is replaced by a constant voltage source.
- Case 7: IBR2 and IBR3 are online. The rest IBR is replaced by a constant voltage source.

Fig. 4.8(a) presents the system eigenvalues for Case 1, 2, 3, and 4. It is can be seen that the 3-Hz mode will be well damped if only one IBR is online.

Fig. 4.8(b) presents the system eigenvalues for Case 5, 6, and 7. It is obvious to see the 3-Hz mode becomes poorly damped only when IBR1 and IBR3 are online. IBR2 has no impact on the 3-Hz mode. Therefore, the 3-Hz poorly damped oscilaltion mode is caused by interaction of two GFM converters.

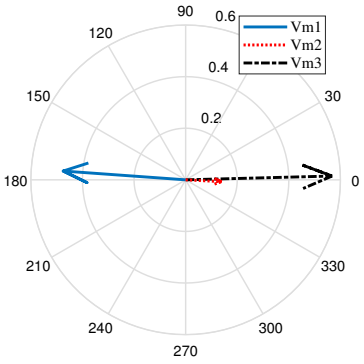

(a)

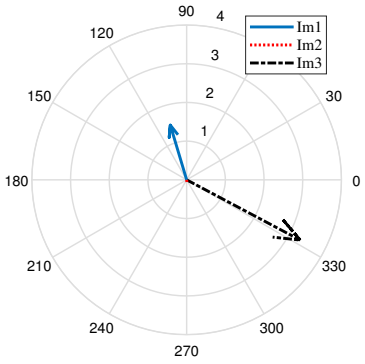

(b)

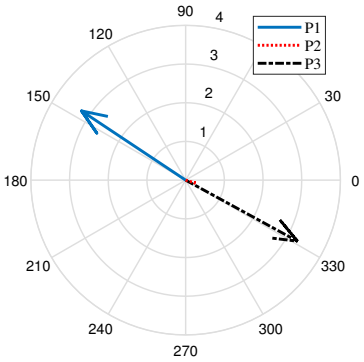

(c)

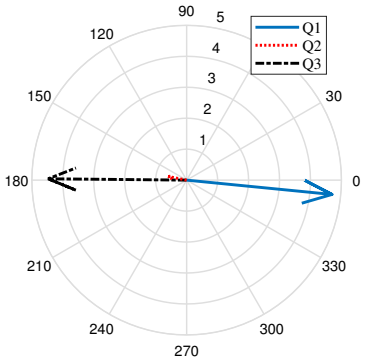

(d)

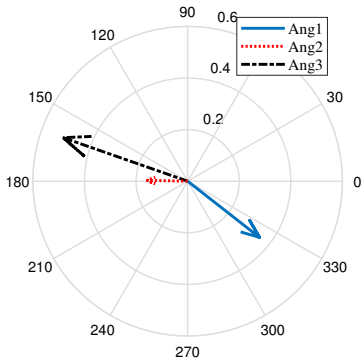

(e)

Figure 4.7: 9-bus system mode shape on bus 1,2,3

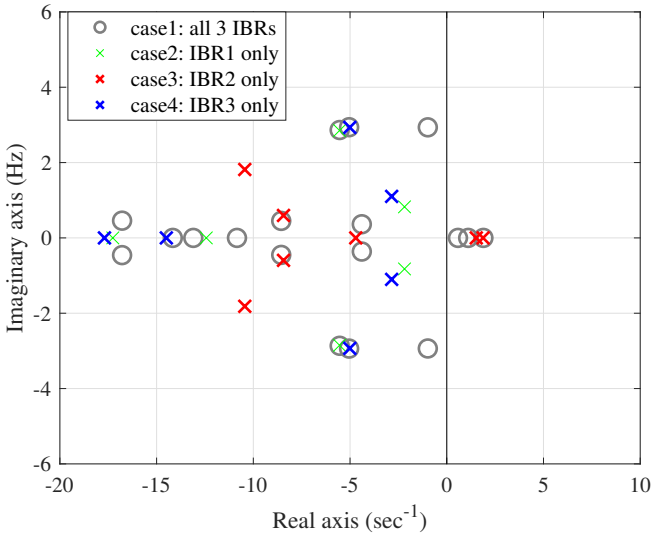

(a)

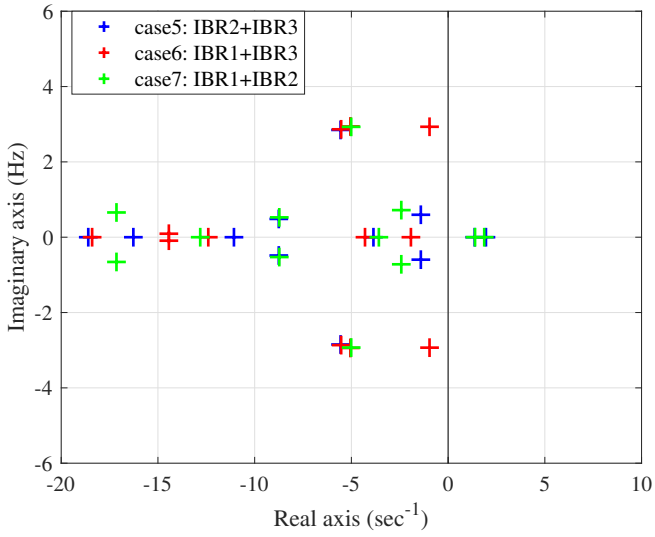

(b)

Figure 4.8: Poles in low-frequency range of $\boldsymbol{Z}_{\text{total}}(s)$ under different IBR combination cases

4.3 Validation in Time-Domain Simulation

In this section, the time-domain simulation results from PSCAD 9-bus EMT testbed are presented to validate above mentioned admittance-based mode shape analysis. There are six case studies are validated.

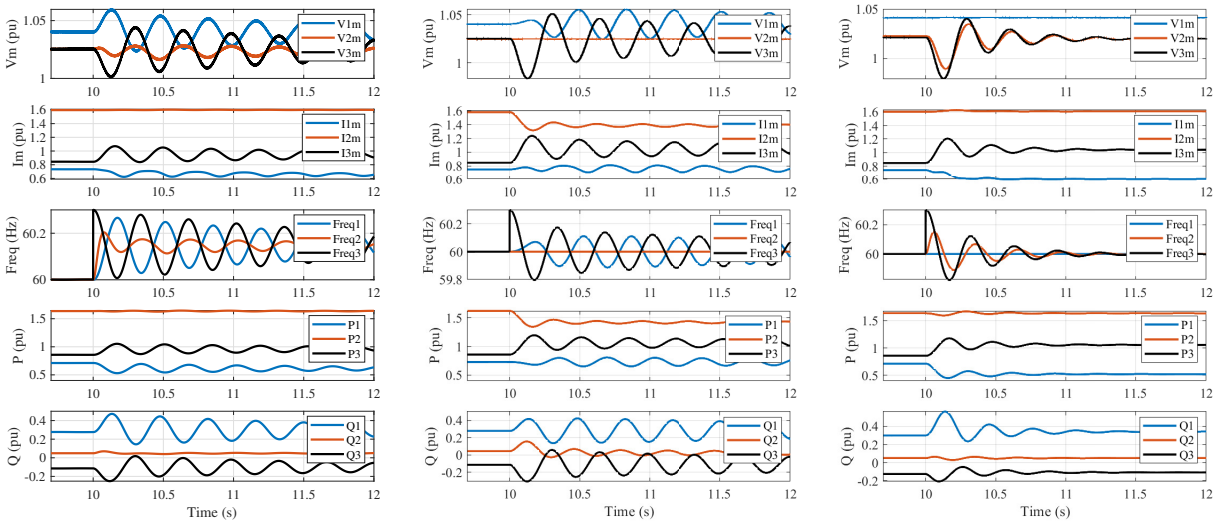

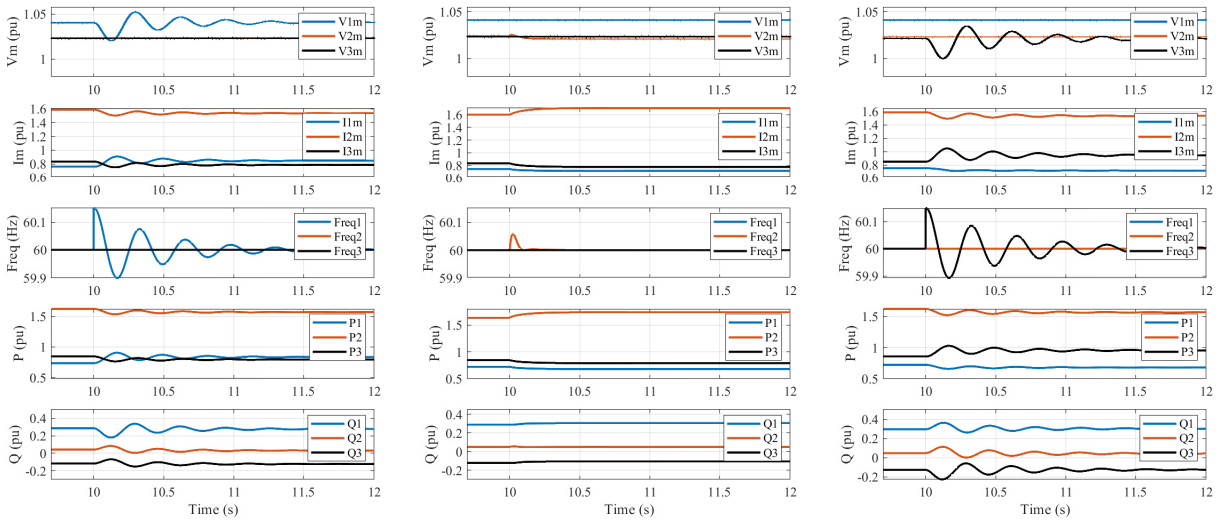

Figure 4.9: PSCAD 9-bus system time-domain dynamic responses

Notation of Fig. 4.9: (a) is case 1 when IBR1, IBR2, and IBR3 are online; (b) is case 6 when IBR1 and IBR3 are online; (c) is case 5 when IBR2 and IBR3 are online; (d) is case 2 when only IBR1 is online; (e) is case 3 when only IBR2 is online; (f) is case 4 when only IBR3 is online.

Fig. 4.9(a) is to validate case 1 results when all three IBRs are online. It presents the bus 1,2,3 dynamic responses, i.e., measured nodal voltage magnitudes, currents, frequencies, real and reactive powers, when bus 3 GFM2 active power generation steps up 0.1 p.u. at $t = 10$ s in PSCAD 9-bus testbed. The marginal damped 3 Hz oscillation matches to the eigenvalue analysis in Fig. 4.5. The voltage magnitude dynamic indicates that bus 1 swing against bus 2, 3, which matches the mode shape in Fig. 4.7 (a). The current magnitude dynamic matches to mode shape in Fig. 4.7 (b), where IBR1 leads IBR3 about 140 degree and IBR2 current has no obvious oscillation. Additionally, IBR3's dynamic is more obvious than IBR2. The frequency dynamics are showing that bus 1 frame is opposite to bus 2,3 frame. That matches to the mode shape in Fig. 4.7 (e). From power dynamics, it can be seen IBR1's real and reactive power swings against IBR3, which can be reflected from Fig. 4.7 (c), (d). Therefore, the PSCAD dynamic performance fully validated the mode shape analysis we carried out in mode shape analysis.

Fig. 4.9(b) is to validate case 6 and (b) is to validate case 5. In Fig. 4.9(b), the interaction between IBR1 and IBR3 exists while IBR2 is substituted by an ideal voltage source. The 3 Hz oscillation mode is observed and matched with the eigenvalue analysis in Fig. 4.8 (b). Furthermore, IBR1 is shown to swing against IBR3.

Fig. 4.9(c) indicates that there is a well damped 3 Hz oscillation instead of a poorly damped oscillations when IBR2 and IBR3 are online. That means that the poorly damped mode is caused by IBR1 and IBR3. Absence of IBR1 leads to disappearance of the poorly damped mode. This observation also matches with the eigenvalue analysis in Fig. 4.8 (b).

Fig. 4.9 (d), (e), (f) are to validate case 2, case 3, case 4 when a single IBR is online. From those three case simulation results, we can verify the eigenvalue analysis in Fig. 4.8 (a). With only IBR1 or IBR3 online, there is a well-damped 3-Hz mode in system. With only IBR2 online, there exists no 3-Hz mode oscillation mode. Moreover, we can still see the power interactions on bus

1,2,3 in (d) and (f). That also indicate the fact that interaction effect between bus 1 and bus 3 is due to IEEE 9-bus system network characteristics.

The set of the studies not only demonstrated the usefulness of the mode shape analysis tool, but also demonstrates that for a 100% IBR-penetrated power grid, a new type of inter-area oscillations may appear. These inter-area oscillations are manifested as an IBR or a group of IBRs swinging against another or another group of IBRs.

4.4 Conclusion

This part investigated a 3-Hz oscillation phenomenon for a power grid with high penetration IBRs via and admittance-based modal analysis framework. This framework is far different from the conventional small-signal analysis tools which rely on transparent models. This work relies on obtaining dq admittance models from OEM supplied black-box models. The current research achieves scalability for admittance-based eigenvalue analysis compared to the state-of-the-art admittance-based stability analysis, where majority of them are limited to two-component systems. The eigenvalue can accurately capture the dominant oscillation mode in the measured frequency range. Furthermore, extended mode shapes are conducted for a variety of measurements and used for influencing factor examination. Utilizing the proposed mode shape analysis tool, we are capable to identify a 3-Hz oscillation mode as the new type of inter-area oscillation mode wit two remote IBRs swinging against each other.

Chapter 5: Fast Dynamic Simulation of IBR Using Measured Admittance Model

Considering the confidentiality constraints of detailed control information of IBRs, they are treated as black-box models and obtain the corresponding admittance/impedance models from measurements for stability analysis. This chapter is to answer a question: Is it possible to produce time-domain simulation results with admittance model which used for stability analysis? In previous mentioned method, a linear state-space model can be created for the entire system by interconnecting components. However, this research is aimed to relax the requirement on knowing each component's model properly. So this work seeks an alternative approach: direct conversion of frequency-domain data to time-domain data via numerical Laplace transform (NLT). First, it presents NLT's advantage over inverse fast Fourier transfer (IFFT) using tutorial electric circuit examples. Then, an example of a type-4 wind farm weak grid operation stability analysis and fast simulation using admittance models obtained from measurements are examined. It can be proven that frequency-domain measurements, along with data fitting and NLT, lead to not only stability analysis bus also fast time-domain simulation for stability demonstration.

The rest of this chapter [3] is organized as follows. The first section introduces the NLT routine briefly. The second section presents two simple electric circuits as examples to illustrate the limitation of IFFT method. The third section presents the process of transforming the frequency-domain data to time-domain data for the test system. Finally, conclusions are drawn in the fourth section.

5.1 NLT Routine

In this section, numerical Laplace transform (NLT) implementation will be introduced briefly. The reader can refer to [63] for the details and coding.

[3] The majority of this chapter has been accepted by IEEE North American Power Symposium [62] and will be presented on November 2021.

The input data of NLT computation is equally-sampled frequency-domain data, while the output is time-domain data.

For a given Laplace transfer function, e.g., $F(s)$, we may set N as the total number of samples in the time domain, and T as the observation time. The sampling intervals for frequency-domain and time-domain discretization are $\Delta\omega$ and Δt, respectively, which can be computed as follows.

$$\Delta t = T/N, \;\; \Delta\omega = \pi/T \tag{5.1}$$

Using the intervals defined above, the discrete version of f(t) and F(s) are given as

$$f_n = f(n\Delta t), \quad \text{for } n = 0, 1, ...N-1 \tag{5.2}$$

$$F_{2k+1} = F(c + j(2k+1)\Delta\omega)), \quad \text{for } k = 0, 1, ...N-1 \tag{5.3}$$

where c is a damping coefficient [64], defined as follows:

$$c = \ln(N^2)/T \tag{5.4}$$

The inverse numerical Laplace transform is defined by (5.5).

$$f_n = \text{Re}\left\{ C_n \left[\sum_{k=0}^{N-1} F_{2k+1}\sigma_{2k+1} e^{j2\pi kn/N} \right] \right\} \tag{5.5}$$

where

$$C_n = 2Ne^{cn\Delta t} e^{j\pi n/N} \Delta\omega/\pi \tag{5.6}$$

The part inside the square bracket in (5.5) can be obtained from IFFT [65]. And the window function coefficient σ in (5.5) may adopt Hanning, Lanczos, and Blackman methods. The major MATLAB coding is attached in the appendix.

5.2 Examine NLT on Simple Circuits

This section presents two simple examples to illustrate IFFT and NLT application to transient analysis.

Figure 5.1: RLC and RL circuit

Fig. 5.1 shows a RLC circuit and a RL circuit in subplot (a) and (b), respectively. Assume $R = 0.3\ \Omega$, $L = 0.5/\omega_0$ H, and $C = 0.4/\omega_0$ F, where $\omega_0 = 377$ rad/s. Therefore, their Laplace admittance in s-domain can be written as follows:

$$Y_{RLC} = \frac{1}{R + Ls + \dfrac{1}{Cs}} \tag{5.7a}$$

$$Y_{RL} = \frac{1}{R + Ls} \tag{5.7b}$$

A step change will be applied to the source voltage. Bode plots of the current transfer function for the two circuits are presented in Fig. 5.2.

With the given Laplace-domain transfer functions and discretized frequency-domain data, the time-domain discrete data can be obtained via IFFT and NLT routine described in Section II. The computed time-domain response is compared with the transient responses obtained via MATLAB `step` function. All those time-domain data are plotted together in Fig. 5.3.

From Fig. 5.3 (a) RLC circuit, it can be observed that both IFFT and NLT methods can predict the exactly same time-domain transient responses as the benchmarked step response. From Fig. 5.3 (b), only NLT can produce the accurate time-domain data in the RL circuit example. IFFT's result does not match the actual time-domain response.

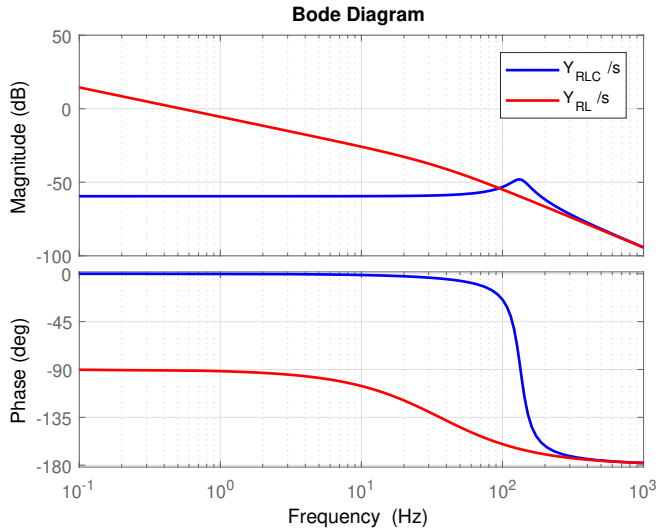

Figure 5.2: Bode plots of RLC and RL circuit current response subject to a step change in the voltage: Y/s

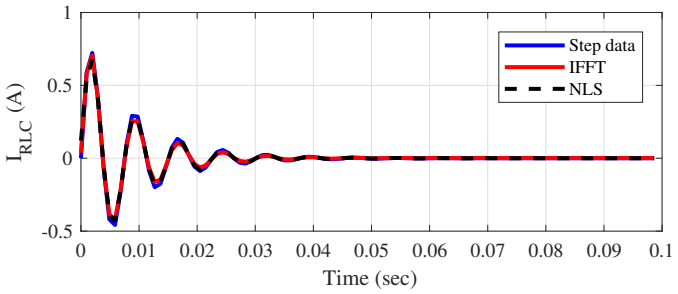

(a)

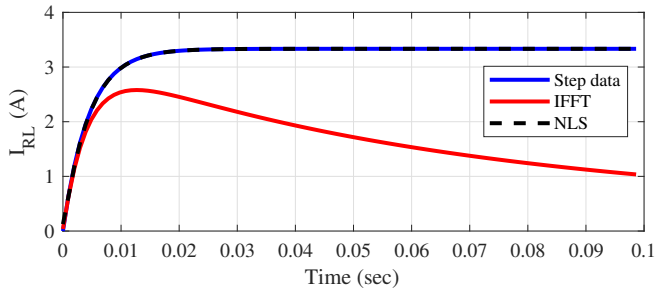

(b)

Figure 5.3: Time-domain current response of RLC circuit and RL circuit

The reason for this discrepancy is that the RL circuit's frequency-domain data have no limit in the low-frequency range. This violates IFFT's assumption. NLT introduces damping into the conversion process; thus, NLT gives accurate time-domain results.

5.3 Test System of A Wind Farm with Weak Grid Interconnection

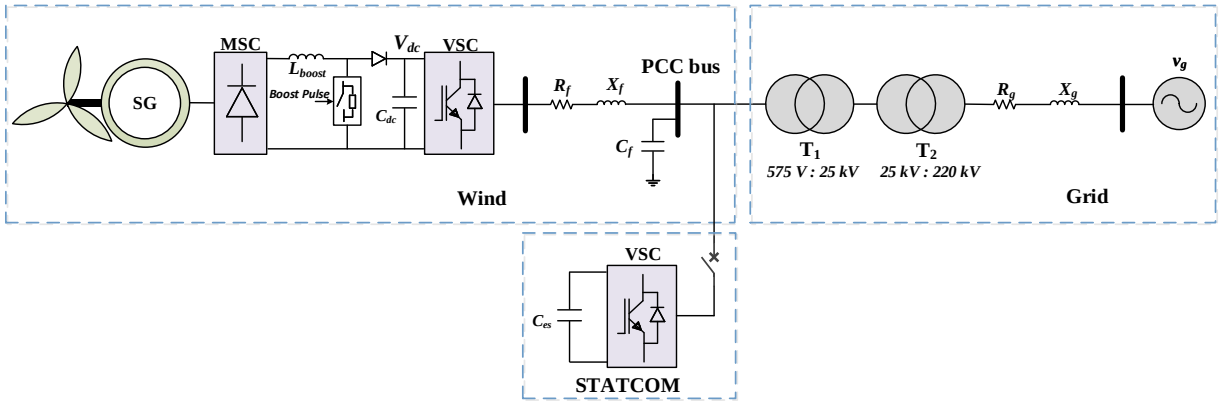

Figure 5.4: EMT test bed of a type-4 wind farm with a STATCOM in MATLAB/SimPowerSystems

A type-4 wind farm with STATCOM is given in Fig. 5.4, which is built in MATLAB/SimPowerSystems platform. Assuming that wind and STATCOM control structures and parameters are unknown. We can treat them as two black-boxes and perform frequency scans to obtain the frequency-domain responses.

5.3.1 Admittance Measurement

Fig. 5.5 shows the measurement test bed. The wind farm (or the STATCOM) are connected to a controllable voltage source. The fundamental components $V_{\mathrm{s,d0}}$ and $V_{\mathrm{s,q0}}$ ensure that the wind side operation condition is constant as in Fig. 5.4. At a frequency f_i, a 0.1 pu voltage harmonic injection ($V_{\mathrm{s,dinj}}$) is superimposed in the d-axis. Conversion between abc-frame and a 60-Hz dq-frame is based on the angle $\omega_0 t$. Next, the phasor at frequency f_i is extracted via Fourier transform from the measured current in the dq-frame. The admittance left column $Y_{\mathrm{wind,dd}}(f_i)$ and $Y_{\mathrm{wind,qd}}(f_i)$ are computed by the ratios of current phasors against voltage phasors in the dq frame. Similarly, another harmonic injection at q-axis voltage ($V_{\mathrm{q,inj}}$) and measured dq currents can identify the right column component $Y_{\mathrm{wind,dq}}(f_i)$ and $Y_{\mathrm{wind,qq}}(f_i)$. Hence, the measured wind side admittance at frequency f_i can be written as (5.8). The measurement range is from 1 Hz to 100 Hz with 1 Hz interval, and measured data are shown as the red markers in Fig. 5.6.

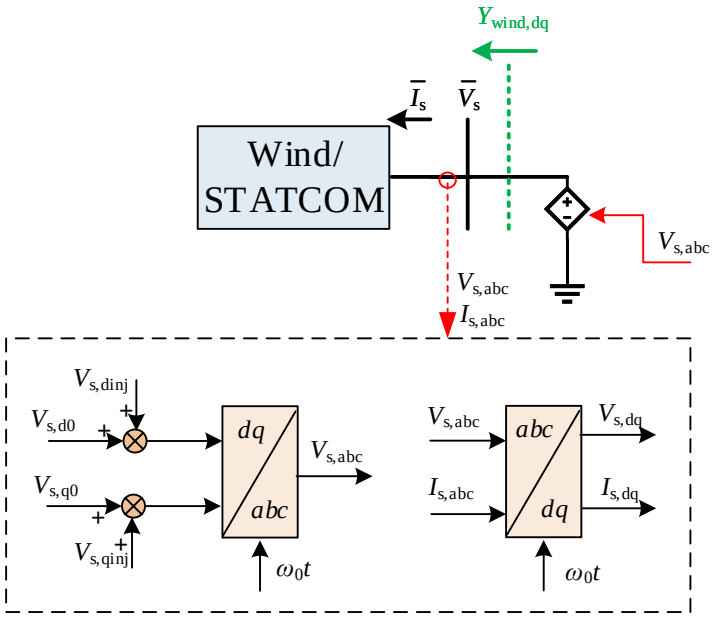

Figure 5.5: Wind/STATCOM admittance measurement using frequency scanning method in dq-frame

$$
\begin{aligned}
Y_{\text{wind}}(f_i) &= \begin{bmatrix} Y_{\text{wind,dd}}(f_i) & Y_{\text{wind,dq}}(f_i) \\ Y_{\text{wind,qd}}(f_i) & Y_{\text{wind,qq}}(f_i) \end{bmatrix} \\
&= \begin{bmatrix} \dfrac{I_{\text{s,d}}(f_i)}{V_{\text{s,d}}(f_i)} & \dfrac{I_{\text{s,d}}(f_i)}{V_{\text{s,q}}(f_i)} \\ \dfrac{I_{\text{s,q}}(f_i)}{V_{\text{s,d}}(f_i)} & \dfrac{I_{\text{s,q}}(f_i)}{V_{\text{s,q}}(f_i)} \end{bmatrix}
\end{aligned} \tag{5.8}
$$

After obtaining the measurement data in the frequency-domain, vector fitting [34] is implemented to find the s-domain transfer function for the wind farm admittance. The blue lines in Fig. 5.6 show the vector fitting results, which match the measured data very well. Note that the order is set to 14 in vector fitting computation. $Y_{\text{wind}}(s)$ and $Y_{\text{STAT}}(s)$ represent the wind and STATCOM admittance s-domain transfer functions.

An RL circuit is used to represent the grid side network. X_g indicates the grid inductance in p.u. and $R_g = 0.1X_g$. Hence, the grid side admittance s-domain transfer function can be expressed as:

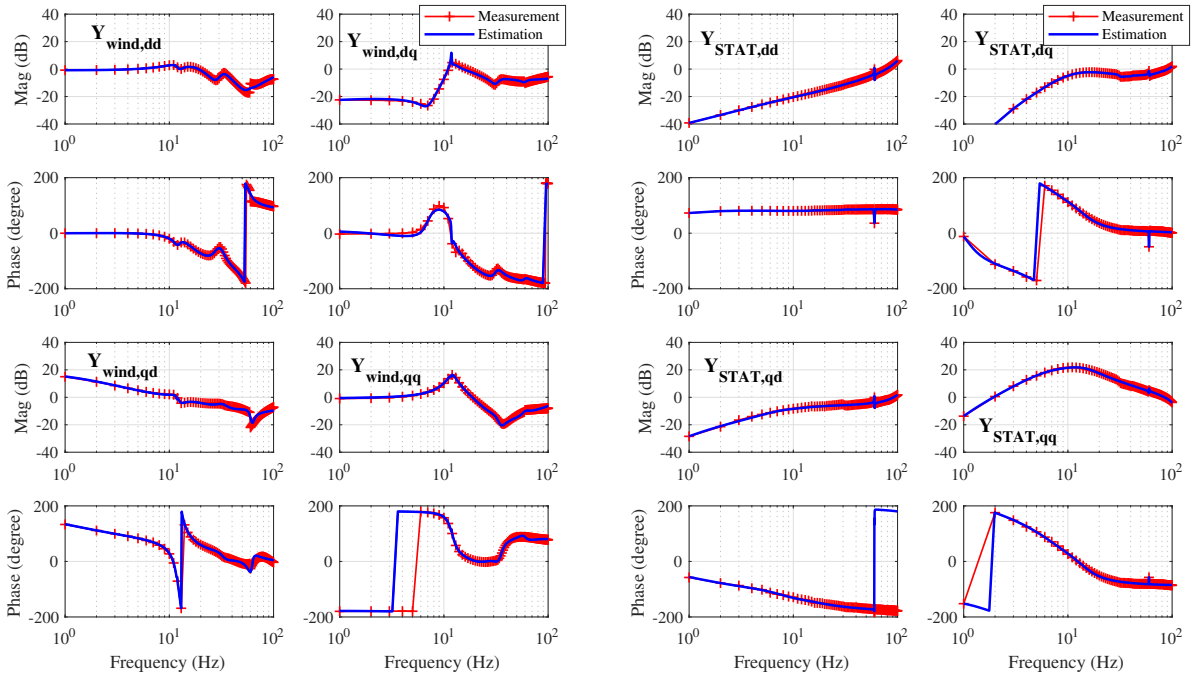

(a) (b)

Figure 5.6: Wind and STATCOM admittance frequency responses in dq-frame

$$Y_{\mathrm{g}}(s) = \begin{bmatrix} Y_{\mathrm{g,dd}}(s) & Y_{\mathrm{g,dq}}(s) \\ Y_{\mathrm{g,qd}}(s) & Y_{\mathrm{g,qq}}(s) \end{bmatrix} = \begin{bmatrix} R_g + Ls & -L\omega_0 \\ L\omega_0 & R_g + Ls \end{bmatrix}^{-1} \tag{5.9}$$

The total admittance of the wind system with and without STATCOM can be derived via the following equations:

$$Y_{\mathrm{tot}}(s) = Y_{\mathrm{wind}}(s) + Y_{\mathrm{g}}(s) \tag{5.10a}$$

$$Y_{\mathrm{tot}}(s) = Y_{\mathrm{wind}}(s) + Y_{\mathrm{STAT}}(s) + Y_{\mathrm{g}}(s) \tag{5.10b}$$

5.3.2 Eigenvalue Analysis

Eigenvalues of the complete system can be obtained using `tzero`$(Y_{\text{tot}}(s))$ in MATLAB. Eigenvalue trajectory with varying grid impedance X_g from 0.3 to 0.5 p.u. is presented in Fig. 5.7. For the system without the STATCOM, it can be seen that there is a 10-Hz mode crossing the imaginary-axis when X_g increases to 0.42 p.u. On the other hand, a 4-Hz mode will move to the right-half-plane (RHP) after adding the STATCOM when X_g is greater than 0.4 p.u. Thus, we can predict that this wind farm system without STATCOM will experience 10-Hz oscillations, and the wind farm system with STATCOM will experience 4-Hz oscillations when the grid becomes weak.

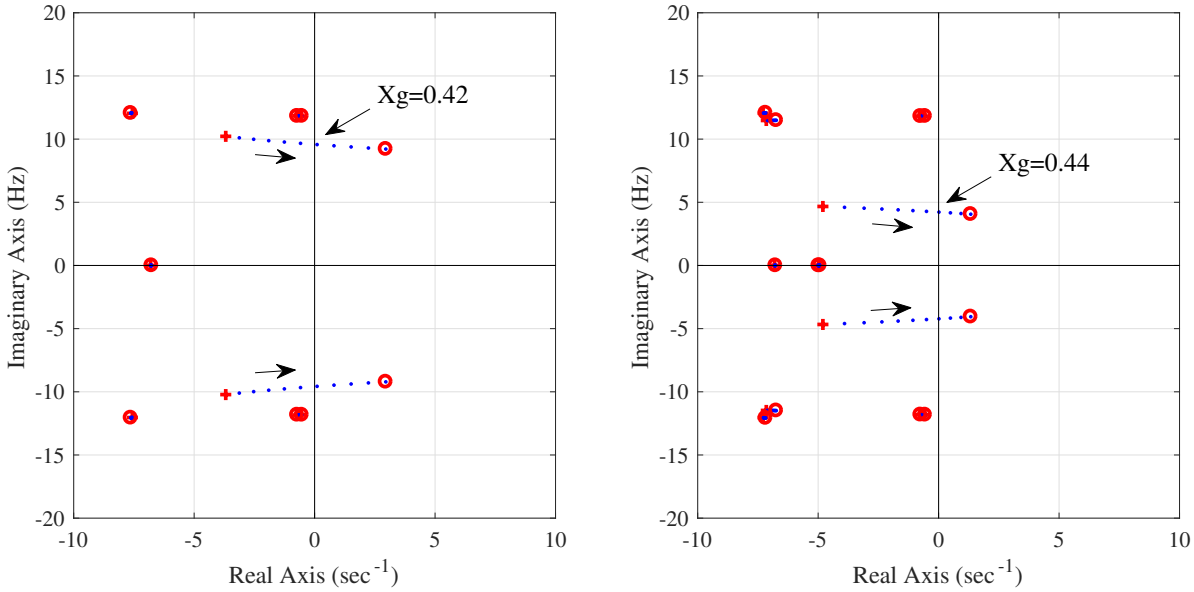

Figure 5.7: Eigenvalue trajectory of without/with STATCOM when varying X_g from 0.3 to 0.5 p.u. with 0.02 step interval

5.3.3 Time-Domain Transient Responses

With the total admittance model, the system impedance can be found by equation (5.11).

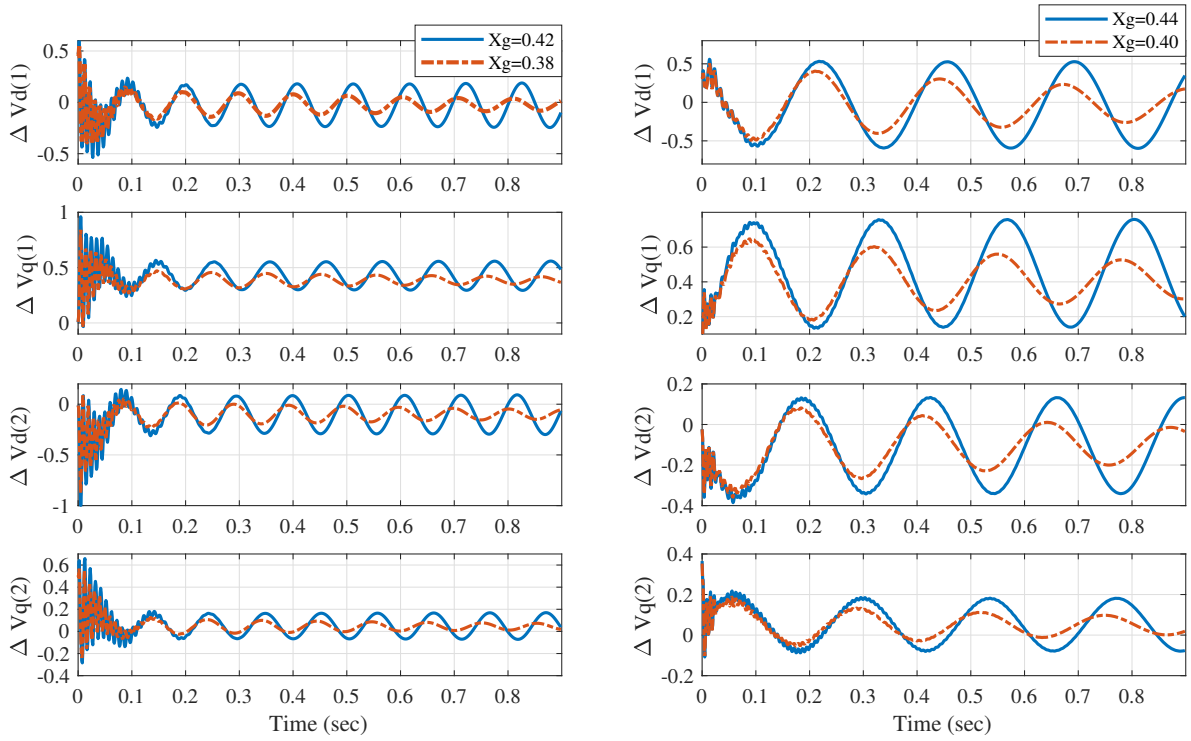

(a) (b)

Figure 5.8: NLT derived voltage time-domain response of without/with STATCOM regarding current step injection on PCC bus

$$Z_{\text{tot}}(s) = Y_{\text{tot}}(s)^{-1} = \begin{bmatrix} Z_{\text{tot,dd}}(s) & Z_{\text{tot,dq}}(s) \\ Z_{\text{tot,qd}}(s) & Z_{\text{tot,qq}}(s) \end{bmatrix} \tag{5.11}$$

The total system impedance reflects the relationship between the PCC voltage and the current injection to the PCC voltage:

$$\begin{bmatrix} \Delta V_{\text{d}} \\ \Delta V_{\text{q}} \end{bmatrix} = \begin{bmatrix} Z_{\text{tot,dd}}(s) & Z_{\text{tot,dq}}(s) \\ Z_{\text{tot,qd}}(s) & Z_{\text{tot,qq}}(s) \end{bmatrix} \begin{bmatrix} \Delta I_{\text{d}} \\ \Delta I_{\text{q}} \end{bmatrix} \tag{5.12}$$

The voltage dynamic responses subject to a step change in the d-axis (or q-axis) current injection can be found by evaluating NLT for each component of $Z_{\text{tot}}(s)$. For example, for a step change

in the d-axis current injection, the dq-axis voltages in s-domain are $Z_{\text{tot,dd}}/s$ and $Z_{\text{tot,qd}}/s$. The corresponding frequency-domain data can be directly converted to the time-domain responses via NLT. In Fig. 5.8, (1) indicates I_{d} step change and (2) indicates I_{q} step change.

Fig. 5.8 (a) presents the scenario without STATCOM. Blue lines represents the case when $X_g = 0.42$ p.u. Red lines correspond to $X_g = 0.38$ p.u. The system has undamped 10-Hz oscillations when X_g is 0.42. If X_g is 0.38, the 10-Hz oscillations have more damping. This matches the eigenvalue analysis results in Fig. 5.7 (a).

Additionally, there are 100-Hz oscillations quickly damped in both cases. That is due to the 100-Hz mode identified by the eigenvalue analysis. Similarly, the scenario with STATCOM is presented in Fig. 5.8 (b). It can be seen the 4-Hz oscillations occur once X_g is 0.44 p.u. The time-domain simulation results corroborate the eigenvalue analysis results in Fig. 5.7 (b).

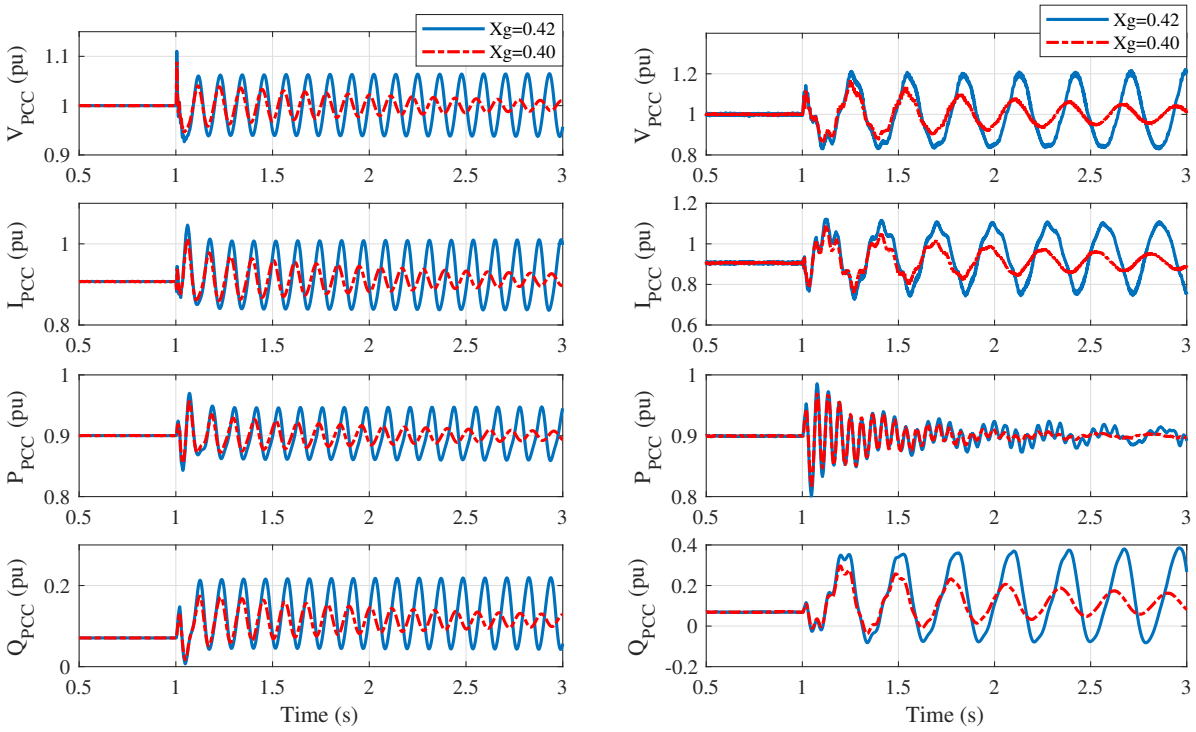

Figure 5.9: EMT time-domain simulation of without/with STATCOM regarding tripping a transmission line. All initial condition is when $X_g = 0.3$ pu

To validate the NLT-based time-domain responses, the simulation results of the test bed from MATLAB/SimPowerSystems are presented in Fig. 5.9. Before $t = 1$ s, the grid-side impedance X_g is kept at 0.3 p.u. X_g has an increased value due to the tripping of a parallel transmission line at $t = 1$ s. Fig. 5.9 (a) presents the dynamic responses for the system without the STATCOM. It shows that the wind system will have 9-Hz undamped oscillations if X_g increases to 0.42 p.u. On the other hand, Fig. 5.9 (b) presents the dynamic responses for the system with the STATCOM. Once X_g is increased above 0.42 p.u, there will be 3.5-Hz undamped oscillations. Those observations agree with the fast time-domain dynamic responses obtained from NLT routine, shown in Fig. 5.8.

5.4 Conclusion

This chapter illustrates how to implement the NLT routine to carry out fast time-domain simulation based on admittance models obtained from measurements. Firstly, it demonstrates the advantage of NLT over IFFT through two simple examples. Secondly, it offers an alternate approach of fast time-domain simulation starting from admittance models. While the prior art, e.g., CCM, relies on converting an admittance model to a linear state-space model and interconnecting various components to a closed-loop system, the proposed approach directly deals with s-domain admittance models and leads to a closed-loop system expressed in s-domain. Time-domain simulation results are obtained through direct conversion of frequency-domain data to time-domain data. This approach is straightforward. The approach has been tested on a grid-interconnected type-4 wind farm to demonstrate weak grid oscillations with and without STATCOM.

Chapter 6: Conclusion and Future Works

The major works in this dissertation will be concluded and future works will be planned in this chapter.

6.1 Conclusion

This dissertation gives a tutorial on how to model, identify, and conduct stability analysis for IBRs integrated power systems.

A reduced-order simplified analytical modeling method is presented with assuming an IBR system is known. This nonlinear analytical model is detailed in chapter 2 for a PV system connected to a weak grid and chapter 3 for general IBR blocks. It is built in MATLAB/Simulink with the capability of not only conducting small-signal analysis but also carrying out dynamic simulations. Eigenvalue analysis can find out the oscillation modes after linearizing at a particular working condition. Furthermore, participation factor analysis can identify the most impact state in the analytical model to explain the root cause of stability issues. In addition, the sensitivity of controller parameters on system stability can be revealed via open-loop analysis.

Chapter 4 and 5 demonstrated the process to estimate the s-domain admittance model from measurement data when IBRs are treated as black-boxes. Chapter 4 illustrated how to conduct small-signal analysis using frequency scan identification and mode shape analysis for dynamic responses explanation. A 3-IBR integrated IEEE 9-bus network is given as an example. While chapter 5 showed a method to carry out fast dynamic simulation of IBRs integrated system using measured admittance model via NLT method. A wind farm with paralleled STATCOM under weak grid condition was examined.

6.2 Future Works

The future works are two-fold.

The first expectation is to expend the nonlinear state-space modeling to investigate more sophisticated power systems. In previous work, the simplified analytical modeling is mainly focused on IBR and RLC circuit dynamic components. However, the real-world power grids are typically hybrid systems, including synchronous generators and induction motors. It is plausible to be inquired that if there will be stability issues caused when an unbalanced induction motor starts in an IBR integrated system. Since the Goerges phenomenon has been mentioned with a positive and negative circuit of induction machine in 1950 [66]. Some simulations and modeling works can replicate this phenomenon. The harmonics are observed and it might result in interactions with the IBR systems at particular frequency ranges.

On the other hand, more IBR identification approaches should be tested. Frequency scanning method is not efficient although it is accurate enough for IBR identification. In author's recent work, it has been found that the online numerical perturbation-based measurement is not suitable for GFM converter identification. As mentioned in [67], the impedance or admittance will change if the dq-frame is not aligned to a constant angle. The numerical perturbation will cause the dq rotating frame frequency dynamics which resulting in a mismatch at low frequency range for GFM identification. Hence, some other efficient measurements have been adopted to identify the three-phase converters in power systems. E.g., Chirp signals are implemented to measure the impedance of voltage source converter [68]. Pseudo-random sequence signals are applied to identify battery impedance in [69] and power system frequency-domain responses in [70]. Those two method will be useful to carry out the GFM converter admittance model especially at low frequency range efficiently.

References

[1] NERC, "Integrating inverter-based resources into low short circuit strength systems," December 2017, accessed: 2020-01-21.

[2] S.-H. Huang, J. Schmall, J. Conto, J. Adams, Y. Zhang, and C. Carter, "Voltage control challenges on weak grids with high penetration of wind generation: Ercot experience," in *Power and Energy Society General Meeting, 2012 IEEE*. IEEE, 2012, pp. 1–7.

[3] First Solar, "Deploying utility-scale pv power plants in weak grids," *2017 IEEE PES General Meeting*, July 2017.

[4] NERC, "900 mw fault induced solar photovoltaic resource interruption disturbance report: Southern california event: October 9, 2017," Tech. Rep., February 2018.

[5] L. Fan and Z. Miao, "An explanation of oscillations due to wind power plants weak grid interconnection," *IEEE Transactions on Sustainable Energy*, vol. 9, no. 1, pp. 488–490, 2018.

[6] L. Fan, "Modeling type-4 wind in weak grids," *IEEE Trans. on Sustainable Energy*, vol. 10, no. 2, pp. 853–864, April 2019.

[7] L. Fan and Z. Miao, "Wind in weak grids: 4 hz or 30 hz oscillations?" *IEEE Transactions on Power Systems*, vol. 33, no. 5, pp. 5803–5804, 2018.

[8] Y. Li, L. Fan, and Z. Miao, "Wind in weak grids: Low-frequency oscillations, subsynchronous oscillations, and torsional interactions," *IEEE Transactions on Power Systems*, vol. 35, no. 1, pp. 109–118, 2019.

[9] R. W. Kenyon, A. Sajadi, A. Hoke, and B.-M. Hodge, "Open-source pscad grid-following and grid-forming inverters and a benchmark for zero-inertia power system simulations," in *2021 Kansas Power & Energy Conference*, 2021, pp. 1–6.

[10] J. Rocabert, A. Luna, F. Blaabjerg, and P. Rodriguez, "Control of power converters in ac microgrids," *IEEE transactions on power electronics*, vol. 27, no. 11, pp. 4734–4749, 2012.

[11] D. Pattabiraman, R. Lasseter, and T. Jahns, "Comparison of grid following and grid forming control for a high inverter penetration power system," in *2018 IEEE Power & Energy Society General Meeting (PESGM)*. IEEE, 2018, pp. 1–5.

[12] X. Fu, J. Sun, M. Huang, Z. Tian, H. Yan, H. H.-C. Iu, P. Hu, and X. Zha, "Large-signal stability of grid-forming and grid-following controls in voltage source converter: A comparative study," *IEEE Transactions on Power Electronics*, 2020.

[13] R. Rosso, X. Wang, M. Liserre, X. Lu, and S. Engelken, "Grid-forming converters: an overview of control approaches and future trends," in *2020 IEEE Energy Conversion Congress and Exposition (ECCE)*. IEEE, 2020, pp. 4292–4299.

[14] L. Fan and Z. Miao, "A modular small-signal analysis framework for inverter penetrated power grids: Measurement, assembling, aggregation, and stability assessment," *arXiv preprint arXiv:2003.03860*, 2020.

[15] M. Zhang, Z. Miao, and L. Fan, "Reduced-order analytical model of grid-connected solar photovoltaic system for low-frequency oscillation analysis," *IEEE Transactions on Sustainable Energy*, 2021.

[16] Y. Xu, M. Zhang, L. Fan, and Z. Miao, "Small-signal stability analysis of type-4 wind in series compensated networks," *IEEE Transactions on Energy Conversion*, 2019.

[17] S. Shah, P. Koralewicz, V. Gevorgian, H. Liu, and J. Fu, "Impedance methods for analyzing stability impacts of inverter-based resources: Stability analysis tools for modern power systems," *IEEE Electrification Magazine*, vol. 9, no. 1, pp. 53–65, 2021.

[18] Y. Li, Y. Gu, Y. Zhu, A. Junyent-Ferré, X. Xiang, and T. C. Green, "Impedance circuit model of grid-forming inverter: Visualizing control algorithms as circuit elements," *IEEE Transactions on Power Electronics*, vol. 36, no. 3, pp. 3377–3395, 2020.

[19] W. Du, Z. Chen, K. P. Schneider, R. H. Lasseter, S. P. Nandanoori, F. K. Tuffner, and S. Kundu, "A comparative study of two widely used grid-forming droop controls on microgrid small-signal stability," *IEEE Journal of Emerging and Selected Topics in Power Electronics*, vol. 8, no. 2, pp. 963–975, 2019.

[20] Y. Gu, N. Bottrell, and T. C. Green, "Reduced-order models for representing converters in power system studies," *IEEE Transactions on Power Electronics*, vol. 33, no. 4, pp. 3644–3654, 2017.

[21] N. Pogaku, M. Prodanovic, and T. C. Green, "Modeling, analysis and testing of autonomous operation of an inverter-based microgrid," *IEEE Transactions on power electronics*, vol. 22, no. 2, pp. 613–625, 2007.

[22] M. Raza, E. Prieto-Araujo, and O. Gomis-Bellmunt, "Small-signal stability analysis of offshore ac network having multiple vsc-hvdc systems," *IEEE Transactions on Power Delivery*, vol. 33, no. 2, pp. 830–839, 2017.

[23] P. Vorobev, P.-H. Huang, M. Al Hosani, J. L. Kirtley, and K. Turitsyn, "High-fidelity model order reduction for microgrids stability assessment," *IEEE Transactions on Power Systems*, vol. 33, no. 1, pp. 874–887, 2017.

[24] B. Wen, D. Boroyevich, R. Burgos, P. Mattavelli, and Z. Shen, "Analysis of dq small-signal impedance of grid-tied inverters," *IEEE Transactions on Power Electronics*, vol. 31, no. 1, pp. 675–687, 2015.

[25] L. Harnefors, M. Bongiorno, and S. Lundberg, "Input-admittance calculation and shaping for controlled voltage-source converters," *IEEE transactions on industrial electronics*, vol. 54, no. 6, pp. 3323–3334, 2007.

[26] H. Gong, X. Wang, and L. Harnefors, "Rethinking current controller design for pll-synchronized vscs in weak grids," *IEEE Transactions on Power Electronics*, 2021.

[27] H. Liu and J. Sun, "Voltage stability and control of offshore wind farms with ac collection and hvdc transmission," *IEEE Journal of Emerging and selected topics in Power Electronics*, vol. 2, no. 4, pp. 1181–1189, 2014.

[28] M. K. Bakhshizadeh, F. Blaabjerg, J. Hjerrild, Ł. Kocewiak, and C. L. Bak, "Improving the impedance-based stability criterion by using the vector fitting method," *IEEE Transactions on Energy Conversion*, vol. 33, no. 4, pp. 1739–1747, 2018.

[29] E. I. Batzelis, G. Anagnostou, and B. C. Pal, "A state-space representation of irradiance-driven dynamics in two-stage photovoltaic systems," *IEEE Journal of Photovoltaics*, vol. 8, no. 4, pp. 1119–1124, 2018.

[30] E. Batzelis, G. Anagnostou, I. R. Cole, T. R. Betts, and B. C. Pal, "A state-space dynamic model for photovoltaic systems with full ancillary services support," *IEEE Transactions on Sustainable Energy*, 2018.

[31] Y. Li, L. Fan, and Z. Miao, "Stability control for wind in weak grids," *IEEE Trans. Sustainable Energy*, vol. 10, no. 4, pp. 2094–2103, Oct 2019.

[32] J. Huang, K. A. Corzine, and M. Belkhayat, "Small-signal impedance measurement of power-electronics-based ac power systems using line-to-line current injection," *IEEE Transactions on Power Electronics*, vol. 24, no. 2, pp. 445–455, 2009.

[33] B. Badrzadeh, M. Sahni, Y. Zhou, D. Muthumuni, and A. Gole, "General methodology for analysis of sub-synchronous interaction in wind power plants," *IEEE Transactions on Power Systems*, vol. 28, no. 2, pp. 1858–1869, 2012.

[34] B. Gustavsen and A. Semlyen, "Rational approximation of frequency domain responses by vector fitting," *IEEE Transactions on power delivery*, vol. 14, no. 3, pp. 1052–1061, 1999.

[35] P. Van Overschee and B. De Moor, "N4sid: Subspace algorithms for the identification of combined deterministic-stochastic systems," *Automatica*, vol. 30, no. 1, pp. 75–93, 1994.

[36] M. Verhaegen, "Identification of the deterministic part of mimo state space models given in innovations form from input-output data," *Automatica*, vol. 30, no. 1, pp. 61–74, 1994.

[37] J.-N. Juang and R. S. Pappa, "An eigensystem realization algorithm for modal parameter identification and model reduction," *Journal of guidance, control, and dynamics*, vol. 8, no. 5, pp. 620–627, 1985.

[38] J. Sanchez-Gasca and J. Chow, "Computation of power system low-order models from time domain simulations using a hankel matrix," *IEEE Transactions on Power Systems*, vol. 12, no. 4, pp. 1461–1467, 1997.

[39] A. Almunif, L. Fan, and Z. Miao, "A tutorial on data-driven eigenvalue identification: Prony analysis, matrix pencil, and eigensystem realization algorithm," *International Transactions on Electrical Energy Systems*, p. e12283, 2019.

[40] A. Rygg and M. Molinas, "Apparent impedance analysis: A small-signal method for stability analysis of power electronic-based systems," *IEEE Journal of Emerging and Selected Topics in Power Electronics*, vol. 5, no. 4, pp. 1474–1486, 2017.

[41] A. Semlyen, "S-domain methodology for assessing the small signal stability of complex systems in nonsinusoidal steady state," *IEEE Transactions on Power Systems*, vol. 14, no. 1, pp. 132–137, 1999.

[42] L. Fan and Z. Miao, "Admittance-based stability analysis: Bode plots, nyquist diagrams or eigenvalue analysis?" *IEEE Transactions on Power Systems*, 2020.

[43] "400-kW Grid-Connected PV Farm (Average Model)," https://www.mathworks.com/help/physmod/sps/examples/400-kw-grid-connected-pv-farm-average-model.html, MATLAB, accessed: 2020-7-20.

[44] M. Sahni, D. Muthumuni, B. Badrzadeh, A. Gole, and A. Kulkarni, "Advanced screening techniques for sub-synchronous interaction in wind farms," in *PES T&D 2012*. IEEE, 2012, pp. 1–9.

[45] B. Badrzadeh, M. Sahni, Y. Zhou, D. Muthumuni, and A. Gole, "General methodology for analysis of sub-synchronous interaction in wind power plants," *IEEE Transactions on Power Systems*, vol. 28, no. 2, pp. 1858–1869, 2013.

[46] G. Francis, R. Burgos, D. Boroyevich, F. Wang, and K. Karimi, "An algorithm and implementation system for measuring impedance in the dq domain," in *2011 IEEE Energy Conversion Congress and Exposition*. IEEE, 2011, pp. 3221–3228.

[47] P. Kundur, "Power system stability," *Power system stability and control*, pp. 7–1, 2007.

[48] L. Fan and Z. Miao, "Time-domain measurement-based *dq*-frame admittance model identification for inverter-based resources," *IEEE Transactions on Power Systems*, vol. 36, no. 3, pp. 2211–2221, 2020.

[49] S. Shah and L. Parsa, "Impedance modeling of three-phase voltage source converters in dq, sequence, and phasor domains," *IEEE Transactions on Energy Conversion*, vol. 32, no. 3, pp. 1139–1150, 2017.

[50] A. Yazdani and R. Iravani, *Voltage-sourced converters in power systems: modeling, control, and applications*. John Wiley & Sons, 2010.

[51] L. Fan, *Control and dynamics in power systems and microgrids*. CRC Press, 2017.

[52] H. Liu, X. Xie, X. Gao, H. Liu, and Y. Li, "Stability analysis of ssr in multiple wind farms connected to series-compensated systems using impedance network model," *IEEE Transactions on Power Systems*, vol. 33, no. 3, pp. 3118–3128, 2018.

[53] R. D. Zimmerman, C. E. Murillo-Sánchez, and D. Gan, "Matpower: A matlab power system simulation package," *Manual, Power Systems Engineering Research Center, Ithaca NY*, vol. 1, 1997.

[54] A. R. Bergen, *Power systems analysis*. Pearson Education India, 2009.

[55] A. Delavari, I. Kamwa, and P. Brunelle, "Simscape power systems benchmarks for education and research in power grid dynamics and control," in *2018 IEEE Canadian Conference on Electrical & Computer Engineering (CCECE)*. IEEE, 2018, pp. 1–5.

[56] O. Tremblay, L.-A. Dessaint, and A.-I. Dekkiche, "A generic battery model for the dynamic simulation of hybrid electric vehicles," in *2007 IEEE Vehicle Power and Propulsion Conference*. Ieee, 2007, pp. 284–289.

[57] M. Zhang, Z. Miao, L. Fan, and S. Shah, "Admittance-based small-signal analysis for a 100% ibr-penetrated power grid via frequency scan," *IEEE Transactions on Powre Delivery*, Under review.

[58] Y. Zhan, X. Xie, H. Liu, H. Liu, and Y. Li, "Frequency-domain modal analysis of the oscillatory stability of power systems with high-penetration renewables," *IEEE Transactions on Sustainable Energy*, vol. 10, no. 3, pp. 1534–1543, 2019.

[59] Y. Zhan, X. Xie, and Y. Wang, "Impedance network model based modal observability and controllability analysis for renewable integrated power systems," *IEEE Transactions on Power Delivery*, 2020.

[60] Y. Zhu, Y. Gu, Y. Li, and T. Green, "Participation analysis in impedance models: The grey-box approach for power system stability," *IEEE Transactions on Power Systems*, 2021.

[61] F. Dorfler and F. Bullo, "Kron reduction of graphs with applications to electrical networks," *IEEE Transactions on Circuits and Systems I: Regular Papers*, vol. 60, no. 1, pp. 150–163, 2012.

[62] M. Zhang, Z. Miao, L. Fan, and P. Gomez, "Measured admittance model for dynamic simulation of inverter-based resources using numerical laplace transform," in *2021 North American Power Symposium (NAPS)*. IEEE, Accepted for presentation.

[63] P. Moreno and A. Ramirez, "Implementation of the numerical laplace transform: A review task force on frequency domain methods for emt studies, working group on modeling and analysis of system transients using digital simulation, general systems subcommittee, ieee power engineering society," *IEEE Transactions on power delivery*, vol. 23, no. 4, pp. 2599–2609, 2008.

[64] L. Wedepohl, "Power system transients: Errors incurred in the numerical inversion of the laplace transform," in *Proc. of the 26th Midwest Symposium on Circuits and Systems*, 1983.

[65] J. G. Proakis, *Digital signal processing: principles algorithms and applications*. Pearson Education India, 2001.

[66] H. L. Garbarino and E. T. Gross, "The goerges phenomenon-induction motors with unbalanced rotor impedances," *Transactions of the American Institute of Electrical Engineers*, vol. 69, no. 2, pp. 1569–1575, 1950.

[67] L. Harnefors, "Modeling of three-phase dynamic systems using complex transfer functions and transfer matrices," *IEEE Transactions on Industrial Electronics*, vol. 54, no. 4, pp. 2239–2248, 2007.

[68] Z. Shen, M. Jaksic, P. Mattavelli, D. Boroyevich, J. Verhulst, and M. Belkhayat, "Three-phase ac system impedance measurement unit (imu) using chirp signal injection," in *2013 Twenty-Eighth Annual IEEE Applied Power Electronics Conference and Exposition (APEC)*. IEEE, 2013, pp. 2666–2673.

[69] J. Sihvo, D.-I. Stroe, T. Messo, and T. Roinila, "Fast approach for battery impedance identification using pseudo-random sequence signals," *IEEE Transactions on Power Electronics*, vol. 35, no. 3, pp. 2548–2557, 2019.

[70] S. Hadavi, D. Rathnayake, S. G. Jayasinghe, A. Mehrizi-Sani, and B. Bahrani, "A robust exciter controller design for synchronous condensers in weak grids," *IEEE Transactions on Power Systems*, 2021.

Appendix A: Reuse Permissions of Published Papers

The permission below is for the reproduction of material in Chapter 2.

CCC RightsLink®

Home | Help | Email Support | Sign in | Create Account

IEEE Requesting permission to reuse content from an IEEE publication

Reduced-Order Analytical Models of Grid-Connected Solar Photovoltaic Systems for Low-Frequency Oscillation Analysis

Author: Miao Zhang
Publication: IEEE Transactions on Sustainable Energy
Publisher: IEEE
Date: July 2021

Thesis / Dissertation Reuse

The IEEE does not require individuals working on a thesis to obtain a formal reuse license, however, you may print out this statement to be used as a permission grant:

Requirements to be followed when using any portion (e.g., figure, graph, table, or textual material) of an IEEE copyrighted paper in a thesis:

1) In the case of textual material (e.g., using short quotes or referring to the work within these papers) users must give full credit to the original source (author, paper, publication) followed by the IEEE copyright line © 2011 IEEE.
2) In the case of illustrations or tabular material, we require that the copyright line © [Year of original publication] IEEE appear prominently with each reprinted figure and/or table.
3) If a substantial portion of the original paper is to be used, and if you are not the senior author, also obtain the senior author's approval.

Requirements to be followed when using an entire IEEE copyrighted paper in a thesis:

1) The following IEEE copyright/ credit notice should be placed prominently in the references: © [year of original publication] IEEE. Reprinted, with permission, from [author names, paper title, IEEE publication title, and month/year of publication]
2) Only the accepted version of an IEEE copyrighted paper can be used when posting the paper or your thesis on-line.
3) In placing the thesis on the author's university website, please display the following message in a prominent place on the website: In reference to IEEE copyrighted material which is used with permission in this thesis, the IEEE does not endorse any of [university/educational entity's name goes here]'s products or services. Internal or personal use of this material is permitted. If interested in reprinting/republishing IEEE copyrighted material for advertising or promotional purposes or for creating new collective works for resale or redistribution, please go to http://www.ieee.org/publications_standards/publications/rights/rights_link.html to learn how to obtain a License from RightsLink.

If applicable, University Microfilms and/or ProQuest Library, or the Archives of Canada may supply single copies of the dissertation.

BACK CLOSE WINDOW

About the Author

Miao Zhang received the B.S. degree in electrical engineering Hebei University of Architecture in 2012 and M.S. degree in electrical engineering from the University of South Florida (Tampa FL) in Dec 2016. He joined the University of South Florida Smart Grid Power Systems Lab in Jan, 2017 for Ph.D. study. His research interests include wind energy grid integration EMT modeling, power systems optimization, system identification, and data analysis.